Title

Neural Signal Processing: Electrode-based Brain Imaging, Focalized Neural Stimulation, and Neural Dynamics Study

Author

Li, Ying

Publication Date

2017

Peer reviewed|Thesis/dissertation

University of California
Los Angeles

Neural Signal Processing: Electrode-based Brain Imaging, Focalized Neural Stimulation, and Neural Dynamics Study

A dissertation submitted in partial satisfaction
of the requirements for the degree
Doctor of Philosophy in Bioengineering

by

Ying Li

2017

Abstract of the Dissertation

Neural Signal Processing: Electrode-based Brain Imaging, Focalized Neural Stimulation, and Neural Dynamics Study

by

Ying Li
Doctor of Philosophy in Bioengineering
University of California, Los Angeles, 2017
Professor Wentai Liu, Chair

Simultaneous neuroimaging and neurostimulation provides a powerful tool for monitoring the functional state of the nervous system as well as treating neural diseases. The neuroimaging is able to obtain real-time information of the targets, and provides a dynamic guidance for the neurostimulation, so that the underlying neural network can be modulated with high precision.

The first part of this thesis aims to develop EEG-based brain imaging algorithms with high reconstruction accuracy and speed. EEG brain imaging is able to produce brain images with excellent temporal resolution (∼ms), and is therefore a good candidate for studying the dynamic brain states. However, the corresponding EEG inverse problem is highly ill-posed, thus requiring regularization techniques to impose additional constraints to obtain a precise result. We have developed two novel EEG-based brain imaging methods (s-SMOOTH and gFOTV) using sparse regularizations based on the compressed sensing principle - these methods demonstrate better performance than the state-of-the-art methods in terms of reconstruction accuracy, localization accuracy, and focalization degree. Furthermore, in order to obtain real-time brain images, a novel parallel computing algorithm has been developed to accelerate the image reconstruction speed.

The second part aims to develop optimization methods for noninvasive electrical stimulation, so as to provide high focal accuracy and desired intensity at the target under specific constraints. Conventional optimization methods either maximize the intensity at the target, resulting in low focal accuracy, or maximize the focal accuracy at the expense of low intensity. We have developed a novel optimization method called Stimulation with Optimal Focality and Intensity (SOFI), which provides both high intensity and focal accuracy within the safety constraints. We apply this method to transcranial current stimulation (tCS) and transcutaneous spinal cord stimulation (tSCS).

The last part further studies the neural dynamics with advanced time-frequency analysis techniques. We employ an accurate time-frequency analysis approach - Hilbert Huang Transform (HHT) - which is able to deal with nonstationary and nonlinear signals such as EEG/ECoG. We have demonstrated that it achieves better results than the widely used method - Fourier Transform (FT) - by comparing them in the applications of seizure detection and cross-frequency coupling.

The dissertation of Ying Li is approved.

Richard Joseph Staba

Ian Cook

Daniel T. Kamei

Wentai Liu, Committee Chair

University of California, Los Angeles

2017

To my parents and my dearest Shuo...

for their endless love and support.

Table of Contents

List of Figures

List of Tables

Acknowledgments

I still remember a conversation five years ago when a friend told me with excitement that there is a retina prosthesis device that can help blind people to see light. Shortly after that, I happened to have a chance to talk to Kuanfu Chen, who introduced his lab to me and told me that this lab is the first to work on the retina prosthesis device. At that moment, I had a strong feeling that this is the lab I belong to. In the past few years, I feel very thankful and proud to be a member of this lab, which is dedicated to enabling blind people to see, enabling paralyzed people to walk, and treating patients with brain disorders.

First, I would like to express my highest respect and deepest gratitude to my advisor, Prof. Wentai Liu, who provided me the valuable opportunity to work in this lab. He is a true scholar who devotes all of his career to this very meaningful and exciting field, and is still very passionate about it after all these years. From him, I learned how to become an independent researcher who knows how to define problems and develop elegant solutions, who always prepares to learn new things and who always holds the research to a high standard.

I also would like to thank my PhD committee members, Prof. Richard Staba, Prof. Ian Cook, and Prof. Daniel Kamei, for their valuable time and insightful advice. I am grateful to my collaborators, Prof. Jing Qin, Prof. Stanley Osher, Prof. Wotao Yin and Tianyu Wu. All of this great work of brain imaging would be impossible without you. I am also thankful to our collaborator Dr. Yue-Loong Hsin for providing us with a large amount of valuable epilepsy and event-related potential data.

I want to thank my lab mates, Kuanfu Chen, Yi-Kai Lo, Chihwei Chang, Stanislav Culaclii, Po-Min Wang, Luyao Chen, Hanyue Zhou, Yushan Wang, Yiwen Meng, and many others. Thanks for your sincere friendship. The happy moments shared with you will always stay in my memory. I would like to especially thank my lab mate Yi-Kai Lo, who provided me selfless encouragement and support in my most difficult time. I also want to thank my collaborators in the lab, Luyao Chen and Yushan Wang, for their help of the realistic models in the focalized stimulation project.

I would like to thank my good friends outside the lab: Huihui Zhou, Beijia Li, Hong Lv,

Fangting Xia, Junzhu Su, Shan Jiang, and many others. Thanks for your constant support and for making my graduate student life more iridescent.

Last but not the least, I would like to express my deepest love to my parents. Thanks for teaching me so much wisdom to confront the beauty and frustration of life. Thanks for being my harbor and telling me to never give up. I also want to thank my husband Shuo Tan. Thanks for being such a wonderful boyfriend and husband. Thanks for your support and companionship during both the good and hard times. Thanks for encouraging me to pursue my dream and helping me to become a better self.

Chapter 3 is a version of [LLQ15] and [LQH16], Chapter 4 is a version of [LLQ15], [LQO16] and [QWL16], Chapter 5 is a version of [LL16], and Chapter 6 is a version of [LHL14] and [ZLH16]. Our research was supported in part by grants from California Capital Equity LLC and UC Laboratory Research Fee Program.

Vita

2007-2011	B.S. Theoretical and Applied Mechanics, Peking University, China
2015 Fall	Machine Learning Scientist Intern, Amazon Co. LLC, Seattle, WA
2016	M.S. Bioengineering, UCLA, Los Angeles, CA

Publications and Presentations

Jing Qin, Tianyu Wu, **Ying Li**, Wotao Yin, Stanley Osher, and Wentai Liu. "Accelerated High-resolution EEG Source Imaging." submitted to 8th International IEEE EMBS Conference on Neural Engineering. IEEE, 2017.

Ying Li, and Wentai Liu. "Focalized Noninvasive Stimulation with Optimization Technique", Provisional Patent Filed, UCLA Case No. UC-2017-497-1-LA.

Ying Li, Jing Qin, Yue-Loong Hsin, Stanley Osher, and Wentai Liu. "s-SMOOTH: Sparsity and Smoothness Enhanced EEG Brain Tomography." in Frontiers in Neuroscience, section Brain Imaging Methods, 2016.

Ying Li, Jing Qin, Yue-Loong Hsin, Stanley Osher, and Wentai Liu. "Sparsity and Smoothness Enhanced EEG Brain Imaging." 2016 BMES Annual Meeting, Oct 5th-8th, Minneapolis, MN.

Ying Li, Jing Qin, Stanley Osher, and Wentai Liu. "Graph Fractional-Order Total Variation EEG Source Reconstruction." 2016 38th Annual International Conference of the IEEE

Engineering in Medicine and Biology Society. IEEE, 2016.

Hanyue Zhou, **Ying Li**, Yue-Loong Hsin, Wentai Liu. "Phase-Amplitude Coupling Analysis for Seizure Evolvement Using Hilbert Huang Transform." 2016 38th Annual International Conference of the IEEE Engineering in Medicine and Biology Society. IEEE, 2016.

Ying Li, Wentai Liu, Jing Qin, Chih-Wei Chang, and Yi-Kai Lo. "Ultra-Dense Electrode-Based Brain Imaging System With High Spatial And Temporal Resolution", Patent Filed, Serial No. PCT/US2016/050452, UCLA Case No. UC-2016-151-2-LA-FP.

Ying Li, Yue-Loong Hsin, and Wentai Liu. "Comparison study of seizure detection using stationary and nonstationary methods." 2014 36th Annual International Conference of the IEEE Engineering in Medicine and Biology Society. IEEE, 2014.

CHAPTER 1

Introduction

Functional neural imaging is able to evaluate brain function, e.g., memory and cognition, as well as help diagnose brain disorders, e.g., epilepsy, depression, schizophrenia and Alzheimer′s disease. However, it is unable to treat the neural disorders by itself. The neural stimulation has been developed to treat neural diseases by intervening with the nervous system, especially for drug-resistant patients, but the location information of the targets is usually unknown in most applications. Recently, it has been realized that the combination of these two techniques can provide more effective stimulation [CCM12]. The neural imaging can provide target information to guide the neural stimulation. In addition, during the stimulation, the neural imaging can also monitor the change of functional states, and provide this feedback to the stimulation algorithm so as to adjust the parameters dynamically. Therefore, concurrent neural imaging and stimulation provides a powerful tool for monitoring the functional state of the nervous system, as well as treating neural diseases. This thesis aims to develop advanced optimization methods to provide brain images with high temporal and spatial resolution, as well as focalized neural stimulation with high precision.

For neural imaging, there have been various functional imaging modalities such as fMRI, PET, SPECT, and EEG-based imaging. Compared to the hemodynamic-based imaging techniques, the EEG-based brain imaging is especially interesting for guiding a dynamic stimulation, since it provides excellent temporal resolution ($\sim$ms). In addition, the device is lightweight and portable, and therefore is more suitable for applications that requires a natural habitual environment. However, the corresponding EEG inverse problem is an ill-posed one that has infinitely many solutions. This is due to the limited number of EEG sensors as well as noise contamination in the recorded signals. To obtain a unique solution,

regularizations can be incorporated to impose additional constraints on the solution. An appropriate choice of regularization is critically important for the reconstruction accuracy of the brain image. The first contribution of this dissertation develops various novel EEG brain imaging algorithms with advanced sparse regularizations, which provide brain images with high reconstruction accuracy and fast speed. For neural stimulation, we focus on noninvasive electrical stimulation techniques, which do not require surgery for implanting the electrodes. The traditional noninvasive stimulation techniques employ two large electrodes, in which the current flow is non-focal and thus a large area is activated. Recently, multi-electrode arrays have been adopted for noninvasive stimulation to obtain multi-site stimulation, which have been demonstrated to be more effective. With multiple electrodes, the stimulation parameters at each electrode can also be optimized to achieve more focal and precise stimulation. The second contribution of this dissertation develops optimization algorithms to provide noninvasive stimulation of the nervous system with high intensity and focal accuracy. Furthermore, it is important to understand the dynamics of the underlying neural networks not only from time domain but also in frequency domain. The third contribution of this dissertation focuses on employing advanced time-frequency analysis methods to study the dynamics of the nervous system with high accuracy.

Chapter 2 introduces the background of EEG-based brain imaging. The mathematical formulation of the EEG inverse problem is introduced, and two groups of EEG inverse methods as well as various regularization techniques are presented. The inverse methods with the widely used ℓ_2-norm regularization [HHI93, Pas02] have the limitation that the reconstructed sources are spread out, resulting in a brain image with low spatial resolution. To obtain a more focal source, methods with sparse regularizations, including ℓ_0-norm and ℓ_1-norm regularizations [UHS99, DH08], were proposed to impose sparsity on the source, which are demonstrated to greatly improve the focalization degree of the source. However, the reconstructed source by these methods is over-focused, therefore these methods fail to estimate the extent of the sources. To address this issue, efforts have been devoted to exploring sparsity in transform domains of the current density, such as the spatial Laplacian domain [HNZ08, VMS08, CNH10], wavelet-basis domain [CNH10, LZD12, ZZD14], Gaussian-basis

domain [HTD11], or variation domain [ACK05, Din09, Gra09, LBM11, BAC14, SLW16]. Total variation (TV) regularization based brain imaging method was proposed recently, which imposes sparsity on the spatial gradient rather than the current density itself. It solves the over-focused problem of ℓ_0-norm or ℓ_1-norm based methods and is able to estimate the extent of the sources. Unfortunately, due to its piecewise constant assumption, the intensity of the reconstructed source is almost uniform.

Chapter 3 presents a novel Sparsity and SMOOthness enhanced brain TomograpHy (s-SMOOTH) method to improve reconstruction accuracy of brain images, by employing advanced variational regularization techniques. More specifically, a voxel-based total generalized variation (vTGV) regularization is employed to promote sparsity on the high-order spatial derivative, and the ℓ_{1-2} regularization is utilized to impose sparsity on the current density itself. The total generalized variation (TGV) regularization [BKP10] has been shown to outperform the Laplacian-based, wavelet-based, and TV-based regularizations in compressive sensing MRI reconstruction [KBP11, QG13, GQY14], image deconvolution and denoising [BKP10, QYW14]. Comparing to its basis, the TV, the TGV incorporates information of higher-order derivatives, and therefore is better suited for modeling piecewise smooth functions [BBB13, BH14]. Notice that the traditional TGV is defined on a 2D image and its extension to an irregular surface is challenging. In order to deal with the 3D cortex surface, we define a voxel-based TGV (vTGV) regularization which extends the definition of the second order TGV from 2D image to an irregular triangular mesh such as the cortical surface. vTGV enhances the smoothness of the brain image and reconstructs the spatial distribution of the current density more precisely. Meanwhile, motivated by the performance of the ℓ_{1-2} regularization in compressive sensing reconstruction and other image processing problems [ELX13, LYH15, YLH15], we incorporate the ℓ_{1-2} regularization into the objective function. Numerical experiments show that ℓ_{1-2} regularization provides faster convergence and yields sparser source images than the ℓ_1-norm regularization. Furthermore, by applying the difference of convex function algorithm (DCA) and alternating direction method of multipliers (ADMM), we derive an efficient numerical algorithm to solve the corresponding optimization problem. A variety of simulation tests on Gaussian-shaped sources with var-

ious noise levels, source sizes, source configurations and locations show that the proposed approach results in better performance than the state-of-the-art methods in terms of total reconstruction accuracy, localization accuracy, and focalization degree. The tests on auditory and visual P300 data further demonstrate that the proposed method is able to preserve high order smoothness and produce brain images with higher spatial resolution.

Chapter 4 focuses on developing accelerated EEG brain imaging method without sacrificing the reconstruction accuracy. For the s-SMOOTH method presented in Chapter 3, although it provides high-quality brain images, its computation is relatively large due to the two complicated regularization terms, which limits its application in real-time brain state monitoring. To address this issue, we propose another novel EEG source reconstruction method based on the Fractional-Order Total Variation (FOTV) to reconstruct brain images with similar accuracy but relatively low computational cost. FOTV has been recently proposed to solve image processing problems [RHZ13, CSZ13]. Different from TV which imposes sparsity of first-order spatial derivatives, FOTV can choose a more flexible and elegant smoothness order for the underlying source by imposing sparsity of α-order derivatives ($\alpha > 0$). Therefore, the proposed method is capable of reconstructing the brain image with higher-order smoothness and preserving natural intensity changes of the brain image. As a consequence, the localization accuracy of peaks is greatly improved compared to TV-based methods. In order to extend the traditional FOTV defined on a 2D rectangular grid to an irregular cortex surface, we treat the cortex surface as a graph and define a novel graph FOTV (gFOTV) using the shortest paths on the graph. In fact, TV-based methods can be considered as a special case in our proposed framework when $\alpha = 1$. In addition, we derive an efficient algorithm using the alternating direction method of multipliers (ADMM). Finally, a large variety of simulations are conducted with different source sizes using a realistic head model. The proposed method is compared with several state-of-the-art ones both qualitatively and quantitatively, which demonstrates superior performance in terms of total reconstruction accuracy, spatial resolution, and localization accuracy. Moreover, in order to further accelerate the brain imaging process, we develop a parallel algorithm by applying the Chambolle-Pock and ARock algorithms along with diagonal preconditioning. A variety

of experiments show that the proposed algorithms have more rapid convergence than the state-of-the-art methods and have the potential to achieve real-time temporal resolution.

Chapter 5 develops optimization algorithms for multi-electrode noninvasive neural stimulation, including transcranial current stimulation (tCS) and transcutaneous spinal cord stimulation (tSCS). For tCS, the current optimization algorithms either maximize the target intensity at the expense of low focal accuracy, or optimize the focality resulting in relatively low target intensity. We propose a novel Stimulation with Optimal Focality and Intensity (SOFI) method, which is able to optimize both the intensity and focality of the target at the same time. A large amount of simulation results demonstrate that the SOFI method is able to achieve focalized stimulation, and it also provides better results than state-of-the-art methods in terms of target intensity, focality, and localization accuracy. For tSCS, the current methods either use two-electrode montage or multi-electrode array with empirical stimulation parameters, which result in non-focal current flow at the target. We construct a realistic spinal cord model based on structural MRI and apply SOFI to design optimal stimulation parameters for each electrode. We demonstrate that it is able to stimulate multiple targets as well as avoid certain regions with high focal and localization accuracy. To the best of our knowledge, this is the first method that designs optimal stimulation parameters for tSCS to achieve focalized stimulation with an array of stimulation electrodes.

Chapter 6 focuses on studying the brain dynamics with advanced time-frequency analysis technique. Fast Fourier Transform (FFT) is widely used for frequency analysis, which assumes that the signal is stationary and linear. However, most bio-signals, such as EEG and ECoG, are nonstationary and nonlinear; therefore, FFT may introduce some inaccuracy to the results. In this dissertation, we propose to use the Hilbert-Huang Transform (HHT), an advanced time-frequency analysis technique that is able to deal with non-stationary and nonlinear signals. We demonstrate that the HHT outperforms FFT in the application of seizure detection and cross-frequency coupling (CFC). For seizure detection, HHT method provides a higher detection accuracy than FFT method with the same set of features. In the application of CFC, HHT provides more regular and stronger coupling patterns than FFT.

Chapter 7 summarizes the dissertation and points out some future directions.

CHAPTER 2

Electrode-based Brain Imaging

In this chapter, we review the background of EEG brain imaging. EEG brain imaging enables us to reconstruct the current density in the brain from the electrical measurements with excellent temporal resolution ($\sim ms$). To reconstruct brain images from the EEG signal, we need to solve the so-called EEG inverse problem.

First, we introduce the mathematical formulation of the EEG inverse problem, the procedures of constructing a realistic head model, and two large groups of inverse methods. A big challenge of solving the EEG inverse problem is that the problem is highly ill-posed, due to the relatively small number of electrodes compared to that of the potential dipole locations. To obtain a unique and precise solution, regularizations can be incorporated to impose additional constraints on the solution. We introduce the widely used ℓ_2-norm based regularization that uses ℓ_2 norm as the regularization term. However, the methods based on ℓ_2-norm regularization tend to generate a brain image with very low spatial resolution. We then present several sparse regularizations, such as ℓ_0-norm or ℓ_1-norm regularization, which overcome this limitation by imposing sparsity constraint on the source. The inverse methods with sparse regularizations are able to improve the spatial resolution of the reconstructed brain image; however, the sources reconstructed by these methods are over-focused. Finally, we explain why imposing sparsity on a transform domain rather than the original domain can help to improve the image reconstruction accuracy. Specifically, some relevant regularizations are introduced and their advantages and disadvantages are discussed.

2.1 Introduction: EEG Inverse Problem

There have been various neural imaging modalities developed so far, such as functional Magnetic Resonance Imaging (fMRI), Positron Emission Tomography (PET), Single-Photon Emission Computed Tomography (SPECT), Electroencephalography (EEG) based imaging, Magnetoencephalography (MEG) based imaging, etc. Hemodynamic imaging techniques, such as fMRI, PET and SPECT, have been widely used since they offer high spatial resolution [PS04]. However, their temporal resolution is limited on the order of seconds due to the relatively slow blood flow response [PS04]. Furthermore, these imaging systems require the subject to be restricted in a large chamber, which limits their applications in the natural habitual environment. On the other hand, brain imaging based on EEG provides an alternative solution that overcomes these limitations. Unlike fMRI, PET and SPECT, EEG has much higher temporal resolution in the range of milliseconds. In addition, it is lightweight and portable, and hence can be used in various applications that require natural environments, such as learning in a classroom. Therefore, in this dissertation, we focus on EEG-based brain imaging.

As a noninvasive method, electroencephalography (EEG) is used to measure brain activity and detect abnormalities associated with certain brain diseases. When neurons in the brain are activated, local currents are generated, and can travel through different tissues, e.g., gray matter, cerebrospinal fluid (CSF), skull and scalp. These currents result in electrical potentials on the scalp that are recorded by electrodes as the EEG signals. The EEG forward problem refers to estimating the electrical potential on the scalp given the current distribution in the brain, while the inverse problem refers to the process of reconstructing the spatial distributions of currents in the form of a 3D brain image given the electrical recordings.

2.1.1 Mathematical Formulation

To formulate this problem in mathematical expressions, we assume that dipole sources are located on the cortex surface [DS93]. In addition, we assume that the orientation of each

dipole is perpendicular to the cortex surface [DS93]. This is based on the assumption that most of the current flow to the scalp is produced by cortical pyramidal cells, which are normal to the cortical surface [DS93, NS06]. Let $b \in \mathbb{R}^N$ be the electrical potential on the scalp measured by the electrodes, where N is the number of electrodes, and $u \in \mathbb{R}^M$ is the neural current density at each dipole location. The electrode potential b can be related to the neural current u by the following linear equation

$$b = Au + n, \tag{2.1}$$

where $n \in \mathbb{R}^N$ denotes the noise and $A \in \mathbb{R}^{N \times M}$ is called *lead field matrix*. Note that the (i, j)-th entry of A stands for the electrical potential measured by the ith electrode due to a unit dipole source at the jth location. The matrix A can be calculated by constructing a head model [OV91, Gul98, FKW02], and solving the Maxwell′s equations [Sar87] with the boundary element method (BEM) [OV91, FKW02].

2.1.2 Realistic Head Model Construction

In order to obtain a brain image with high accuracy, a realistic head model based on individual MR image is desired. The basic steps for constructing a head model with boundary element method (BEM) include: 1) segmentation, in which the head is segmented into different tissue layers, e.g. scalp, skull, brain; 2) meshing, in which a triangular mesh is constructed for each layer to describe the geometry; 3) lead field matrix calculation, in which a one-to-one mapping is calculated between each electrode and each dipole by BEM, and the result is stored in the lead field matrix A.

Currently, there are various open-source toolboxes available for head model construction, including Freesurfer (`https://surfer.nmr.mgh.harvard.edu/`), SPM (`http://www.fil.ion.ucl.ac.uk/spm/`), Fieldtrip (`http://www.fieldtriptoolbox.org/`), NFT (`https://sccn.ucsd.edu/wiki/NFT`), etc. Fig. 2.1 illustrates a realistic head model we constructed based on high-resolution MRI with Fieldtrip toolbox [OV91, FKW02], which contains the scalp, skull, brain, and the cortex surface.

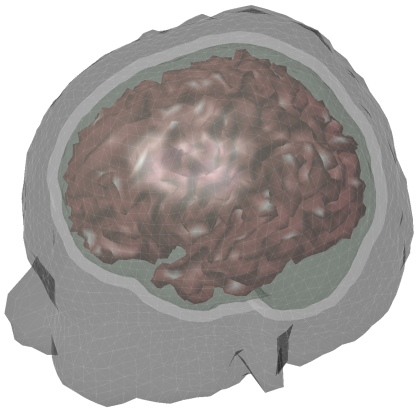

Figure 2.1: Construction of a realistic head model from MRI. From outside in are: scalp (gray), skull (white), brain (green), cortex surface (brown).

2.1.3 Two Groups of Inverse Methods: Dipolar and Distributed Models

In general, there are two types of models for solving the EEG inverse problem: dipolar and distributed source model [MML04]. The dipolar model [SGA78, SV86, MLL92] assumes that a small number of focal sources are active so only a few parameters of these sources need to be estimated. Since the number of unknown parameters is usually smaller than that of the measurements, the corresponding inverse problem is over-determined and can be solved by nonlinear optimization techniques [UHS98]. However, the source reconstruction is usually highly sensitive to the initial values due to the high non-convexity of the objective function. Furthermore, this model is not able to handle spatially extended sources, such as that during the propagation of a seizure. On the other hand, in the distributed source model [HI84, HHI93], the source space is divided into a lot of voxels with fixed locations, and only the activation in each location needs to be estimated. However, due to a relatively small number of electrodes ($\sim 10^2$) and a large number of potential dipole locations ($\sim 10^4$), the corresponding inverse problem is highly under-determined and results in infinitely many solutions. To obtain a unique solution, regularization can be used to impose additional constraints on the solution.

2.2 Inverse Methods for Distributed Model

In this dissertation, we focus on the distributed source model. In this model, we assume that the source space is divided into M voxels with fixed locations. Usually, the number of voxels M is much larger than the number of electrodes N, thus the linear system Eq. (2.1) is highly under-determined and has infinitely many solutions. To guarantee uniqueness of the solution for the distributed source model, regularization techniques can be applied to impose additional constraints on the solution. We consider the following model to reconstruct the brain image

$$\min_u \frac{1}{2} \|Au - b\|_2^2 + \alpha \mathcal{R}(u), \tag{2.2}$$

Here, the first term, called data fidelity term, reflects the statistics of the Gaussian noise. The second term is the regularization term which is related to the assumption on the characteristics of u, e.g., smoothness or sparsity. The regularization parameter α controls the trade-off between these two terms.

2.2.1 L_2-norm Based Regularization

The L_2-norm based regularization is the earliest used regularization for EEG-based brain imaging. It uses the ℓ_2-norm of the current density as the regularization term, i.e. $\mathcal{R}(u) = \|Wu\|_2$ where W is a weighting matrix; therefore, it chooses a solution with minimal energy. The corresponding model for solving the inverse problem can be expressed as follows

$$\min_u \frac{1}{2} \|Au - b\|_2^2 + \alpha \|Wu\|_2 , \tag{2.3}$$

The minimum ℓ_2-norm methods include several widely-used methods, such as minimum norm estimate (MNE) [HHI93], weighted minimum norm estimate (wMNE) [JLS87, DS93], low resolution brain electromagnetic tomography (LORETA) [Pas99], and standardized low resolution brain electromagnetic tomography (sLORETA) [Pas02]. These methods usually have a closed-form solution and thus the computational cost is relatively low. This advantage

makes L_2-norm based methods convenient and easy to implement. However, they share a limitation that the reconstructed sources spread over a large area of the brain, resulting in a brain image with low spatial resolution, i.e., proximal sources may become indistinguishable in the solution.

2.2.2 Sparse Regularization: L_0 and L_1 Regularizations

To overcome the limitation of minimum ℓ_2-norm methods, sparse structure of the underlying source has been explored to improve the focalization of the source. A natural strategy to impose sparsity is ℓ_0-norm regularization which minimizes the number of nonzero intensity values in the image. However, since the ℓ_0-regularized problem is computational NP-hard, its ℓ_1-norm relaxed version is usually considered in practice. For a real nonnegative number p, the ℓ_p-norm of $u \in \mathbb{R}^{\mathbb{M}}$ is defined as

$$\|u\|_p = (\sum_{i=1}^{M} |u_i|^p)^{\frac{1}{p}}, \quad p \geq 0. \tag{2.4}$$

Here p can be any non-negative value (e.g. $p = 0$ corresponds to ℓ_0-norm, and $p = 1$ corresponds to ℓ_1-norm).

Different from minimum ℓ_2-norm methods, the minimum ℓ_0-norm or ℓ_1-norm methods, such as focal underdetermined system solution (FOCUSS)[GGR95], minimum current estimate (MCE) [UHS99], and sparse source imaging (SSI) [DH08], assume that the source current density is sparse with only a few active voxels. As a result, these methods greatly improve the focalization degree of the reconstructed source and are better at distinguishing proximal sources.

2.2.3 Sparsity on Transform Domain

For methods that impose sparsity on the original source domain, although the focalization is greatly improved, these methods fail to estimate the extent of the sources since the reconstructed source is over-focused. To address this issue, efforts have been devoted to exploring sparsity on transform domains of the current density, such as the spatial Laplacian domain

[HNZ08, VMS08, CNH10], wavelet-basis domain [CNH10, LZD12, ZZD14], Gaussian-basis domain [HTD11], or variation domain [ACK05, Din09, Gra09, LBM11, BAC14, SLW16]. Mathematically, the corresponding model can be expressed as

$$\min_u \frac{1}{2} \|Au - b\|_2^2 + \alpha \|Du\|_1 , \tag{2.5}$$

where D is an operator for the transformation. For example, if D is the finite difference operator, then the model imposes sparsity on the variational domain [ACK05, Din09, Gra09].

Furthermore, in order to obtain a local smooth and global sparse result, some approaches impose sparsity on both the transform domain and the original source domain. For example, Focal Vector field Reconstruction (FVR) [HNZ08] and ComprEssive Neuromagnetic Tomography (CENT^L) [CNH10] impose sparsity on the spatial Laplacian and the current density itself. It has been shown that combination of these two regularization terms improves the imaging results than by using ℓ_2-norm or ℓ_1-norm regularization alone. However, the Laplacian operator, i.e., the sum of all unmixed second partial derivatives, tends to assign high weight to the central voxel and relatively low weights to its neighbors, which results in the over-smoothing effect of the reconstructed image. Sparse Total Variation (TV) methods, also known as TV-ℓ_1 [BAC14, SLW16], impose the sparsity constraint on both the spatial gradient and the current density itself. They assume that the current density distribution is piecewise constant, and are able to preserve the extent of the sources well. However, due to the piecewise constant assumption, the reconstructed current density distribution is almost uniform in each subregion (so called "staircasing effect"), which fails to reflect the intensity variation of the source in space. As a consequence, these methods have difficulty localizing peaks of the source, leading to relatively large localization error.

2.3 Quantitative Evaluation of the Inverse Methods

In order to quantitatively evaluate the performance of an EEG source imaging method, we use the following criteria to evaluate the results for synthetic data:

(a) *Total reconstruction error* (TRE), which measures the relative difference between the

true source and the reconstructed one [IAJ03]. The smaller the TRE, the higher reconstruction accuracy the brain image will have. TRE is defined as

$$TRE = \frac{\|\hat{u} - u\|_2}{\|u\|_2},$$

where u is the true source and $\hat{u}$ is the reconstructed source. Note that TRE has no units since it is a relative value.

(b) *Localization error* (LE), which measures the distance between the peaks of the true source and the reconstructed one [IAJ03, MSB08]. Suppose that there are K underlying sources and LE_k is the localization error of the k-th source; then LE is defined as the average localization error of all the sources. In order to define LE_k, let I_k be a set of voxel indices that are spatially closest to the peak of the k-th source (the voxels with intensity less than 10% of the global maximum are not considered) and let d_{ki} be the distance between the i-th voxel to the peak of the k-th true source. The LE_k and LE can then be expressed as

$$LE = \frac{1}{K}\sum_k LE_k, \quad LE_k = \{d_{ki} \,|\, i = \operatorname*{argmax}_{i' \in I_k} \|u_{i'}\|_2\}.$$

(c) *Degree of focalization* (DF), which describes how focal the reconstructed source is. It is defined as the energy ratio between the reconstructed and the true source in the true source area [IAJ03]

$$DF = \frac{\|\hat{u}_S\|_2^2}{\|u_S\|_2^2},$$

where u_S is u restricted to the true source area S. The higher the DF, the more focalized the reconstructed source will be. A perfect reconstruction has a DF of 100%.

2.4 Effect of Various Factors on EEG Brain Imaging

There are many factors that may influence the accuracy of the reconstructed brain image, such as the electrode number, noise level, and inverse methods. After studying the influence of various factors using Monte Carlo Simulation, we find that the accuracy of brain image can be improved by increasing electrode number, improving signal-to-noise-ratio (SNR) and

using better inverse algorithms. In Fig. 2.2 (top), we compare the performance of different inverse methods, including MNE, sLORETA, WMNE and FOCUSS, with different electrode numbers. We can see that increasing electrode number, and using better inverse methods can improve the accuracy of the reconstructed brain image. Fig. 2.2 (bottom) shows the performance of the inverse method MNE under different noise levels and with different electrode numbers. One can see that increasing electrode number and improving SNR helps to improve the brain imaging performance, in terms of relative error, degree of focalization, and localization error. Therefore, to obtain a more precise brain image, we can increase electrode number by using a dense electrode array, reduce the electronics noise by designing better electronics, or develop a better inverse imaging algorithm.

During the past two decades, electrode systems with 64$\sim$256 electrodes (electrode pitch at $\sim$2 cm) were adopted in scientific research and clinics [GBC90, Tuc93]. Recently, the ultra-high density electrode system is becoming increasingly interesting [FHB03, RFH09, OFC13, PNH14], and researchers have tried to use small sized dense array (less than 64 electrodes) to demonstrate the concept and its advantages of ultra-dense electrodes [FHB03, OFC13, PNH14]. However, no one has developed an ultra-dense electrode array that is able to cover a large portion of the whole head. We propose to develop an ultra-dense electrode array (500$\sim$5,000 electrodes for EEG, 10,000 electrodes for ECoG) to fully capture the functional brain information with high temporal and spatial resolution, illustrated in Fig. 2.3 [LLQ15]. In addition, we have developed several novel brain imaging algorithms to improve the brain image reconstruction accuracy, which will be presented in Chapters 3 and 4.

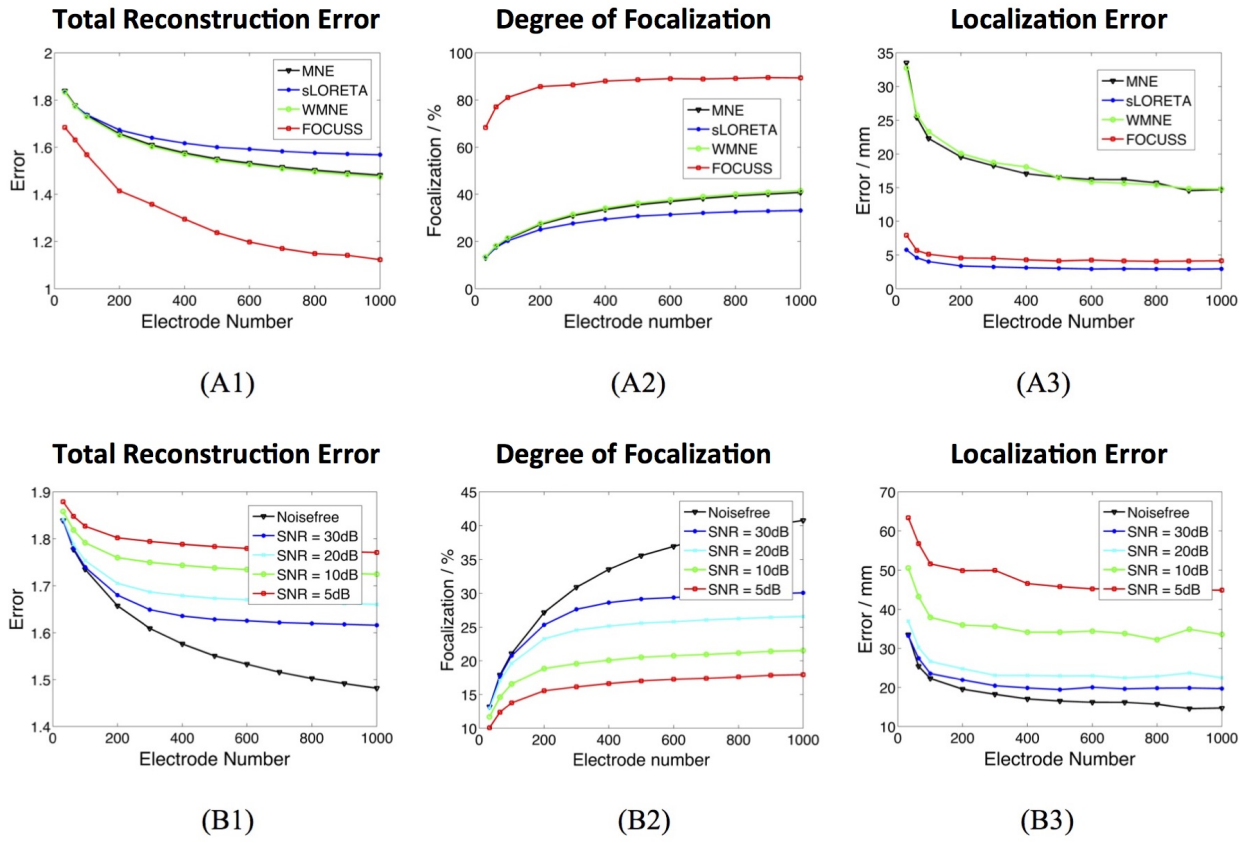

Figure 2.2: Top: comparison of different inverse algorithms with different electrode numbers (noise-free). One can see that more electrodes and better inverse methods help to improve the reconstruction accuracy. Bottom: performance of the inverse method MNE under different noise levels. One can see that more electrodes and better SNR result in higher reconstruction accuracy.

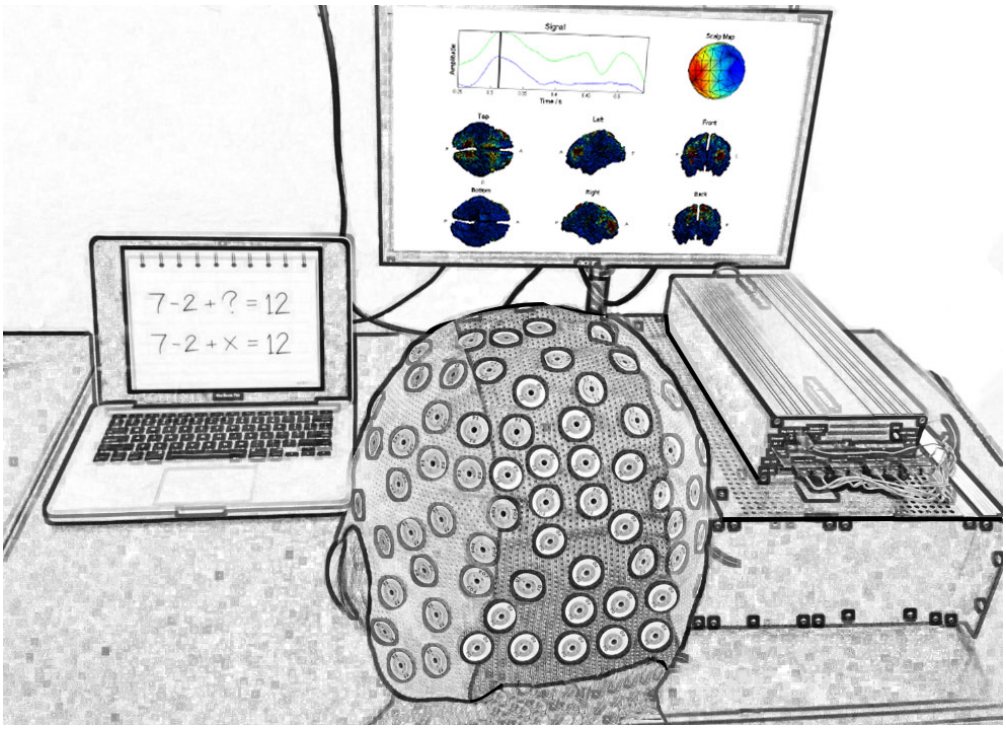

Figure 2.3: Illustration of the ultra-dense electrode-based brain imaging system.

CHAPTER 3

Variational EEG Brain Image Reconstruction

In the previous chapter, we introduce the background of EEG brain imaging, and explain the importance of an appropriate choice of regularization for the brain image reconstruction accuracy. In this chapter, we present a novel Sparsity and SMOOthness enhanced brain TomograpHy (s-SMOOTH) method to improve the reconstruction accuracy by integrating two recently proposed regularization techniques: Total Generalized Variation (TGV) regularization and ℓ_{1-2} regularization. TGV is able to preserve the source edge and recover the spatial distribution of the source intensity with high accuracy. Compared to the relevant total variation (TV) regularization, TGV enhances the smoothness of the image and reduces staircasing artifacts. The traditional TGV defined on a 2D image has been widely used in the image processing field. In order to handle 3D EEG source images, we propose a voxel-based TGV (vTGV) regularization that extends the definition of second-order TGV from 2D planar images to 3D irregular surfaces such as cortex surface. In addition, the ℓ_{1-2} regularization is utilized to promote sparsity on the current density itself. We demonstrate that ℓ_{1-2} regularization is able to enhance sparsity and accelerate computations than ℓ_1 regularization. The proposed model is solved by an efficient and robust algorithm based on the difference of convex functions algorithm (DCA) and the alternating direction method of multipliers (ADMM). Numerical experiments using synthetic data demonstrate the advantages of the proposed method over other state-of-the-art methods in terms of total reconstruction accuracy, localization accuracy, and focalization degree. The application to the source localization of event-related potential data further demonstrates the performance of the proposed method in real-world scenarios.

3.1 Sparsity on High Order Spatial Derivative: Total Generalized Variation (TGV)

In Chapter 2, we introduce a variational method - total variation (TV) which assumes the current density of the sources is piecewise constant, and imposes sparsity on first-order spatial derivative. The TV-based brain imaging method has the limitation that the reconstructed intensity of the source is almost uniform (staircasing artifacts), therefore it has difficulty of localizing the source peak accurately. To overcome this limitation, TGV was proposed to preserve high order of smoothness in image processing problems [BKP10]. Based on the assumption that the underlying image is piecewise polynomial, TGV exploits sparsity of high order derivatives along the x-axis and the y-axis. For the illustrative purpose, we display in Fig. 3.1 various piecewise polynomials defined on a plane with degree up to two. Given a 2D image u twice continuously differentiable on a bounded set $\overline{\Omega} \subset \mathbb{R}^2$, the second order TGV of u with the coefficient $\alpha = (\alpha_1, \alpha_2)$ can be defined as the following infimal convolution [BKP10, GQY14]

$$\mathrm{TGV}^2_\alpha(u) = \min_{p=(p_1,p_2)\in(C^2(\overline{\Omega},\mathbb{R}))^2} \alpha_1 \left\|\nabla u - p\right\|_1 + \alpha_2 \left\|\widetilde{\mathcal{E}}(p)\right\|_1, \tag{3.1}$$

where ∇ is the 2D gradient operator, p is an auxiliary variable, and the operator $\widetilde{\mathcal{E}}$ is defined by

$$\widetilde{\mathcal{E}}(p) = \begin{bmatrix} \frac{\partial p_1}{\partial x} & \frac{1}{2}(\frac{\partial p_2}{\partial x} + \frac{\partial p_1}{\partial y}) \\ \frac{1}{2}(\frac{\partial p_2}{\partial x} + \frac{\partial p_1}{\partial y}) & \frac{\partial p_2}{\partial y} \end{bmatrix}. \tag{3.2}$$

Here the ℓ_1-norm of a matrix treats a matrix as a vector, i.e., $\|X\|_1 = \sum_{i,j} |X_{i,j}|$. Unlike the Laplacian operator which only involves all unmixed second partial derivatives, the second-order TGV involves all partial derivatives, similar to Hessian. In Eq. (3.1), when ∇u is equal to p, the first term in the objective function becomes zero and $\widetilde{\mathcal{E}}$ becomes the Hessian of u. Therefore, one can see that $TGV(u) \leq \|\mathcal{H}(u)\|_1$ where $\mathcal{H}(u)$ is the Hessian of u. This suggests that TGV could yield a faster minimizing sequence than $\|\mathcal{H}(u)\|_1$; therefore, it is a better choice as a regularization term for imposing sparsity than the ℓ_1-norm of Hessian in terms of convergence rate.

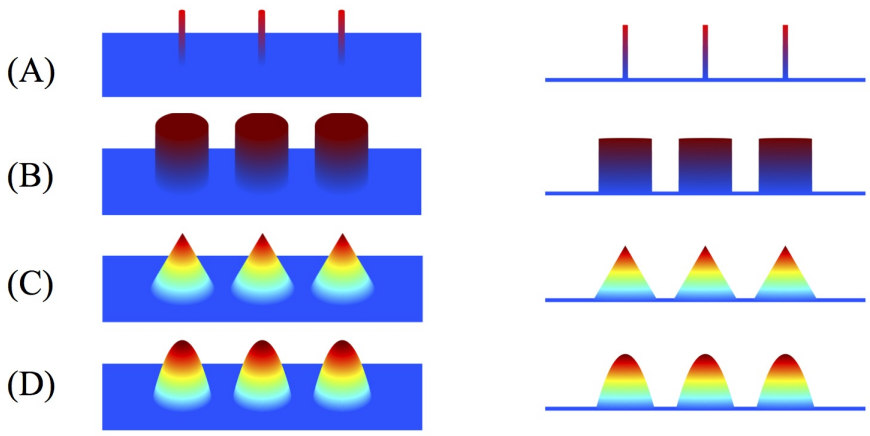

Figure 3.1: Illustration of piecewise polynomial current densities in 3D view and side view. From top to bottom: impulse (sparse in itself), piecewise constant (sparse in first spatial derivative), piecewise linear (sparse in second derivative), piecewise quadratic (sparse in third derivative).

3.2 Voxel-based Total Generalized Variation (vTGV) for Smoothness Enhancement

Since the cortex surface has complicated geometries and topological structures, it is crucial to choose an appropriate regularization tailored to such kind of irregular surfaces. We discretize the cortex surface to be a 3D triangular mesh Ω and define a voxel-based TGV (vTGV) regularization on it. In order to define directional derivatives on triangular mesh, we treat the centroid of each triangle as a dipole. From now on, we treat each triangle as one voxel in the discretized source space, and the terms triangle and voxel are used interchangeably. Since each voxel has three voxels connected to it, three directional derivatives on $\mathbb{R}^3$ can be used to define "gradient" of the density function u. Consider a triangular voxel $\Lambda \in \Omega$, which is homeomorphic to $\mathbb{R}^2$; we assume that q_1, q_2, q_3 are three normal directions along three edges for Λ, where $q_i \in \mathbb{R}^3$ depends on the shape of the triangle Λ. For instance, Fig. 3.2 illustrates three normal directions associated with a triangular voxel. Although not perpendicular to each other, these three directions can span the tangent plane through each voxel and thereby can be used to fully describe variations of u. The gradient of u restricted

on Λ is defined by

$$\widehat{\nabla} u = \begin{bmatrix} \frac{\partial u}{\partial q_1} \\ \frac{\partial u}{\partial q_2} \\ \frac{\partial u}{\partial q_3} \end{bmatrix}, \quad \frac{\partial u}{\partial q_i} = \lim_{\substack{h \to 0 \\ x, x+hq_i \in \Lambda}} \frac{u(x+hq_i) - u(x)}{h}. \tag{3.3}$$

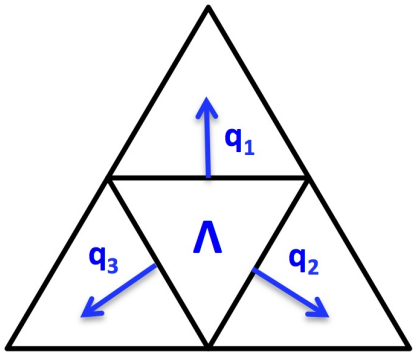

Figure 3.2: Illustration of three normal directions to a triangular voxel Λ.

Note that this definition is in the local sense and it can be considered as an extension of the gradient operator in $\mathbb{R}^2$ into the gradient in a 2D manifold. Given a differentiable function $p = (p_1, p_2, p_3)$, the operator $\mathcal{E}$ acting on p restricted to Λ is defined by

$$\mathcal{E}(p) = \begin{bmatrix} \frac{\partial p_1}{\partial q_1} & \frac{1}{2}(\frac{\partial p_2}{\partial q_1} + \frac{\partial p_1}{\partial q_2}) & \frac{1}{2}(\frac{\partial p_3}{\partial q_1} + \frac{\partial p_1}{\partial q_3}) \\ \frac{1}{2}(\frac{\partial p_1}{\partial q_2} + \frac{\partial p_2}{\partial q_1}) & \frac{\partial p_2}{\partial q_2} & \frac{1}{2}(\frac{\partial p_3}{\partial q_2} + \frac{\partial p_2}{\partial q_3}) \\ \frac{1}{2}(\frac{\partial p_1}{\partial q_3} + \frac{\partial p_3}{\partial q_1}) & \frac{1}{2}(\frac{\partial p_2}{\partial q_3} + \frac{\partial p_3}{\partial q_2}) & \frac{\partial p_3}{\partial q_3} \end{bmatrix}. \tag{3.4}$$

This operator can be considered as an extension of $\widetilde{\mathcal{E}}$ in Eq. (3.2) tailored to the triangular mesh Ω.

Next, we discuss the discretization of the operators $\widehat{\nabla}$ and $\mathcal{E}$. On the triangular mesh Ω with M voxels, we first index all voxels and then define a finite difference operator matrix $D \in \mathbb{R}^{3M \times M}$ as follows. The (i,j)-th entry of D is defined as

$$D_{i,j} = \begin{cases} 1, & \text{if } j = l; \\ -1, & \text{if } j \in \{k_{l,1}, k_{l,2}, k_{l,3}\}; \\ 0, & \text{otherwise,} \end{cases} \tag{3.5}$$

where the voxel index is $l = \lceil i/3 \rceil \in \{1, \ldots, M\}$, i.e., the smallest integer no less than $i/3$, and $k_{l,1}$, $k_{l,2}$ and $k_{l,3}$ are the indices of the voxels adjacent to the l-th voxel. Based on the definition in Eq. (3.4), the discretization of the operator $\mathcal{E}$ is defined as $E \in \mathbb{R}^{3M \times 3M}$ of the form

$$E = \frac{1}{2}(\widehat{D} + \widehat{D}^T), \quad \text{where} \quad \widehat{D} = I_{1\times 3} \otimes D, \quad \text{and} \quad I_{1\times 3} = \begin{bmatrix} 1 & 1 & 1 \end{bmatrix}, \tag{3.6}$$

where $\otimes$ is the Kronecker product of two matrices. Note that each edge is counted twice in Eq. (3.5) so that the operator E can be easily constructed by using D. Moreover, E is symmetrized by taking the average between $\widehat{D}$ and its transpose.

One can see that $\widehat{\nabla} u$ is discretized by Du, and $\mathcal{E}(p)$ is discretized by Ep. Once D and E are available, TV and the second order vTGV with the coefficients α_1 and α_2 can be defined as

$$\mathrm{TV}(u) = \|Du\|_1 , \tag{3.7}$$

$$\mathrm{vTGV}^2_{(\alpha_1,\alpha_2)}(u) = \min_{p \in \mathbb{R}^{3M}} \alpha_1 \|Du - p\|_1 + \alpha_2 \|Ep\|_1 . \tag{3.8}$$

In Eq. (3.8), the parameters α_1 and α_2 balance the first and second order derivative information of the image [PV15]. It has been proven that for a large ratio α_2/α_1, the second order TGV coincides with TV under certain conditions [PV15].

TV is able to well preserve the edges of images, but is known to create piecewise constant result even in regions with smoothly changed intensities [BBB13]. By considering higher-order derivative information, TGV generalizes TV and is able to reduce staircasing effects by assuming that the image to be reconstructed is piecewise polynomial (including piecewise constant, piecewise linear, piecewise quadratic, etc.)[BH14]. In particular, the proposed second order vTGV assumes that the underlying current density distribution is piecewise linear, and thereby this regularization is able to enforce the sparsity of second spatial derivatives. Although a natural image may have higher order smoothness, it is usually sufficient to use the second order vTGV in practice, since performance enhancement is limited but more computations are required for higher order vTGV. Therefore, we only use the second order vTGV regularization in this work.

3.3 L_{1-2} Regularization for Sparsity Enhancement

In order to further improve the spatial resolution of the brain image, sparsity constraint can be incorporated into the model. Previous work incorporate ℓ_1 regularizations to further impose sparsity on the current density [HNZ08, CNH10, SLW16]. Recently, ℓ_{1-2} regularization has been proposed [ELX13, YEX14, LYH15], and has been shown to provide a sparser result than the widely used ℓ_1-norm regularization. The ℓ_{1-2} regularization penalty function is defined as

$$\|u\|_{1-2,\beta} = \|u\|_1 - \beta \|u\|_2, \quad 0 < \beta \leq 1, \tag{3.9}$$

which has shown potential in image processing and compressive sensing reconstruction [LYH15, YLH15] in terms of sparsity and fast convergence. It promotes sparsity of an image, and achieves the smallest value when only one voxel in the image is non-zero.

We further discuss the property of ℓ_{1-2} regularization from the optimization point of view. Consider a minimization problem in 2D $\min_{x\in\mathbb{R}^2} R(x)$ subject to the linear constraint $Ax = b$ where $R(x)$ is a regularization function. To solve the problem graphically, we need to find the level curve of minimum radius to the origin that intersects with the line $L : Ax = b$. Fig. 3.3 illustrates the solutions when R is ℓ_2, ℓ_1, $\ell_{0.001}$ (used to approximate ℓ_0) and ℓ_{1-2} when $\beta = 1$, respectively. As shown in Fig 3.3(A), the ℓ_2-regularized solution rarely has zero components, indicating that the solution is usually non-sparse. The ℓ_1-regularized solution may not be sparse if the line L is parallel to the level curves. Compared to ℓ_p $(0 < p < 1)$ regularization, the ℓ_{1-2} regularization is more likely to yield a sparse solution due to the curvature of level curves. Therefore, the ℓ_{1-2} regularization promotes sparser solutions than the other regularizations being compared. In the EEG inverse problem, the brain images to be reconstructed in general have a sparse structure that the number of sources is limited, which motivates us to apply the ℓ_{1-2} regularization to solve this problem.

In this work, we unify the ℓ_1 type and the ℓ_{1-2} type regularizations by allowing $\beta = 0$ in Eq. (3.9), so that the sparsity regularization term could be adjusted by tuning the parameter β.

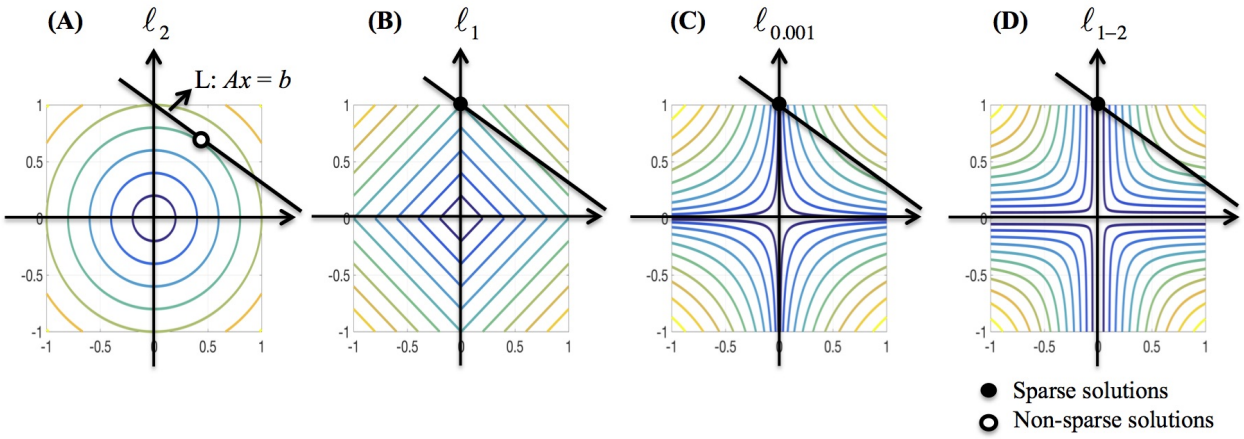

Figure 3.3: Geometric interpretation of sparsity for various regularizations. From left to right: ℓ_2, ℓ_1, $\ell_{0.001}$ (used to approximate ℓ_0), and ℓ_{1-2} when $\beta = 1$. The black line corresponds to the linear constraint, the solid dot specifies the sparse solution and the circular dot specifies the non-sparse solution.

3.4 s-SMOOTH: Sparsity and Smoothness Enhanced Brain Tomography

3.4.1 Formulation and Algorithm

3.4.1.1 Proposed EEG Reconstruction Algorithm

In this method, we combine the vTGV and ℓ_{1-2} regularizations:

The following model is proposed to reconstruct the EEG brain image u

$$\min_u \frac{1}{2} \|Au - b\|_2^2 + \mathrm{vTGV}^2_{(\alpha_1,\alpha_2)}(u) + \alpha_3 \|u\|_{1-2,\beta}\,, \tag{3.10}$$

where $\mathrm{vTGV}^2_{(\alpha_1,\alpha_2)}(u)$ is defined in Eq. (3.8), and $\|u\|_{1-2,\beta}$ is defined in Eq. (3.9). Here, $\alpha_i > 0$ are regularization parameters which control the contribution of each regularization term. Note that if $\beta = 0$, the ℓ_{1-2} regularization reduces to the ℓ_1 regularization. If we require $p = \mathbf{0}$, then the vTGV regularization reduces to the TV.

Since the dual norm of $\|\cdot\|_2$ is itself, i.e., $\|u\|_2 = \max_{\|q\|_2 \le 1} \langle u, q \rangle$, the model Eq. (3.10)

can be reformulated as

$$\min_{u,p,\|q\|_2\leq 1} \frac{1}{2}\|Au-b\|_2^2+\alpha_1\|Du-p\|_1+\alpha_2\|Ep\|_1+\alpha_3(\|u\|_1-\beta\langle u,q\rangle). \tag{3.11}$$

Next, we apply the difference of convex function algorithm (DCA) [TA97] to obtain the following two subproblems

$$\begin{cases} q \leftarrow u/\|u\|_2, \\ (u,p) \leftarrow \operatorname*{argmin}_{u,p} \frac{1}{2}\|Au-b\|_2^2+\alpha_1\|Du-p\|_1+\alpha_2\|Ep\|_1+\alpha_3(\|u\|_1-\beta\langle u,q\rangle). \end{cases} \tag{3.12}$$

In particular, the second subproblem can be solved efficiently using ADMM. By the change of variables, it can be further written as

$$\begin{aligned} &\min_{u,p,x,y,z} \frac{1}{2}\|Au-b\|_2^2+\alpha_1\|x\|_1+\alpha_2\|y\|_1+\alpha_3(\|z\|_1-\beta\langle z,q\rangle) \\ &\qquad \text{subject to} \quad x=Du-p,\ y=Ep,\ z=u. \end{aligned}$$

By introducing the scaled multipliers $\tilde{x},\tilde{y},\tilde{z}$, we have the following augmented Lagrangian function

$$\begin{aligned} \mathcal{L}(u,p,x,y,z,\tilde{x},\tilde{y},\tilde{z}) &= \frac{1}{2}\|Au-b\|_2^2+\alpha_1\|x\|_1+\alpha_2\|y\|_1+\alpha_3(\|z\|_1-\beta\langle z,q\rangle) \\ &+\frac{\rho}{2}\left(\|Du-p-x\|_2^2+2\langle Du-p-x,\tilde{x}\rangle+\|Ep-y\|_2^2+2\langle Ep-y,\tilde{y}\rangle+\|u-z\|_2^2+2\langle u-z,\tilde{z}\rangle\right). \end{aligned}$$

Note that this version is equivalent to the standard augmented Lagrangian function up to scaling of multipliers. We group the variables u,p,x,y,z into three blocks, i.e., u, p and (x,y,z). Then the ADMM yields the following algorithm:

$$\begin{cases} u \leftarrow \operatorname*{argmin}_{u} \mathcal{L}(u,p,x,y,z,\tilde{x},\tilde{y},\tilde{z}) \\ p \leftarrow \operatorname*{argmin}_{p} \mathcal{L}(u,p,x,y,z,\tilde{x},\tilde{y},\tilde{z}) \\ (x,y,z) \leftarrow \operatorname*{argmin}_{x,y,z} \mathcal{L}(u,p,x,y,z,\tilde{x},\tilde{y},\tilde{z}) \\ \tilde{x} \leftarrow \tilde{x}+Du-p-x \\ \tilde{y} \leftarrow \tilde{y}+Ep-y \\ \tilde{z} \leftarrow \tilde{z}+u-z+\dfrac{\alpha_3\beta}{\rho}q \end{cases} \tag{3.13}$$

Moreover, u and p can be solved explicitly as follows

$$\begin{cases} u = \big(A^TA + \rho(D^TD + I)\big)^{-1}\big(A^Tb + \rho D^T(p + x - \tilde{x}) + \rho(z - \tilde{z})\big) \\ p = (E^TE + I)^{-1}\big(E^T(y - \tilde{y}) + (Du - x + \tilde{x})\big). \end{cases}$$

In addition, due to the separability of variables, the (x, y, z)-subproblem boils down to three independent subproblems with respect to x, y and z, respectively, each of which has a closed-form solution represented by proximal operators. For example, the z-subproblem can be solved by using the proximal operator of ℓ_1-norm

$$\underset{z}{\operatorname{argmin}} \left\{ \alpha_3 \|z\|_1 + \frac{\rho}{2} \left\| u - z + \tilde{z} + \frac{\alpha_3\beta}{\rho} q \right\|^2 \right\} = \operatorname{prox}_{\alpha_3/\rho}(u + \tilde{z} + \frac{\alpha_3\beta}{\rho} q). \tag{3.14}$$

where $\operatorname{prox}_\gamma(x) = \operatorname{sign}(x) \odot \max\{|x| - \gamma, 0\}$ with componentwise multiplication $\odot$, also known as shrinkage operator. Combining DCA for problem Eq. (3.12) and ADMM for the (u, p)-subproblem, we obtain the algorithm summarized in Algorithm 1.

Note that in this study the entire matrix A is scaled by multiplying 10^5 in order to reduce round-off errors. Algorithm 1 terminates when either the maximal number of iterations or the minimal relative change is reached. Note that there are two loops in the algorithm: outer and inner loop. In our experiments, the maximum number of iterations for each inner loop is set to be 40, and the maximum number of outer loop is set to be 10. The algorithm will also be halted if the relative change of u is smaller than 10^{-3}. Here the relative change of u is defined as

$$u_{change} = \frac{\|u_{new} - u_{old}\|_2}{\|u_{old}\|_2}. \tag{3.15}$$

In general, ADMM is simple to implement with linear convergence even if part of the objective function is nondifferentiable. Our empirical experience shows that the ℓ_{1-2} regularization further promotes faster convergence of the algorithm than its ℓ_1-regularized counterpart.

3.4.1.2 Parameter Selection

In the proposed Algorithm 1, the regularization parameters $\alpha_1, \alpha_2, \alpha_3$ are selected to make a balance between smoothness and sparsity. Based on our large numbers of experiments, the optimal parameter selection does not change significantly as the source number, size,

Algorithm 1 s-SMOOTH EEG Reconstruction Algorithm

Input: the data b, the sensing matrix A, difference operators D, E, parameters $\alpha_1, \alpha_2, \alpha_3 > 0$ and $\beta \in [0, 1]$, the maximal number of iterations for the outer loop N_{out}, and the maximal number of iterations for the inner loop N_{in}.

Output: the reconstructed u_o.

if $\beta = 0$ **then**

$N_{out} \leftarrow 0$

end if

Initialize $u_o = \mathbf{0}$.

for 1 to N_{out} **do**

if $u_o = \mathbf{0}$ **then**

$q \leftarrow \mathbf{0}$

else

$q \leftarrow u_o / \|u_o\|_2$

end if

Initialize $p, x, y, z, \tilde{x}, \tilde{y}, \tilde{z}$ as zero vectors

for 1 to N_{in} **do**

$u \leftarrow (A^T A + \rho(D^T D + I))^{-1} \left[A^T b + \rho D^T (p + x - \tilde{x}) + \rho(z - \tilde{z})\right]$

$p \leftarrow (E^T E + I)^{-1} \left[E^T (y - \tilde{y}) + (Du - x + \tilde{x})\right]$

$x \leftarrow \text{prox}_{\alpha_1/\rho}(Du - p + \tilde{x})$

$y \leftarrow \text{prox}_{\alpha_2/\rho}(Ep + \tilde{y})$

$z \leftarrow \text{prox}_{\alpha_3/\rho}(u + \tilde{z} + \dfrac{\alpha_3 \beta}{\rho} q)$

$\tilde{x} \leftarrow \tilde{x} + Du - p - x$

$\tilde{y} \leftarrow \tilde{y} + Ep - y$

$\tilde{z} \leftarrow \tilde{z} + u - z + \dfrac{\alpha_3 \beta}{\rho} q$

end for

$u_o \leftarrow u$

end for

or configuration changes. For different noise levels, the regularization parameters need to be tuned smaller when SNR increases. Table 3.1 lists all values of α_1 that we use for the synthetic data sets with SNR between 0dB and 30dB. For simplicity, we set α_2 to be equal to α_1. A more detailed discussion about the influence of ratio α_2/α_1 on the reconstruction results can be found in [PV15]. For α_3, we find that the performance of the proposed method is not sensitive to α_3 as long as it is in the range of $\alpha_3 = 0.1 \sim 0.5\alpha_1$. Fig. 3.4 illustrates the source reconstruction results with different values of α_3, where we can see that the results look very similar. By taking a careful look at the bottom source, one can see that $\alpha_3 = 0.1\alpha_1$ yields slightly under-focalized result, while $\alpha_3 = 0.4\alpha_1$ yields slightly over-focalized result, so $\alpha_3 = 0.2$ or 0.3 α_1 provides results closest to the ground truth. In our experiment, we fix α_3 to be $0.3\alpha_1$ in all test cases. As for the parameter ρ, which controls the convergence speed of Algorithm 1, it is set to $10\alpha_1$ by default. For real data sets, we use the same parameters for the same noise level as the synthetic data.

Table 3.1: Parameter α_1 used in different noise levels.

SNR(dB)	0	5	10	15	20	25	30
α_1 (*10)	7	6	5	3	2	2	1

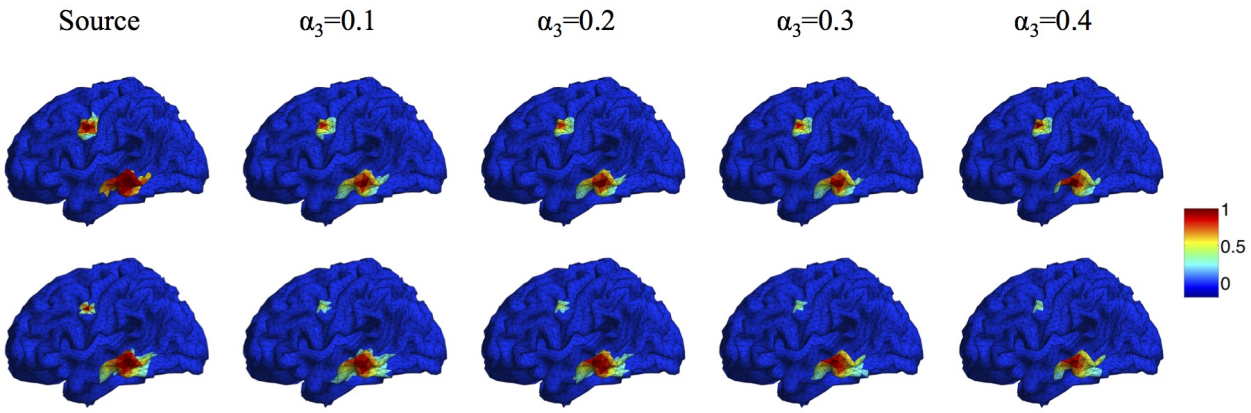

Figure 3.4: Source localization results with different α_3. Top: two sources with different configurations. Bottom: two sources with different sizes.

The parameter β in the ℓ_{1-2} regularization term varies from 0 to 1. When $\beta = 0$, the ℓ_{1-2} regularization becomes the ℓ_1 regularization. In Fig. 3.5, we study the effect of β on the source reconstruction results. Fig. 3.5(B) shows the change of reconstruction error with different values of β, where we can see that the larger β is, the smaller the reconstruction error will be. When $\beta = 1$, the highest reconstruction accuracy is achieved. Fig. 3.5(C) shows the change of the sparsity term as iteration increases. One can see that comparing to $\beta = 0$ (ℓ_1 regularization), $\beta = 1$ (ℓ_{1-2} regularization) helps to promote sparsity. Notice that the sparsity term will decrease rapidly from one inner loop to another since the variable q is redefined in each outer loop. In our experiments, the maximal number of iterations at each inner loop is set to 40. At each inner loop, the solution becomes convergent and stable within the tolerance, so does the sparsity term. Then at the iteration 41, the updated q results in the refinement of the solution and a large drop of the sparsity term (Fig. 3.5(C)). In sum, $\beta = 1$ not only helps reduce the reconstruction error, but also enhances the sparsity term. Therefore , we set β to 1 in the following study.

3.4.1.3 Computational Cost

In Algorithm 1, the two least squares subproblems involve matrix inverse which is computationally intensive. Instead of computing inverses of $P = A^T A + \rho(D^T D + I)$ and $Q = E^T E + I$ directly, we apply the Cholesky decomposition and then solve linear systems using backward/forward substitution, i.e., `mldivide` in MATLAB. In addition, since the construction of P and Q does not depend on the time points, we can further reduce computational time by performing Cholesky decomposition once and saving results for all time points. For instance, when using 10240 voxels and running 100 iterations, the running time on a desktop with 3.4GHz CPU and 16G memory using MATLAB 2014b is reduced from 3.5 min to 1.8 min.

Further, if we reduce the number of voxels to 6000, it takes about 11 s to run 100 iterations, and only 6.4 s if the matrices are pre-computed. If further decreasing the voxel number to be 2000, the computation time is reduced to 1.2 s, or 0.9 s with pre-computed

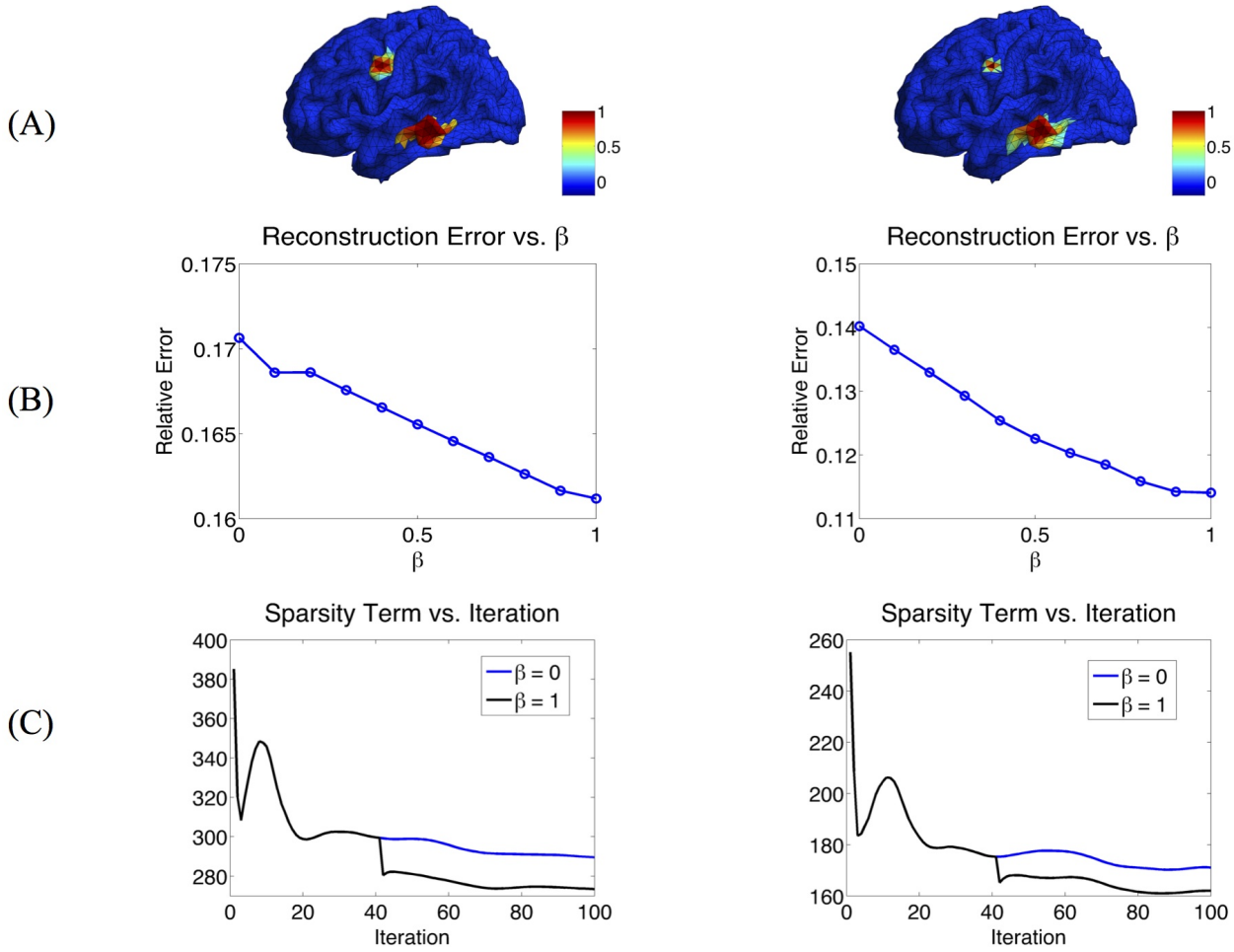

Figure 3.5: Influence of β on the image reconstruction results. (A) Two simulated sources. (B) Influence of β on the reconstruction error. The larger the β, the smaller the reconstruction error will be. (C) Influence of β on the sparsity term. $\beta = 1$ enhances the sparsity compared to $\beta = 0$.

matrices. Compared to relevant work [HNZ08, CNH10, SLW16], the proposed algorithm has reduced the computational cost significantly.

3.4.2 Simulation Experiments and Results

3.4.2.1 Synthetic Data Simulation

In our simulation, source is synthesized using the Gaussian-tapered patch. Firstly, a source center is seeded on the cortex surface, then its neighbors are gradually recruited to make

a patch. Because the Gaussian function has bell shape, the source intensity distribution reaches a peak at the center and gradually decreases to zero as it moves away from the center. To model different source configurations, we use Gaussian functions with different variations (σ^2), illustrated in Fig. 3.6. As σ^2 goes to infinity, the intensity of the source decays more and more slowly from the center to its neighbors and approximates the constant function.

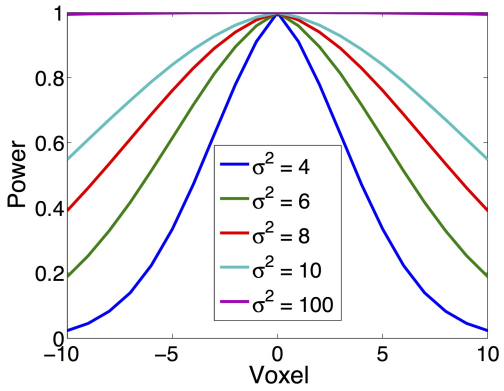

Figure 3.6: Various source configurations (side view) with a shape of Gaussian function of different σ^2.

In addition to various source configurations, we test a variety of sources with different sizes. Specifically, we use the sources containing 100∼300 triangular voxels, which corresponds to 1.4∼2.2cm in radius. To study the sensitivity of the result to the measurement noise, we add i.i.d. additive white Gaussian noise to each channel. We also study the influence of the brain noise by adding i.i.d. Gaussian additive noise to the voxel space. As a widely used criterion for noise level measurement, the signal-to-noise ratio (SNR) is defined as

$$SNR = 10 \log_{10} \frac{P_{signal}}{P_{noise}},$$

where P_{signal} and P_{noise} are the power of the signal and the noise, respectively. In our simulation, SNR is set to 20dB by default. The effect of different noise levels is also studied by using signals of SNR 0∼20dB. The synthetic signal is normalized to make sure that the amplitude of the signal falls into the range from 10 μV to 100 μV, which is the typical EEG signal amplitude of an adult human [AGA04]. For synthetic data, we use the head model

template provided by Fieldtrip [OSP03], where the number of voxels M is equal to 10240.

3.4.2.2 Performance Comparison with State-of-the-art Methods

We compare the proposed method s-SMOOTH with four representative source localization methods in the literature: MNE, sLORETA, minimum ℓ_1 method ("L1" for short) and TV-ℓ_1. Fig. 3.7 shows the reconstructed brain image of three synthetic sources, where the source intensity is scaled to be in [0 1]. A threshold is set at 20% of the maximum intensity, i.e., voxel intensity less than the threshold will be set to 0, so as to obtain a better visualization. For MNE and sLORETA which are minimum ℓ_2 methods, one can see the reconstructed sources are spread out with a lot of spurious sources around the sources. The intensity of adjacent voxels has large jumps since these two methods do not consider the spatial relation between neighboring voxels. Regarding L1 method, the focalization of the reconstructed source is greatly improved. However, the sources are over-focused that only a few voxels are included in the area of the true sources. Compared to L1 method, the TV-ℓ_1 method successfully recovers the extent of sources, but fails to reflect the intensity variation of the sources, as we can see that the intensity of the current density is almost uniform in each source region. In contrast, the proposed method not only eliminates the spurious sources, recovers the extent of the sources, but also provides a smooth result which reflects the magnitude variation of the current density.

3.4.2.3 Sensitivity Study

In this section, we investigate the sensitivity of the proposed method to various factors both qualitatively and quantitatively.

1. Influence of Measurement Noise Level

Fig. 3.8(A) illustrates the source localization results of two sources in nearly noiseless (30dB) and noisy (0dB) cases. In the nearly noiseless case, MNE successfully locates these two sources but produces a few spurious sources. For TV-ℓ_1 method, although we can see a little magnitude variation in the edge of the sources, the main area of the sources still

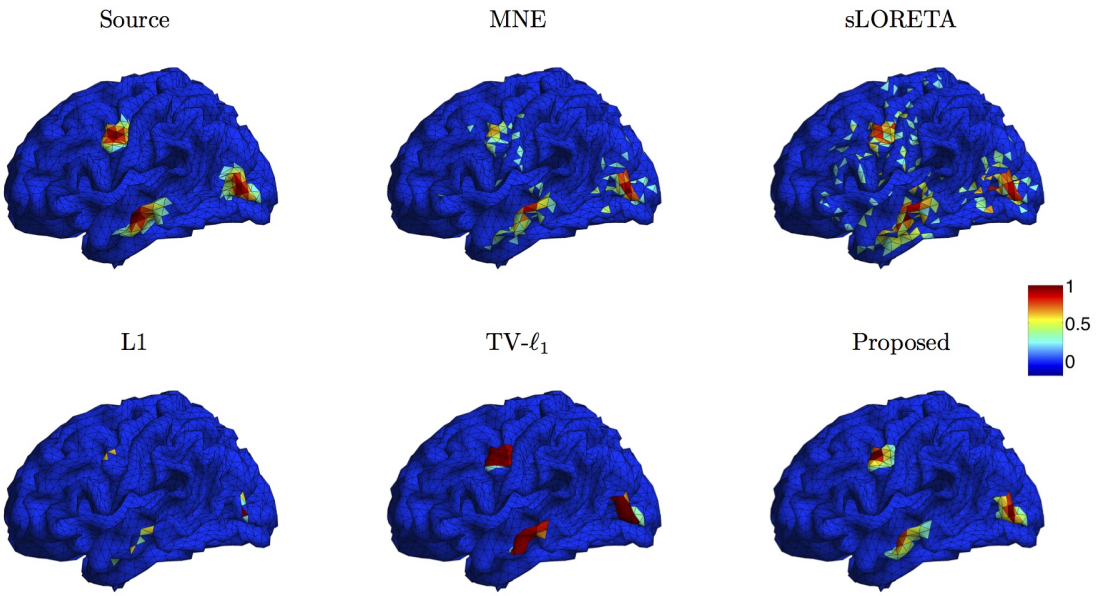

Figure 3.7: Source localization results of various methods on synthetic data with three sources.

shows almost uniform current density distribution. Compared to the other two methods, the proposed method shows the closest result to the ground truth, where the magnitude of the current density varies smoothly from the peak to its neighbors. From the noisy case, one can see that the imaging result is sensitive to measurement noise, especially for the bottom source. MNE shows a lot more spurious sources than the nearly noiseless case even after thresholding. The TV-ℓ_1 method shows an enlarged coverage of the bottom source compared to the ground truth. In addition, one can see that the source intensity becomes more flat in the noisy case. The proposed method is more robust to the noise with the coverage of the bottom source shrinks slightly.

To quantify the influence of noise levels on the source reconstruction performance, we test various noise levels and evaluate the results with the criteria defined above. In order to avoid inconsistency due to different noise configurations, we repeat the experiment 50 times by adding random noise and display the averaged result and the standard deviation in Fig. 3.8(B). Generally, the performance of all the methods is improved as SNR increases. From the TRE plot, one can see that our method has the smallest total reconstruction error compared to the other two methods. The LE plot shows that the proposed method has

the smallest localization error. Compared to the proposed method, the TV-ℓ_1 method has relatively large localization error since it tends to produce an almost uniform current density and thereby has difficulty locating the peak of the source. In the DF plot, both TV-ℓ_1 method and the proposed method show very high focalization degree, this is because they incorporate ℓ_1 or ℓ_{1-2} regularization to impose sparsity on the source current density. Taken together, the proposed method shows good performance for all three quantitative criteria at every noise level.

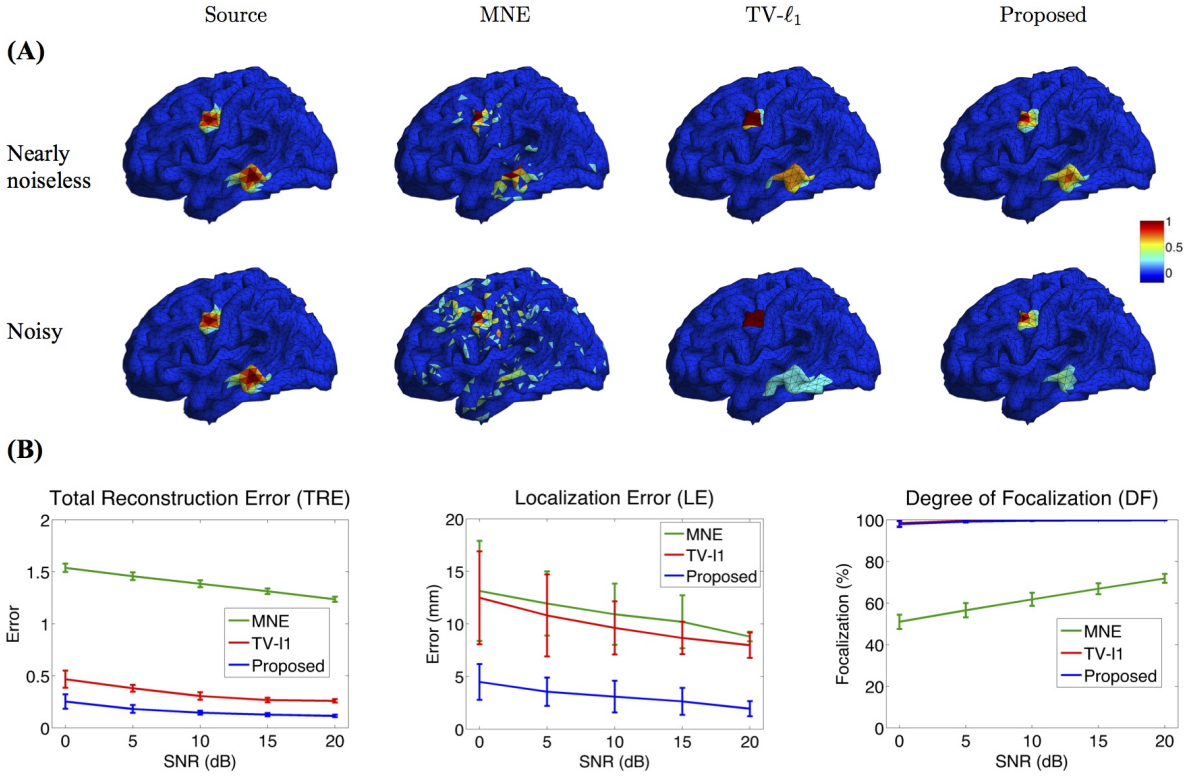

Figure 3.8: Influence of measurement noise. (A) Source localization results in the nearly noiseless (30dB) and noisy (0dB) cases. (B) Quantitative evaluation of various methods under different measurement noise levels. The plots show the average results over 50 repeats, where the error bar represents standard deviation.

2. Influence of Brain Noise Level

In this section, we study the influence of brain noise by adding i.i.d. Gaussian additive noise to each voxel. Fig. 3.9(A) shows the source imaging results in the nearly noiseless (30dB) and noisy (0dB) cases. Note that in this figure the imaging results are not thresholded

so as to better visualize the influence of brain noise. In the nearly noiseless case, MNE produces much less spurious sources under the brain noise than under the measurement noise (Fig. 3.8(A)), indicating that the spurious sources are mainly due to the measurement noise. For the TV-ℓ_1 method, the reconstructed intensity distribution is generally piecewise constant, but we can see that the intensity variation is larger than the result in Fig. 3.8(A). The proposed method produces an accurate source intensity distribution that is very close to the ground truth. In the noisy case, generally the performance of all the methods is affected by the noise. The MNE result shows more background activities due to the high level of noise. The TV-ℓ_1 result shows smaller intensity variation than the nearly noiseless case. For example, for the bottom source, we can see four different intensity colors in the nearly noiseless case, but only two different intensity colors in the noisy case. Compared to the TV-ℓ_1 method, the proposed method provides a smoother result. We can see that the source intensity is weakened due to the high noise level.

Fig. 3.9(B) further quantifies the results using different noise levels. The TRE plot shows that the proposed method has the smallest reconstruction error. In addition, by comparing to the result in Fig. 3.8(B) with the same noise level, one can see that the reconstruction error under brain noise is smaller, which is consistent with the visualization result. The LE plot shows that the proposed method has the smallest localization error. It is worth noting that the localization errors of all the methods are smaller than those with measurement noise (Fig. 3.8(B)). Finally, in the DF plot, both the proposed method and the TV-ℓ_1 method achieve high focalization degree. The focalization degree for MNE is much higher than that under measurement noise. In summary, we observe that the brain imaging result is less sensitive to brain noise than to measurement noise. The proposed method demonstrates robust performance under various levels of brain noise.

3. Influence of Source Size

In addition to noise level, we also investigate the influence of the source size on the reconstruction results. Fig. 3.10(A) illustrates the reconstructed brain image with two sources of different sizes. In MNE, although it locates these two sources at the approximate locations, it is difficult to differentiate the smaller source from the large numbers of spurious

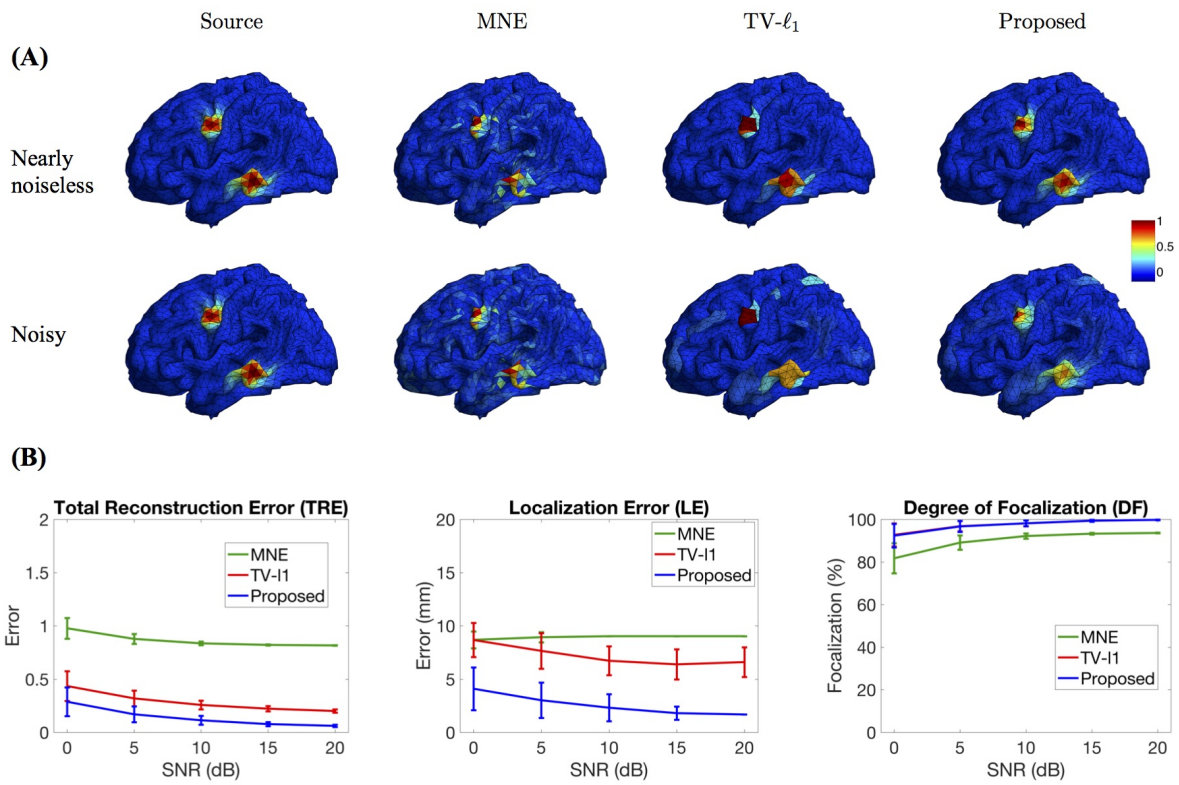

Figure 3.9: Influence of brain noise. (A) Source localization results in the nearly noiseless (30dB) and noisy (0dB) cases. (B) Quantitative evaluation of various methods under different brain noise levels. The plots show the average results across 50 repeats, where the error bar represents standard deviation.

sources. TV-ℓ_1 method recovers both sources clearly without spurious sources, but the coverage of the reconstructed sources is enlarged, especially for the small source on the top. Additionally, it fails to recover the intensity variation of the source in space. In contrast, the proposed method accurately reconstructs the size and intensity variation of these two sources.

Fig. 3.10(B) shows the quantitative results of various source sizes, where the x-axis represents the number of voxels contained in the simulated sources. TRE plot shows that the proposed method has the smallest reconstruction error, which is insensitive to the source size. In the LE plot, the proposed method shows the smallest localization error. As the source size increases, its localization error becomes slightly smaller, which implies that the

proposed method has advantages of dealing with larger sources. The TV-ℓ_1, by contrast, shows relatively large localization error due to the uniform intensity of the reconstructed source. In the DF plot, the proposed method demonstrates very high focalization degree. In summary, the proposed method shows consistent outstanding performance over the other two methods regardless of the source size.

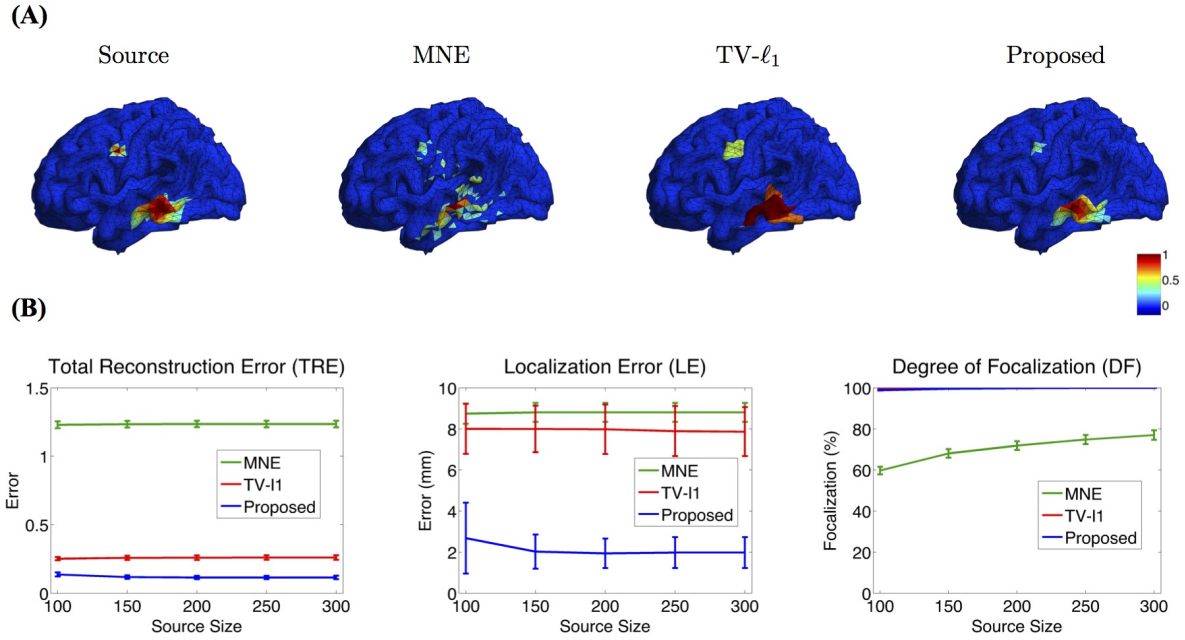

Figure 3.10: Influence of source sizes. (A) Source localization results of various methods for two sources with different source sizes. (B) Quantitative evaluation of various methods with different source sizes. The average result of 50 repeats is shown in the plots, where the error bar represents the standard deviation.

4. Influence of Source Configuration

We study the performance of the proposed method using sources with different decay speeds (see Fig. 3.6). In Fig. 3.11(A), we show two sources of different configurations: the top source decays fast as it goes far from the center while the bottom source decays slowly. From the reconstruction results, one can see that the MNE is not able to tell the configuration difference between these two sources. The TV-ℓ_1 method models the source intensity to be piecewise constant, so both of the reconstructed sources decay very slowly. As for the proposed method, we can tell that the bottom source decays more slowly than

the top one.

We further evaluate the performance of the methods with different source configurations quantitatively. In Fig. 3.11(B), the x-axis represents the variance σ^2 of the Gaussian function (Fig. 3.6), so the source intensity decays faster and faster from left to right. The TRE plot shows that the proposed method has the smallest reconstruction error among all the methods. By comparing the results of different variance σ^2, one can see that the proposed method favors smoother sources whose intensity decays faster, i.e. smaller σ^2. In the LE curve, the proposed method shows much smaller localization error than the other two methods. Again, one can see that the smoother sources have smaller localization errors. Finally, the DF plot shows that the focalization degree does not rely on the source configurations too much. In sum, the proposed method outperforms the other two methods consistently for all three criteria. Compared to constant sources, it favors smoother sources.

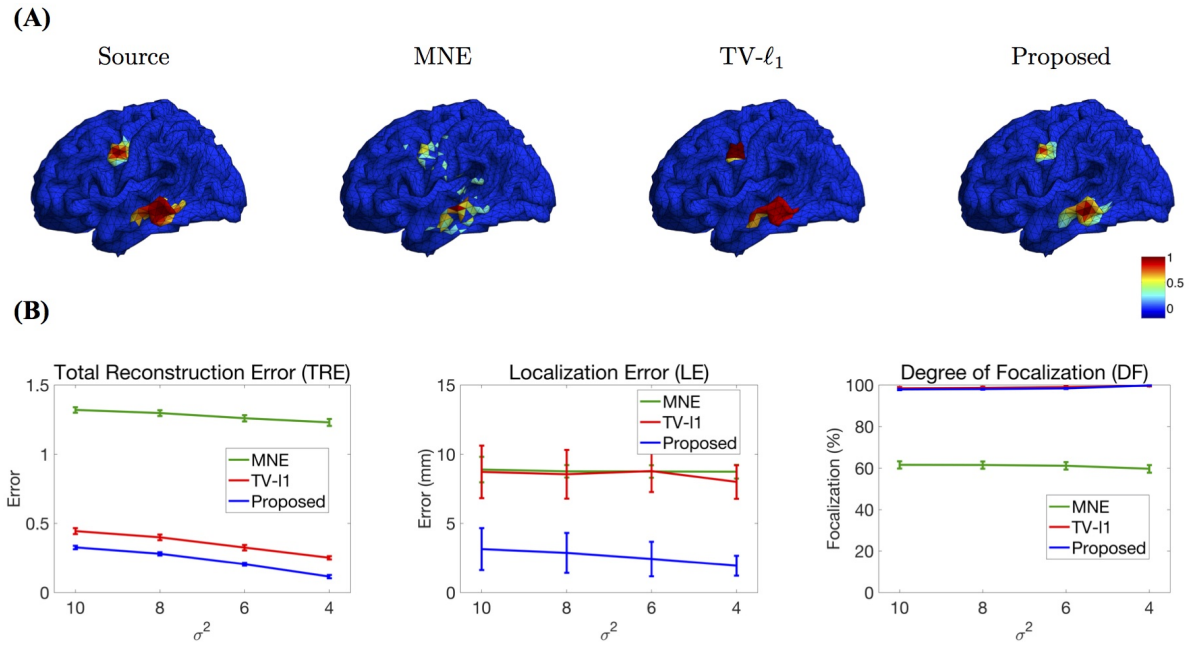

Figure 3.11: Influence of source configurations. (A) Source localization results of two sources data with different configurations. (B) Quantitative results of various methods with different source configurations (σ^2). The average result of 50 repeats is shown in the plots, where the error bar represents the standard deviation.

5. Influence of Source Location

To systematically evaluate the performance of the proposed method for different source locations, we randomly select 50 locations in the whole source space, and test its average performance. Fig. 3.12 displays the whisker plot of the quantitative results, where the lower quartile, median, and upper quartile are shown. In TRE plot, the proposed method shows the best median reconstruction accuracy. The range of the results is relatively large which indicates the performance varies at different locations. The LE plot shows that the localization error of the proposed method has a median value of around 1cm, which is the smallest among all the methods. In addition, the range of its localization error is also the smallest. From the DF plot, one can see that the median focalization degree of the proposed method is $\sim$ 97% which is the highest. All in all, the proposed method shows the best average performance for different source locations among all the compared methods.

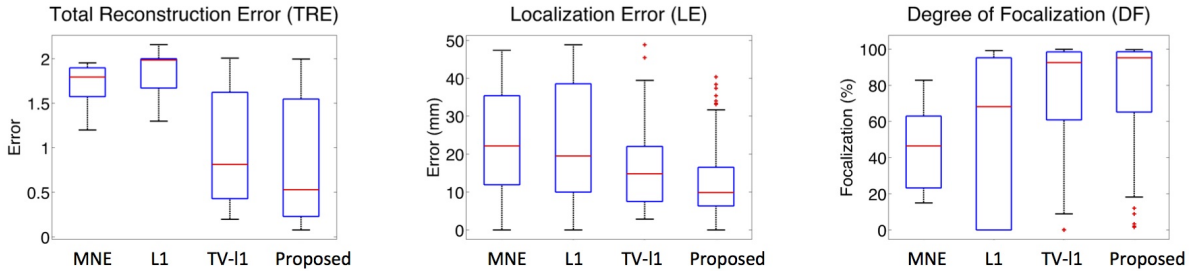

Figure 3.12: Whisker plots of various methods at different source locations. The red bar represents the median value of 50 random locations.

3.4.3 Application to Real Data

To evaluate the performance of the proposed method in realistic scenario, we collected two P300 event-related potentials (ERPs) via auditory and visual oddball paradigms, in which a subject detected an occasional target stimulus in a regular train of sensory stimuli. The experiment was conducted with the approval of institutional review board at Hualien Tzu Chi General Hospital, Taiwan (IRB 101-102) with written informed consent from the subject.

P300 is a positive peak occurring about 300ms or more after a stimulus [Lin05], which reflects information processing associated with attention and memory. In the auditory stimulation setting, two audio signals of 1500 Hz (target, 40 trials) and 1000 Hz frequency

(nontarget, 160 trials) were randomly presented to the subject. In the visual stimulation setting, two different pictures of a fierce shark (40 trials) and of an old man (160 trials) were randomly presented to the subject. The subject was required to detect the targets by silently counting these events. A 64 channels EEG machine (ANT Neuro, Enschede Netherlands) was used to record the neural signals. The EEG data was sampled at 512 Hz, filtered by a band pass filter of 0.5-30 Hz and was referenced to the average of all channels. In the end, the average was taken across the trials in order to improve the SNR, and the difference between the target and nontarget was used for source localization.

In addition to EEG data, high-resolution MRI data (General Electric, Waukesha, WI, USA) were obtained from the subject for realistic head model construction [OFM11]. We first segmented the head into three layers, i.e., scalp, skull and brain, and then constructed a triangular mesh for each layer [OV91, FKW02]. The cortex surface was also triangulated into a fine mesh with 16384 triangles, each corresponding to a potential dipole source. Finally, boundary element method (BEM) [OV91, FKW02] was used to calculate the lead field matrix.

We have applied the proposed s-SMOOTH method to localize the generators of P300 ERPs. Although the neural generators of P300 remain imprecisely located, a consistent pattern of P300 sources has been shown by various techniques - such as intracranial recordings, lesion studies, and fMRI-EEG combination - that the target-related responses locate in the parietal cortex and the cingulate, with stimulus specific sources in the superior temporal cortex for the auditory stimulation and in the inferior temporal, and superior parietal cortex for the visual stimulation [Lin05]. It is shown that there is a significant amplitude difference between target and non-target at latency of 300-400ms for auditory stimulation and of 400-500ms for visual stimulation [LPF99].

We compare the proposed method with various representative methods, including MNE, sLORETA, minimum ℓ_1 method ("L1" for short), and TV-ℓ_1. Among them, sLORETA has been widely used to localize the sources of P300 [SHI09, BKI11, MAS14] due to its high localization accuracy, which can be used as a rough reference. Fig. 3.14 illustrates the P300 source localization results of auditory stimulation at the peak (312ms). Since the results of

MNE and sLORETA show low spatial resolution, a threshold is set at 20% of the maximum intensity to improve the visualization. One can see that the source localization results of different methods generally agree with each other. The sources from insula, superior temporal, temporo-parietal junction and parietal cortex are detected, which agree with previous literature [LPF99, MJS04, Lin05]. The results of MNE and sLORETA are spread out with many spurious sources, and the extent of the sources is difficult to be identified. L1 method generates an over-focused result that only a few voxels are active in each source area. TV-ℓ_1 produces a result with clearer extent, however, the current density is piecewise constant in each source subregion. In contrast, our method provides a smooth result that reflects the intensity variation of the sources in space. Fig. 3.13 shows the source localization results of visual stimulation at 438ms, in which the sources in posterior temporal, parietal and mesial frontal cortices are found, which generally agrees with previous literature [LPF99, Lin05]. One can see that the image resolution for MNE and sLORETA is very low, especially for sLORETA. L1 method only pinpoints a few active voxels and TV-ℓ_1 provides an almost uniform current density in each source region. Compared to other methods, the proposed method demonstrates the capability of producing brain images with better smoothness and higher spatial resolution.

3.4.4 Discussion

In this study, we develop a novel EEG source imaging method aiming to accurately reconstruct the location, extent, and magnitude variation of the current density distribution. The contributions of this work are threefold: (1) a voxel-based total generalized variation (vTGV) regularization is defined, which incorporates the information of higher-order derivatives and therefore is able to enhance smoothness of the reconstructed brain image as well as reduce the staircasing artifacts; (2) a new ℓ_{1-2} regularization is introduced to the EEG source imaging field for the first time, which is able to reconstruct a sparser source than the widely used ℓ_1 regularization; and (3) an efficient algorithm is derived to solve the proposed model based on DCA and ADMM. The reconstructed brain image by the proposed method shows not only high location accuracy, but also high focalization degree.

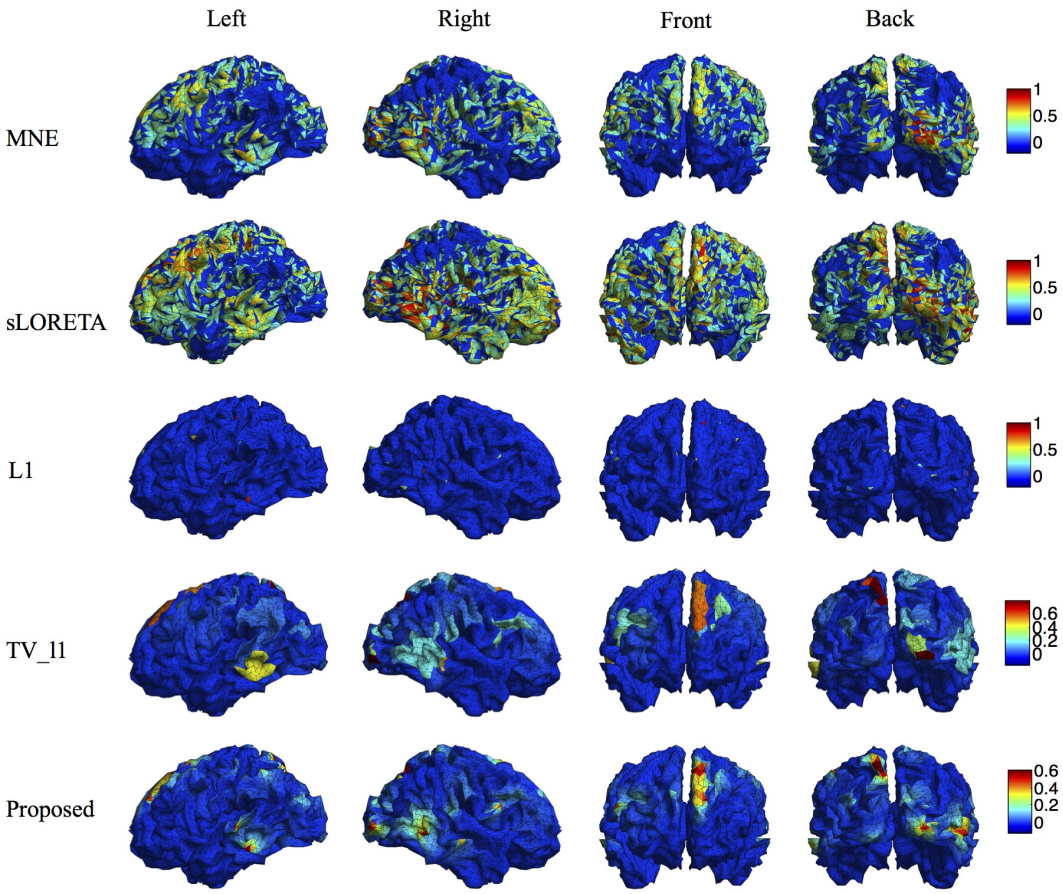

Figure 3.13: Localization results of visual P300 sources with different methods.

Due to the ill-posedness of EEG inverse problem, the source image reconstruction relies on the modeling of the characteristics of underlying sources. MNE and sLORETA do not model the spatial relation between adjacent dipoles; thus the reconstructed current density distribution is not smooth and many spurious sources are generated. Minimum ℓ_1-norm methods, such as MCE, assume the source to be highly focalized thus is not suitable for spatially extended sources. Total variation (TV) based methods assume the intensity of the source to be uniformly distributed in space, and hence fail to reflect the intensity variation of the sources. This effect becomes more obvious when the regularization parameter increases, resulting in even more flat intensity distribution [Gra09]. By contrast, the proposed method s-SMOOTH assumes the intensity of the adjacent dipoles to be piecewise polynomial, resulting in a brain image which is very smooth that recovers the magnitude variation within a source precisely (Fig. 3.7). The performance of the proposed method is evaluated under

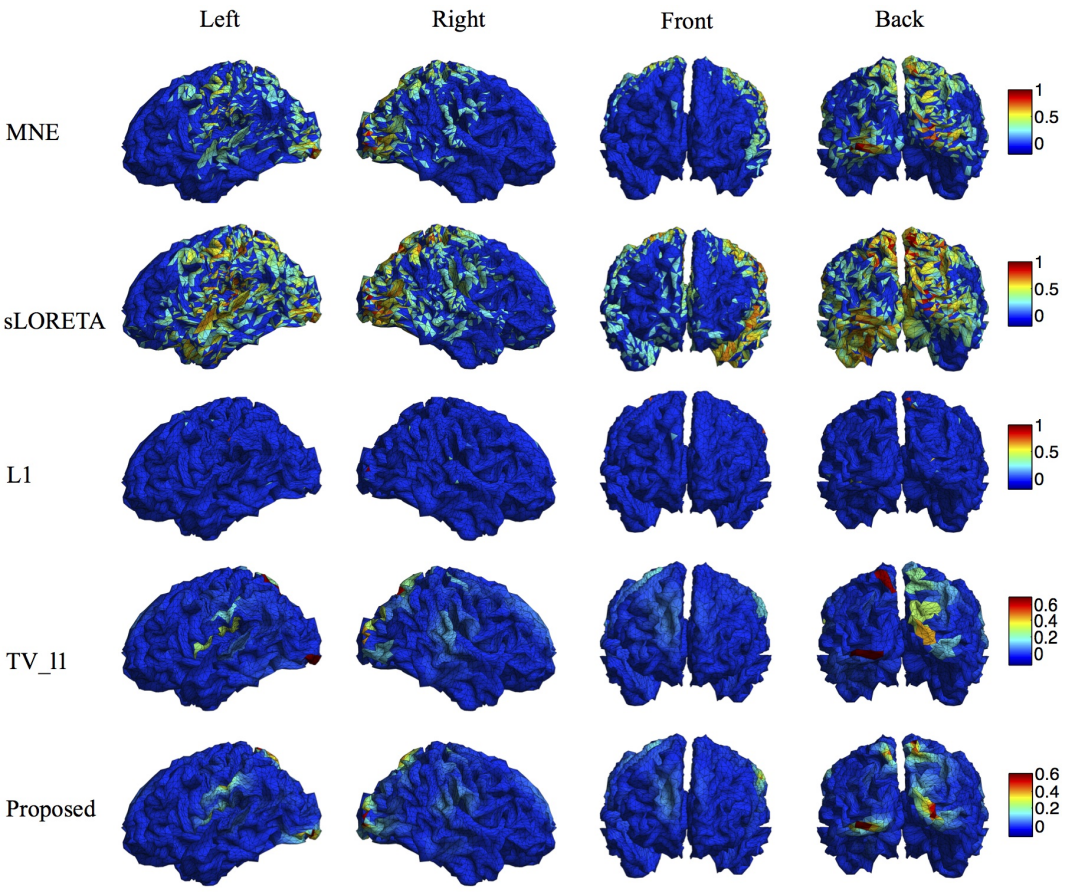

Figure 3.14: Localization results of auditory P300 sources with different methods.

various noise levels, source sizes, source configurations and locations. The simulation results show that the source reconstruction result of s-SMOOTH is robust under different conditions. Quantitative results show that the performance of s-SMOOTH improves as the noise level decreases (Fig. 3.8(B), Fig. 3.9(B)), source size increases (Fig. 3.10(B)), and current density distribution gets far from a constant function (Fig. 3.11(B)).

The classical TGV assumes that the underlying image is piecewise polynomial (including piecewise constant, linear, quadratic, etc.) and thus imposes sparsity in high-order spatial derivatives. In this work, we extend the TGV framework from Euclidean spaces to irregular surfaces and propose a novel second-order vTGV operator. A large number of simulation experiments with Gaussian-shaped sources show that it provides better results than the state-of-the-art methods. It is sufficient to use second order considering the computational cost and performance improvement. Note that the second-order TGV is mathematically different

from the Laplacian operator [BKP10] used in previous methods, such as LORETA, FVR, and CENT^L. Laplacian operator has been widely used in EEG brain imaging [PML94, HNZ08, CNH10] due to its simple form. However, it only considers the unmixed second partial derivatives and does not involve the mixed partial derivatives. It assigns high weight to the central dipole and low weights to its neighbors, resulting in a very high peak in the center of the reconstructed source. In contrast, the proposed vTGV operator takes both unmixed and mixed partial derivatives into account and is able to recover fine details of brain images. Fig. 3.15 compares the reconstructed brain image using a Laplacian operator and the proposed vTGV operator. One can see that the vTGV operator reconstructs the intensity variation of the sources more precisely. With the Laplacian operator, the reconstructed sources show a high peak in the center and the intensity decays very fast from the center ("over-smoothing" effect). Note that in this study, we treat each triangle as voxel, so each voxel has three neighbors. Accordingly, the weighting assigned to the central voxel by Laplacian operator is 1 and is -1/3 for its neighbors. In the case that each vertex is treated as voxel, this over-smoothing effect will become even more severe, since each vertex usually has 6 neighbors thus the weighing assigned to the neighbors will be only -1/6. From the quantitative results in the right panel of Fig. 3.15, one can see that the vTGV operator is advantageous in both total reconstruction accuracy and localization accuracy. The focalization degree results are very close for both operators.

The ℓ_1-norm regularization has been used in EEG source imaging to improve the focalization of the source for a long time [MO95, UHS99, HDS06, DH08]. In this work, we use the ℓ_{1-2} regularization instead of the ℓ_1-norm regularization to enhance sparsity of the image. The ℓ_{1-2} regularization is a very recently proposed regularization technique which refines the ℓ_1 regularization by taking the difference between the ℓ_1 and ℓ_2 norms. In this work, we set the parameter $\beta \in [0, 1]$. When β is equal to 0, ℓ_{1-2} regularization becomes the ℓ_1-norm regularization. We show that the reconstruction accuracy is improved as β increases, and it achieves the highest accuracy when $\beta = 1$ (Fig. 3.5(B)). Therefore, we set the β to 1 in our experiments. Fig. 3.5(C) shows that with $\beta = 1$, the sparsity of the image improves faster than $\beta = 0$, implying that the sparsity of the image is further enhanced using the ℓ_{1-2}

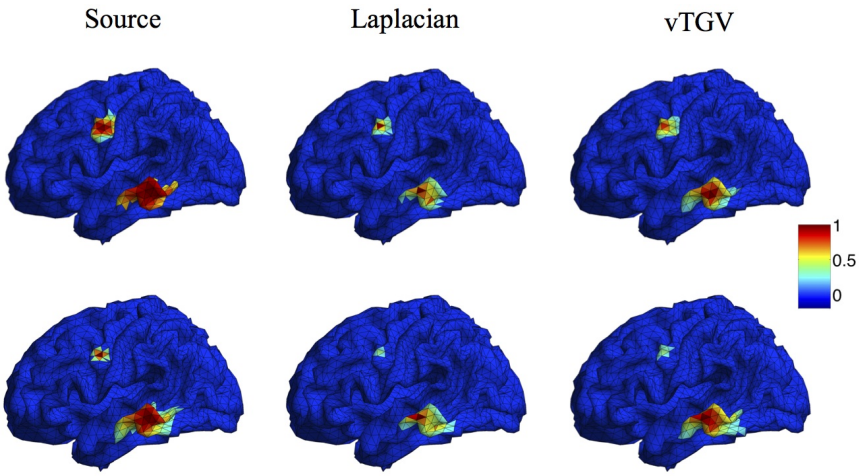

	Laplacian	vTGV
TRE	0.29	0.16
LE(mm)	5.59	3.55
DF(%)	96.92	96.49

	Laplacian	vTGV
TRE	0.25	0.11
LE(mm)	5.59	5.59
DF(%)	99.65	99.34

Figure 3.15: Comparison of Laplacian and vTGV operator. Top: two sources with different configurations. Bottom: two sources with different sizes. The left panel visualizes the source localization results. The vTGV operator provides accurate results with intensity distribution closer to the ground truth. The right panel shows the quantitative results.

regularization compared to ℓ_1 regularization. On the other hand, if sparsity is fixed, ℓ_{1-2} regularization helps to accelerate the convergence of the optimization algorithm.

It is worth noting that the proposed objective function is a very general frame, which includes some related methods, e.g. L1, TV and TV-ℓ_1, as its special cases by choosing proper parameters. For example, by setting the α_2, p and β to be 0, it becomes the TV-ℓ_1 method. By further setting the α_3 to be 0, it becomes the TV method. On the other hand, if choosing α_1, α_2 and β to be 0, it becomes the L1 method. In addition, some relevant methods that combine two regularization terms [HNZ08, CNH10, SLW16] usually describe the data fidelity by using an inequality constraint. Instead, we integrate this term into our objective function. This enables us to apply efficient optimization methods such as ADMM to derive a fast and robust algorithm. Compared to the optimization algorithms used in these methods [HNZ08, CNH10, SLW16], the proposed algorithm in this work is more efficient and robust, and it is also able to tackle large-scale problems. Further, with this type of problem formation, it is possible to adopt some computing techniques [PXY16] to further accelerate the algorithm, which will be the future work.

For parameter selection, we provide some typical parameter values that work well in our experiment. Table 3.1 lists some values for α_1 used in our experiments. For α_2, we simply set it to be equal to α_1. Note that it might provide a better result if α_2 is further tuned. For α_3, the parameter associated with the sparsity term, we show that the source reconstruction results are not sensitive to the choice of α_3 as long as it is within the range $0.1 \sim 0.5\alpha_1$. Specifically, we suggest to use $\alpha_3 = 0.3\alpha_1$. Notice that in this study, we focus on spatially extended sources rather than point sources; therefore, we assign relatively small weighting to the sparsity term. In the case that the underlying source is point source, larger weights can be assigned to the sparsity term (e.g. $\alpha_3 = 100\alpha_1$) so as to make the reconstructed source highly focalized.

3.4.5 Conclusion

In this study, we propose a novel EEG inverse method Sparsity and SMOOthness enhanced brain TomograpHy (s-SMOOTH), which combines the vTGV and the ℓ_{1-2} regularizations to improve reconstruction accuracy for EEG source imaging. Considering the complicated geometries of the cortex surface, we define a vTGV regularization on a triangular mesh expressed as an infimal convolution form. The vTGV regularization enhances the high-order smoothness and thus is able to improve localization accuracy, while the ℓ_{1-2} regularization enhances the sparsity of the brain images. A series of simulation experiments with Gaussian-shaped sources show that the proposed s-SMOOTH is able to accurately estimate the location, extent, and magnitude variation of the current density distribution. It also consistently provides better performance than other competitive methods in terms of quantitative criteria such as total reconstruction accuracy, localization accuracy, and degree of focalization. Although this study focuses on discussing EEG source imaging, the proposed method is equivalently applicable to MEG source imaging.

CHAPTER 4

Acceleration of EEG Brain Image Reconstruction

In Chapter 3, we present a novel EEG brain image method s-SMOOTH, which incorporates two advanced regularization techniques to provide brain images with high reconstruction accuracy. An efficient algorithm using ADMM is derived to solve the problem, however, its computational cost is still relatively high due to these complicated regularization terms. In order to provide real-time brain images, more efficient methods with less computation are desired.

In this chapter, we propose a graph Fractional-Order Total Variation (gFOTV) based method, which provides similar reconstruction accuracy but consumes less computation by using only one regularization term. As discussed in the previous chapter, imposing sparsity on the first derivative provides sources with high focalization degree, but the intensity of the reconstructed sources is almost uniform that leads to low localization accuracy. On the other hand, imposing sparsity on the second derivative produces smooth brain images, which improves the localization accuracy but the reconstructed sources become less focalized. To solve this problem, the s-SMOOTH method incorporates two regularization terms: voxel-based total generalized variation (vTGV) regularization and the ℓ_{1-2} regularization. The vTGV regularization imposes sparsity on the second derivative, which enhances the smoothness of the brain image, and the ℓ_{1-2} regularization imposes sparsity on the current density itself to enhance the sparsity of the image. The combination of these two regularizations result in a brain image that is both locally smooth and globally sparse. In contrast, the gFOTV method only employs one regularization term to achieve similar performance. It provides the freedom to choose the smoothness order by imposing sparsity on α-order derivatives ($\alpha > 0$). We demonstrate that choosing a order $\alpha = 1.6$ provides an accurate result that is

smoother than $\alpha = 1$ and more focal than $\alpha = 2$. The performance of gFOTV and various state-of-the-art methods is compared using a large amount of simulations both qualitatively and quantitatively. The results demonstrate the superior performance of gFOTV not only in spatial resolution but also in localization accuracy and total reconstruction accuracy. With only one regularization term, the computational cost of gFOTV method is reduced to three times less than that of the s-SMOOTH method.

To further speed up the algorithm, we develop a parallel algorithm by applying the Chambolle-Pock and ARock algorithms along with diagonal preconditioning. A variety of experiments show that the proposed algorithms have more rapid convergence than the state-of-the-art methods and have the potential to achieve the real-time temporal resolution.

4.1 Sparsity on Fractional-Order Derivative: Fractional-Order Total Variation (FOTV)

Fractional-order TV has been proposed recently in image processing to enhance smoothness with relatively low computational cost [RHZ13, CSZ13, BF07]. We focus on the anisotropic version in which the objective function of the derived minimization problem is separable. Recall that the anisotropic fractional-order TV in a 2D rectangular mesh is defined as follows:

$$TV_\alpha(u) = \|\nabla^\alpha u\|_1 = \sum_{i,j=1}^{M} \big(|(D_x^\alpha u)_{i,j}| + |(D_y^\alpha u)_{i,j}|\big),$$

where $\alpha \in (1, 2)$. Here the fractional derivative is based on the Grüwald-Letnikov derivative definition [OS74]

$$(D_x^\alpha u)_{i,j} = \sum_{k=0}^{K} w_\alpha(k) u(i-k, j),\ (D_y^\alpha u)_{i,j} = \sum_{k=0}^{K} w_\alpha(k) u(i, j-k),$$

where the coefficients are

$$w_\alpha(k) = (-1)^k \frac{\Gamma(\alpha+1)}{k!\Gamma(\alpha-k+1)}.$$

It is easy to see that $w_\alpha(0) = 1$ and $w_\alpha(1) = -\alpha$. Moreover, if $\alpha = 1$, then TV_α is the traditional TV. If $\alpha = 2$, D_x^α / D_y^α approximates the second partial derivative of u along the

x/y-direction. Although the above definition is also valid for $\alpha \in (0,1) \cup (2,\infty)$, it has experimentally shown that $\alpha \in (1,2)$ achieves the best performance in applications [CSZ13].

4.2 Graph Fractional-Order Total Variation (gFOTV)

Since the cortex surface is an irregular 3D surface consisting of gyrus and sulcus, we define a graph α-order TV with $\alpha \in [1,2]$ tailored to such surface. After discretizing the cortex surface, we create a graph whose nodes correspond to the centroids of all triangles. For a specific node v_i, let $d(v_i, v_j)$ be the number of nodes on the shortest path connecting the nodes v_i and v_j, which is in or close to a geodesic of the underlying surface passing through v_i and v_j. Given a path $p = (v_{i=m_0}, v_{m_1}, \ldots, v_{m_K})$ where the shortest distance between the nodes v_{m_0} and v_{m_j} is j nodes, the fractional-order derivative along the path p is defined as

$$(D_p^\alpha u)_i := D_p^\alpha u(v_i) = \sum_{v \in p} w_\alpha(d(v_i, v)) u(v) = \sum_{j=0}^{K} w_\alpha(j) u(v_{m_j}).$$

Then the discretized fractional-order TV of u is defined as follows:

$$TV_\alpha(u) = \|D_\alpha u\|_1 = \sum_{i=1}^{M} \sum_{p \in \mathcal{P}(i;K)} |(D_p^\alpha u)_i|,$$

where $\mathcal{P}(i;K)$ is the set of all paths starting from the ith node with length of K nodes. The shortest path between each node pair can be calculated by the breadth-first search (BFS) algorithm. For a specific node v_i, the nodes at level k, i.e., the nodes have shortest distance k from v_i, are assigned the weight $w_\alpha(k)$. In particular, if $\alpha = 1$, then D_α is exactly the finite difference operator used in the TV-based methods. If $\alpha = 2$, then $w_\alpha(k) = 0$ for $k > 2$ which implies that all nodes at level more than two are assigned zero weight. If $\alpha \in (1,2)$, then the weights $w_\alpha(k)$ will gradually decay as k goes to infinity. As the value of α increases from 1 to 2, the decay rate of weights $w_\alpha(k)$ becomes larger. Note that K specifies the maximal level of nodes to be used. Due to the sparse structure of the underlying u, it is sufficient to choose $K \leq 4$ levels of neighboring nodes to achieve the desired accuracy in our experiments.

4.3 gFOTV: Graph Fractional-Order Total Variation EEG Source Reconstruction

4.3.1 Formulation and Algorithm

After defining FOTV on triangular mesh of cortex surface, we propose the following fractional-order TV regularized EEG source reconstruction model to improve high order smoothness of the brain image

$$\min_{u} \left\{ \frac{1}{2} \|Au - b\|_2^2 + \lambda TV_\alpha(u) \right\}. \tag{4.1}$$

where $\lambda > 0$ is regularization parameter, which controls the tradeoff between the data fidelity term and the sparsity term.

By change of variables, the above problem can be converted to a linear equality constrained minimization problem

$$\min_{u,v} \left\{ \frac{1}{2} \|Au - b\|_2^2 + \lambda \|v\|_1 \right\}$$
$$\text{subject to } D_\alpha u = v.$$

Then the ADMM yields the following algorithm

$$\begin{cases} v = \text{shrink}(D_\alpha u + \tilde{v}, \lambda/\rho) \\ u = \underset{u}{\text{argmin}} \left\{ \frac{1}{2} \|Au - b\|_2^2 + \frac{\rho}{2} \|D_\alpha u - v + \tilde{v}\|_2^2 \right\} \\ \quad = (A^T A + \rho D_\alpha^T D_\alpha)^{-1} \big(A^T b + \rho D_\alpha^T (v - \tilde{v}) \big) \\ \tilde{v} \leftarrow \tilde{v} + \gamma (D_\alpha u - v) \end{cases} \tag{4.2}$$

Here the parameters $\rho > 0$, $\gamma \in (0, (\sqrt{5}+1)/2)$ and the shrinkage operator is defined componentwise as $\text{shrink}(u, \mu)_i = \text{sign}(u_i) \max\{|u_i| - \mu, 0\}$.

4.3.2 Experiments and Results

4.3.2.1 Experimental Protocol

In our simulation, Gaussian patches are used to simulate sources in the brain. To represent sources at different locations, we randomly select three sources located at different lobes of the cortex surface. In addition, to evaluate the performance of the proposed methods for different source sizes, we simulate sources containing 50, 100, 150, 200, 250 voxels, corresponding to 1.0cm, 1.4cm, 1.7cm, 1.9cm, 2.1cm in radius, respectively. After sources are generated, random independent and identically distributed (i.i.d.) Gaussian noise is added to each voxel as background neural noise. Additionally, electrode and electronic noise are added to each channel. For the signal-to-noise ratio (SNR), it is set to be 10dB by default. The number of electrode used is 346, and the number of voxels in the source model is 10240. Finally, the signal is normalized to between $10\mu V$ to $100\mu V$, which is a typical range of amplitude for an adult EEG signal [AGA04]. To reduce round-off errors, both the lead field matrix A and the electrical potential b are scaled by 10^5.

4.3.2.2 Parameter Selection

In the operator D_α, the parameter α specifies the order of the spatial derivative domain where we want to impose sparsity constraint on. As α becomes larger, we impose sparsity of higher order derivatives, and therefore the reconstructed sources become smoother and decay faster. When $\alpha = 1$, the source decay speed is the slowest, which is the case of TV that the current density is piecewise constant. By our experience, it works well when $\alpha = 2$. By choosing α to be a fraction between 1 and 2, all level nodes will be assigned a non-zero weight, which enhances reconstruction smoothness. Specifically, $\alpha = 1.6$ is appropriate for all our experiments. In addition, the spatial resolution will be higher than that of $\alpha = 2$. In the proposed Algorithm Eq. (4.4), the regularization parameter λ controls the balance between the data fidelity term and the sparsity term. When the source size becomes larger, λ should be tuned to be a little larger. As the noise level becomes higher, λ needs to be a little smaller. According to our experience, it works pretty well by simply choosing λ around

1. The parameter ρ affects the convergence speed of Algorithm Eq. (4.4), and is set as 10λ by default. Finally, the parameter γ is fixed as 1.

4.3.2.3 Simulation Results

First, we evaluate the performance of the proposed method using $\alpha = 2$ and $\alpha = 1.6$, and compare with several state-of-the-art methods: sLORETA, ℓ_1-norm based and TV-based methods. Fig. 4.4 shows the reconstruction results of three sources at different locations of the cortex surface. One can see that the spatial resolution of sLORETA is very low, since it is based on the Tikhonov regularization using ℓ_2-norm. The ℓ_1-norm based method MCE greatly improves the spatial resolution because it imposes sparsity of the source in itself, but it yields over-focused reconstructed sources and fails to identify the spatial extent of the sources. The TV-based method shows good performance in identifying the spatial extent and preserving edges. However, it does not recover the varying intensity of the source, because of the assumption that the source intensity is piecewise constant. In contrast, the proposed method generates the reconstructed images closest to the ground truth. It not only provides high spatial resolution, but also successfully reconstructs the intensity variation and the spatial extent of the sources. It is worth noting that $\alpha = 1.6$ is able to further enhance the spatial resolution compared to $\alpha = 2$.

We further evaluate the proposed method quantitatively by using various quantitative criteria. To show the robustness and consistency, we conduct a large number of simulation tests with different source sizes, and average results of 50 realizations with different noise configurations, illustrated in Fig.4.5. In the TRE curve, one can see that the proposed method provides the smallest total reconstruction error. Notice that the TV-based method also shows a relatively small total reconstruction error compared to other methods. In the LE curve, our proposed method shows the smallest localization error, since it makes the brain image smoother by imposing sparsity in higher order derivative instead of the first order derivative. As is well known that sLORETA can provide high localization accuracy, sLORETA also shows small localization error. TV-based method, however, produces rela-

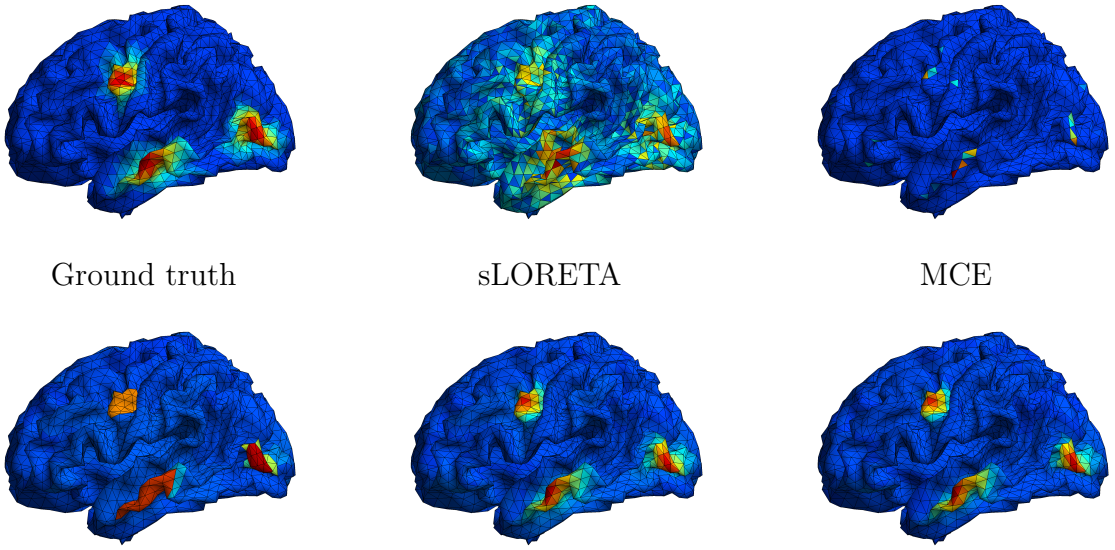

Figure 4.1: Source localization results of various methods on synthetic data with three sources. The color scale gradation goes from blue being the minimum to red being the maximum.

tively large localization error, which is because the reconstructed sources are constant in each subregion therefore it has difficulty pinpointing the peak of the source accurately. Finally, the DF curve shows that all of the methods with sparsity constraints show high focalization degree. It is interesting to notice that for gFOTV-based methods, $\alpha = 1.6$ further enhances the spatial resolution. Compared to other methods, the spatial resolution of sLORETA is the lowest, as indicated by its name "standardized low resolution brain electromagnetic tomography". To sum up, our proposed method demonstrates superior performance from all the criteria including total reconstruction accuracy, localization accuracy and focalization degree.

4.3.2.4 Comparison of gFOTV with s-SMOOTH

To compare the performance of gFOTV with s-SMOOTH, we simulate three spatially extended sources on the cortex surface. Fig. 4.3 shows the brain image reconstruction results of TV, s-SMOOTH, and gFOTV methods when $\alpha = 1.6$. The TV method fails to reflect

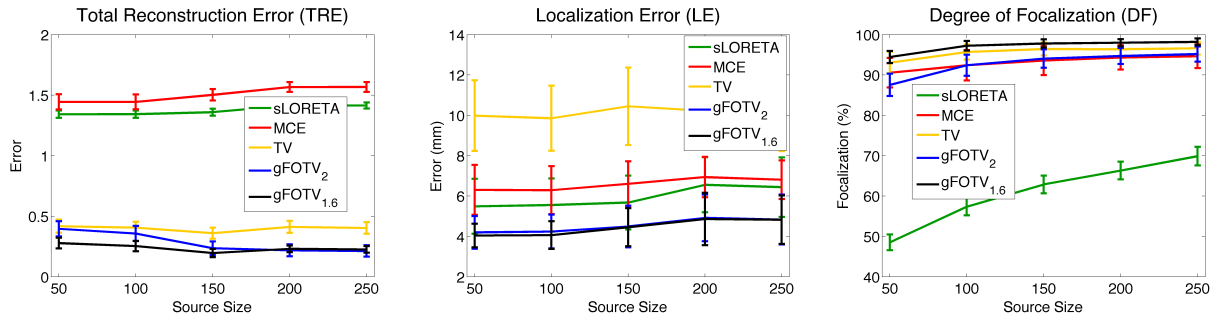

Figure 4.2: Quantitative comparisons of various methods with different source sizes (average of 50 realizations of different noise configurations, where the error bar shows the sample standard deviation).

the varying intensity of the sources, while both s-SMOOTH and gFOTV methods are able to reconstruct the intensity variation. Furthermore, the gFOTV method achieves a better result that is closer to the ground truth than the s-SMOOTH method. This can also be seen from the quantitative results where the TRE for s-SMOOTH is 0.22 while that for gFOTV is only 0.19, indicating that the gFOTV provides higher reconstruction accuracy compared to s-SMOOTH method. More interestingly, the gFOTV method only consumes 1/3 of the computation compared to the s-SMOOTH, since it only uses one regularization term. In summary, the gFOTV method demonstrates potential to provide similar or higher reconstruction accuracy but consume less computation cost than the s-SMOOTH method.

4.3.3 Conclusion

We have proposed an efficient and accurate EEG source reconstruction method by defining a novel graph fractional-order total variation (gFOTV) adapted for a triangular mesh of the cortical surface. This method imposes sparsity in α-order spatial derivatives with $\alpha \in [1, 2]$, which includes the TV-based methods as a special case when $\alpha = 1$. By tuning the parameter α, the proposed method provides the freedom to choose a more elegant order of smoothness for the underlying brain image. Therefore, it not only provides high spatial resolution, but also recovers the current density variation and localizes the source peaks with high accuracy. In addition, the proposed algorithm is parameter friendly in the sense that the parameter

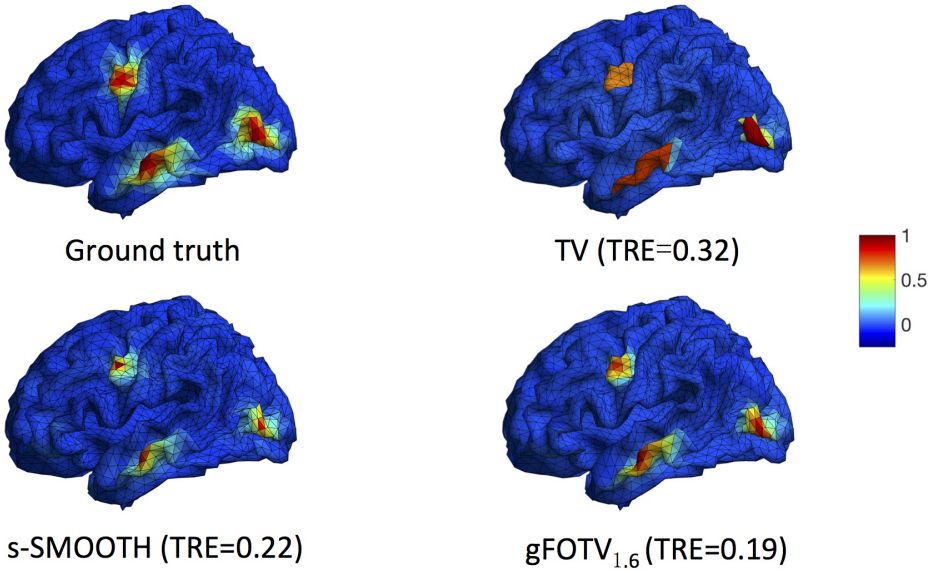

Figure 4.3: Comparison of gFOTV with s-SMOOTH.

selection is not sensitive to source size and noise level. A variety of simulation experiments demonstrate that the proposed method consistently outperforms the state-of-the-art methods both qualitatively and quantitatively.

4.4 Parallel Computation to Accelerate the Algorithm

The gFOTV is able to save the computational cost by only involving one regularization term. However, since each of its iterations solves a least squares subproblem, the computation intensity of gFOTV grows very quickly as the number of voxels increases. Inspired by the numerical performance of the asynchronous coordinate updating scheme [PWX16], we exploit the coordinate-friendly structure of the gFOTV operator and develop a very fast algorithm to solve it. It is important to note that the proposed algorithm can be easily extended toward other regularization models that involve the composition of the ℓ_1-norm and a coordinate-friendly operator, such as those in the sparse source imaging (SSI) [DH08] and the spatial Laplacian in [CNH10].

4.4.1 Fast Numerical Algorithm

We consider the following variational model to reconstruct the current density distribution on the cortical surface

$$\min_u \frac{1}{2} \|Au - b\|_2^2 + \lambda \|D_\alpha u\|_1 , \tag{4.3}$$

where $\lambda > 0$ is a tuning parameter used to balance the first data fidelity term and the second regularization term. Here $\|\cdot\|_2$ is the Euclidean norm and $\|\mathbf{x}\|_1$ returns the sum of absolute values of all components in the vector $\mathbf{x}$. Note that the proposed algorithms can be easily extended when we replace D_α in Eq. (4.3) by another sparsifying matrix. For example, if D_α is replaced by the identity matrix, then Eq. (4.3) becomes the ℓ_1-norm regularized model [UHS99, DH08].

In our previous gFOTV work [LQO16], we applied the alternating direction methods of multipliers (ADMM) to derive an algorithm, where one subproblem involves solving $Mx = b$ for an $N \times N$ matrix M. It is time-consuming even though we used the Cholesky factorization; moreover, the computation time will increase superlinearly when the number of voxels N increases. Motivated by the desire to design a scalable algorithm, we resort to the Chambolle-Pock algorithm [CP11]. The Chambolle-Pock algorithm is one of the first primal-dual algorithms which solves the problem $\min_x \ f(x) + g(Ax)$ without inverting any matrices.

By defining

$$B = \begin{pmatrix} A \\ D_\alpha \end{pmatrix},\ f(p,q) = \frac{1}{2}\|p - b\|_2^2 + \lambda\|q\|_1 \text{for } \begin{pmatrix} p \\ q \end{pmatrix} \in \mathbb{R}^{M+L},$$

Problem Eq. (4.3) can be rewritten as $\min_u \ f(Bu)$. Then we can apply the Chambolle-Pock algorithm with diagonal preconditioning [PC11] to solve it. By introducing two dual variables $s \in \mathbb{R}^L, t \in \mathbb{R}^M$, we obtain the following algorithm

$$\begin{cases} u^{k+1} = u^k - \Sigma(D_\alpha^T s^k + A^T t^k) \\ s^{k+1} = \text{Proj}_{\|\cdot\|_\infty \le \lambda}(s^k + \Gamma_1 D_\alpha(u^k - 2\Sigma(D_\alpha^T s^k + A^T t^k))) \\ t^{k+1} = (I + \Gamma_2)^{-1}(t^k - \Gamma_2 b + \Gamma_2 A^T(2u^{k+1} - u^k)). \end{cases} \tag{4.4}$$

Here $\Sigma, \Gamma_1, \Gamma_2$ are diagonal matrices controlling the step sizes, which are defined by

$$\begin{cases} \Sigma_{ii} = (\sum_{j=1}^{L} |(D_\alpha)_{ji}| + \sum_{j=1}^{M} |A_{ji}|)^{-1} \\ (\Gamma_1)_{ii} = (\sum_{j=1}^{N} |(D_\alpha)_{ij}|)^{-1} \\ (\Gamma_2)_{ii} = (\sum_{j=1}^{N} |A_{ij}|)^{-1}. \end{cases}$$

The projection of $\mathbf{x} \in \mathbb{R}^L$ is defined componentwise as

$$\left[\mathrm{Proj}_{\|\cdot\|_\infty \leq \lambda}(\mathbf{x})\right]_i = \min(\lambda, \max(-\lambda, x_i)).$$

It has been shown that the above choices make Algorithm Eq. (4.4) converge fast.

By letting $z^k := (u^k, s^k, t^k)^T$, Eq. (4.4) can be rewritten as

$$z^{k+1} = Tz^k.$$

As shown in [PWX16], it is computationally advantageous to update z^k in the (block) coordinate fashion. Specifically, for every iteration, we randomly update one coordinate of z in Eq. (4.4), say $z_i^{k+1} = (Tz^k)_i$, and keep the rest coordinates unchanged, i.e., $z_j^{k+1} = z_j^k$ for $j \neq i$. Furthermore, as shown in [PWX16, Section 4.2], we can plug the u update in Algorithm Eq. (4.4) to the t update, and get a similar yet new algorithm:

$$\begin{cases} u^{k+1} = u^k - \Sigma(D_\alpha^T s^k + A^T t^k) \\ s^{k+1} = \mathrm{Proj}_{\|\cdot\|_\infty \leq \lambda}(s^k + \Gamma_1 D_\alpha(u^k - 2\Sigma(D_\alpha^T s^k + A^T t^k))) \\ t^{k+1} = (I + \Gamma_2)^{-1}(t^k - \Gamma_2 b + \Gamma_2 A^T(u^k - 2\Sigma(D_\alpha^T s^k + A^T t^k))), \end{cases} \tag{4.5}$$

which is more suitable for coordinate update. Algorithm Eq. (4.5) is shown to be *coordinate-friendly*, which means updating one coordinate of z is much cheaper than updating z entirely, and the aggregate cost of updating all coordinates is similar to updating the whole z. Moreover, one of the major advantages of coordinate update is that it allows larger step sizes than its full update counterpart. During the implementation of the coordinate update of Algorithm Eq. (4.5), all the step-size matrices $\Sigma, \Gamma_1, \Gamma_2$ are multiplied by a scaling factor $s \geq 1$, which empirically leads to faster convergence.

Furthermore, on computers and clusters equipped with multiple cores, we are able to perform asynchronous parallel update in Eq. (4.5), as described in [PWX16, Section 4.4] and [PXY16], which greatly speeds up the convergence. On a multi-core system, each core will randomly select one coordinate of z to update, independent of other cores, and all cores update the coordinate in parallel, while reading from and writing to their shared memory. Asynchronous information delay and lockless memory access are allowed. It is shown in [PXY16, PWX16] that if we relax the coordinate update as

$$z_i^{k+1} = (1-\rho)z_i^k + \rho(Tz^k)_i, \quad z_j^{k+1} = z_j^k, \ \forall\, j \neq i, \tag{4.6}$$

with a properly chosen factor $\rho < 1$, then this async-parallel algorithm will yield a solution to Problem Eq. (4.3). We empirically choose $\rho = 0.5$ in all experiments for stable performance. Our numerical experiments show that the above async-parallel version provides a nearly linear speedup to Algorithm Eq. (4.5) as the number of working cores grows.

4.4.2 Experiments and Results

In this section, we demonstrate the performance of the proposed algorithms by testing them on various simulation data sets. In particular, we compare the randomized coordinate update of Algorithm Eq. (4.5) and its multi-core version with the ADMM-based algorithm [LQO16] and the CVX toolbox `http://cvxr.com/cvx/`. The toolbox has been used in the state-of-the-art EEG methods [CNH10, SLW16]. We apply the fractional-order TV regularized model with $\alpha = 1.6$, which consistently yields superior performance compared to other related models in terms of accuracy [LQO16]. It is worth noting that as the number of voxels increases, the quality of brain images reconstructed from this model can be further enhanced.

4.4.2.1 Simulation Protocol

Our simulation uses the same sources as those in [LQO16], which we describe as follows. First, a center is seeded and then its neighbors are gradually recruited to form a patch. The current density is the strongest in the center, and then gradually decays as it goes far from

the center following the shape of a Gaussian distribution. To represent sources at different locations, we randomly select three sources located in different lobes of the cortex surface. To simulate the noise, we impose random independent and identically distributed (i.i.d.) Gaussian noise to each voxel and then add Gaussian noise at a signal-to-noise ratio (SNR) of 20dB to each channel. The simulated measurements are normalized to fall between 10 μV to 100 μV, as suggested in [AGA04]. Experimental results show that the computation time only relies on the number of voxels, the number of electrodes and the regularization parameter λ, rather than the configuration of noise and source. Here, we choose the number of electrodes as 68, 103 and 346, and the number of voxels as 10240, 16384 and 40960.

4.4.2.2 Computing Platform

All numerical experiments are performed in a machine with an Intel® Xeon® CPU E5-2650 v4 @ 2.2GHz and 64GB RAM in double precision. The CPU has 12 physical cores and each core has 2 logical processors. The ADMM and CVX are called in Matlab 2016a running on Windows 10. The async-parallel coordinate update algorithm is written in C++ based on the toolbox [EPY16], and runs on Ubuntu 16.04LTS. We compare only the computing time of the three algorithms. The core optimization algorithm of CVX is written in C and called in Matlab through MEX; the ADMM subproblems are solved using basic linear algebra operations in Matlab, which are highly optimized. Therefore the comparison is considered fair despite the difference of platforms.

4.4.2.3 Performance Comparison

To make a fair comparison, we let each algorithm run until it achieves the same objective function value, which implies the same accuracy and focalization degree. The scaling factor s for the step size matrices in Eq. (4.6) is tuned between 5 and 11 to achieve the best performance. In addition, we fix the regularization parameter $\lambda = 20$ for all tests, as it works well consistently. Let p be the number of threads in our algorithm.

Fig. 4.4 shows all the brain images reconstructed from various data sets by randomized

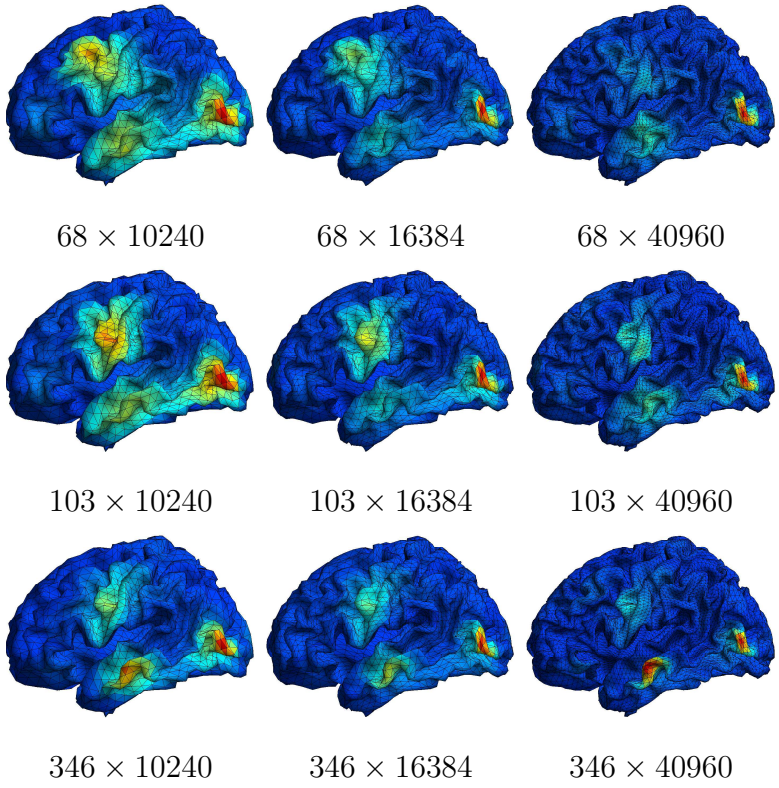

Figure 4.4: Reconstructed brain images for various data sets (No. of electrodes × No. of voxels).

coordinate update of Algorithm Eq. (4.6) running one thread. As the triangular mesh gets finer, the reconstructed sources become more focused. The increase of electrodes also helps shrink the extent of sources and thereby localize sources more accurately. In Columns 3-6 of Table 4.1, we compare the computation times of single-threaded CVX, ADMM and coordinate update of Eq. (4.6) running one thread and 16 threads. Here, we manually change the precision in CVX to achieve the same accuracy. In ADMM, the algorithm terminates when it reaches either 1000 iterations or the tolerance of 10^{-3} for the relative error between two consecutive results. In our method, we tune the scaling factor s and the number of epoches for each data set, and then fix them for both single-threaded and multi-threaded versions of Algorithm Eq. (4.6). One can see that for large-scale data sets, e.g., the case with 346 electrodes and 40960 voxels, coordinate update algorithm Eq. (4.6) shows superior performance over ADMM and CVX in terms of computation time.

m	n	CVX	ADMM	$p = 1$	$p = 16$
68	10240	52.78	67.36	40.30	4.90
68	16384	95.00	237.80	74.46	8.46
68	40960	311.71	2015.79	242.42	25.45
103	10240	62.37	64.21	33.00	3.84
103	16384	108.16	175.31	56.19	6.35
103	40960	393.23	1639.51	194.48	19.77
346	10240	370.63	51.02	45.14	5.21
346	16384	476.16	135.12	66.45	7.59
346	40960	2720.28	1200.10	177.15	19.70

Table 4.1: Computation time in seconds. Columns 3 to 6 list the computation times of single-threaded CVX, ADMM and the proposed algorithm Eq. (4.6) with one thread and 16 threads, respectively.

Furthermore, to study the speedup behavior of Algorithm Eq. (4.6), we use various numbers of threads $p = 1, 2, 4, 8, 16$ and fix the number of epoches as 5000 and the scaling factor $s = 6$. We define the speedup ratio by

$$\frac{\text{running time using 1 thread}}{\text{running time using } p \text{ threads}},$$

which measures the reduction of running time due to the growth of threads. In Fig 4.5, we plot the speedup ratio against the number of threads. One can see that the async-parallel coordinate update algorithm achieves an (almost) linear speedup as the number of threads grows. The above comparisons show that multi-threading significantly shortens the computation time: for the 346×40960 test, it is reduced from over twenty minutes (ADMM or CVX) to less than twenty seconds (see Table 4.1).

4.4.3 Conclusion

We propose a fast and high-resolution EEG source imaging method, which significantly accelerates the numerical solutions of TV and gFOTV regularized EEG reconstruction methods.

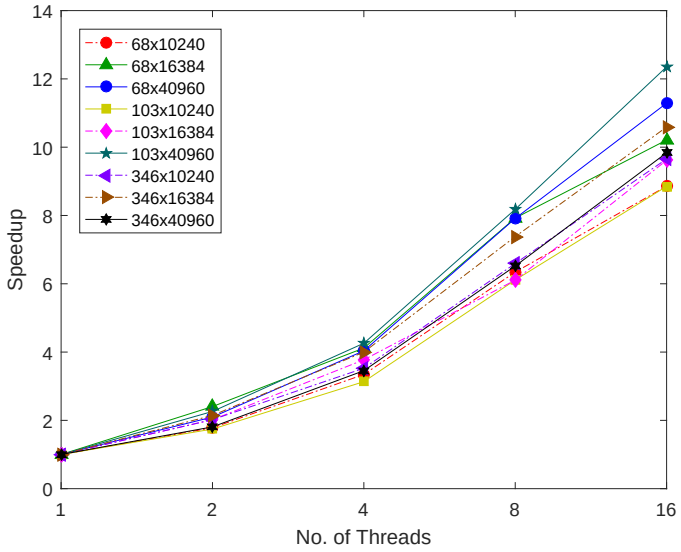

Figure 4.5: Multi-threading speedup of computation.

Specifically, by utilizing the coordinate friendly structure of the gradient and the fractional-order gradient operators, we derive the proposed algorithm by applying the primal-dual method and diagonal preconditioning technique. Numerical experiments show that the proposed method running multiple threads on a multi-core system exhibits superior performance in terms of both computation time and solution accuracy over the state-of-the-art methods. The proposed approach can be generalized to accelerate other regularized models involving the ℓ_1-norm. It also has a great potential to achieve real-time temporal resolution, which can potentially bring tremendous convenience and broad influence to clinical applications.

CHAPTER 5

Focalized Multi-Electrode Stimulation with Optimization Techniques

In the previous chapters, we have developed several EEG-based brain imaging algorithms that are able to produce images with high spatial and temporal resolution. In this chapter, we will discuss focal and precise electrical stimulation for neural disorder treatment. Specifically, we are interested in noninvasive neuromodulation that does not requires surgery, such as transcranial current stimulation (tCS) and transcutaneous spinal cord stimulation (tSCS). We will also discuss how to integrate together of both neural imaging and neural stimulation by applying neural imaging to guide the neural stimulation.

It is well known that the key challenges for noninvasive stimulation lie in the ability to provide high spatial and temporal resolution, with a high degree of focal accuracy, while using the correct intensity and directionality using external current injection through an electrode on the skin. The conventional two-electrode system inherently lacks this capability. However, a multi-electrode systems can meet these requirements, based on their use of sophisticated mathematical models and algorithms, and carefully designed safety features. As a result, a multi-electrode system is considered herein as a viable mechanism to achieve focal and precise stimulation.

In this chapter, we first introduce the background of tCS and tSCS. To achieve focalized and precise stimulation, we propose a novel optimization method called Stimulation with Optimal Focality and Intensity (SOFI), which is able to optimize both intensity and focality at the target. We also apply the SOFI method to tCS and tSCS, and demonstrate that it is able to stimulate multiple targets as well as avoid certain regions with high focal and

localization accuracy. In addition, we show that it provides better results than the state-of-the-art methods in terms of directional intensity and focality at the target.

5.1 Introduction

5.1.1 Transcranial Current Stimulation (tCS)

The technique of transcranial current stimulation (tCS) is rapidly becoming a non-invasive neuromodulation for the treatment of brain-related disorders. Transcranial direct current stimulation (tDCS) is a type of tCS, which applies a constant weak DC current to the targeted cortex regions, while transcranial alternating current stimulation (tACS) is a variant of tDCS where the current varies in time. tCS has shown great therapeutic potential for modulating neural disorders and brain injuries such as depression [LKH06, NBF09], Parkinson′s disease [BFR06, FBS06], and epilepsy [ARG13]. Studies also show that tCS could be applicable to attention problem, stroke, and other illnesses caused by traumatic brain injury [WCC06, KKP12, SDO14]. However, most of these studies are conducted by using two large patch electrodes at specific anodic or cathodic neuromodulation at the targeted regions. The two electrode montage has the limitation that it cannot stimulate multiple targets at the same time, and we need to change electrode locations frequently to stimulate different targets.

To overcome the limitations of the two electrode montage, the multiple electrode stimulation has been proposed [DDB11, SVS12, RFR14, GDE16, FTL16]. In order to better make use of each electrode, it is desirable to control each electrode independently and design optimal stimulation patterns for each electrode to obtain a focal stimulation at the target as well as avoid activation in certain regions. So far, several optimization methods have been developed for tCS to achieve more accurate stimulation [DDB11, SVS12, DDH13, RFR14, GDE16]. The conventional optimization methods either maximize intensity at the target, which results in very low focal accuracy (e.g. maximum intensity method [DDB11, DDH13, SVS12, GDE16]), or maximize the focal accuracy at the expense of low intensity (e.g. Linear Constrained Minimum Variance (LCMV) [DDB11]). In addition, in

the LCMV method and its variants [DDB11], a hard constraint is enforced to meet the specified intensity and orientation at the target, which may lead to an infeasible solution when the specified intensity is high or the target region is large. In addition, the hard constraint limits the degree of freedom of the problem, which hinders it from obtaining a better solution with higher intensity or focality. To overcome this limitation, we have developed a novel optimization method called Stimulation with Optimal Focality and Intensity (SOFI), which provides a solution with both high intensity and high focal accuracy within the safety constraints. It is able to not only deal with multiple targets, but also avoid activating certain regions. Particularly, for the spatially extended target, the algorithm is able to provide various current intensity distributions (e.g. uniform, smooth, Gaussian) at the target depending on the applications.

Another limitation of conventional optimization methods is that they require the clinician to specify location and intensity at the target, which is usually unknown in most applications. Recently, a method based on the reciprocity principle was proposed [FTL16], which enables the EEG signal to be used as a guide for designing stimulation patterns without specifying the location of the target. However, the stimulation parameters chosen by this method is just empirical, and it is only able to deal with simple situations, such as cases in which a single focal source predominates. It is unable to handle complicated cases, such as multiple targets, spatially extended targets with different orientations in different parts, or containing brain regions to be avoided. In the multiple targets case, it is possible that this method may stimulate the averaged location of these targets. With the expertise in EEG brain imaging area, we propose to use our dynamic EEG brain image methods [LQO16, QWL16] as a guide for electrical brain stimulation. Using our precise EEG source localization [LQO16, QWL16], our method is able to provide the accurate information of the target location, number as well as orientation, so as to enable a precise stimulation. Different from other studies which use fMRI as a guidance [CCM12], our EEG brain imaging system is able to provide much higher temporal resolution in the range of milliseconds rather than seconds. In addition to guide dynamic stimulation of the neural networks, the concurrent EEG brain imaging will also offer real-time feedback of the neuromodulation. Thus, a closed-loop stimulation is

eminently possible.

5.1.2 Transcutaneous Spinal Cord Stimulation (tSCS)

Epidural spinal cord stimulation (eSCS) has been used for restoration of motor functions in spinal cord injury (SCI) [DGP98, MPR07b, HGH11, AEG14], pain management [Cam04, RDD12, Jeo12], and spasticity control [PGD00]. However, it is invasive in that surgery is needed to implant electrodes into the body. As an alternative, the transcutaneous spinal cord stimulation (tSCS) was used to achieve a similar effect as eSCS in a noninvasive way [EGR12]. It has been shown that tSCS is able to elicit the locomotor-like movements in healthy subjects [MPR07a, GGM10, GMP10, GPP11] as well as in spinal cord injury (SCI) subjects [EGR12, HHK13]. tSCS has also been demonstrated to control pain [Cec09] and suppress spasticity [HMT14]. Conventional tSCS uses one or two large electrodes for stimulation, resulting in non-focal current flows in the spinal cord. Due to the large activated area, it is difficult to avoid certain regions that we do not want to activate, e.g. bladder. In addition, the two-electrode montage is not able to target multiple sites simultaneously, which limits its effectiveness. Furthermore, when stimulating different targets, we may need to frequently change the electrode locations, which is very inconvenient especially if we want to stimulate a neural network dynamically.

More recently, multiple electrode arrays consisting of 3*3 [GGM15, GGP15, GER16], 3*7, and 3*8 electrodes [KTD13, KDS14, KHD15] have been adopted for transcutaneous spinal cord stimulation, which make the multisite stimulation possible. Compared to single site stimulation, the multisite stimulation has been demonstrated to induce more effective stepping movements and higher amplitude of EMG activity in healthy subjects [GGM15, GGP15, GER16]. However, the stimulation parameters are currently chosen by experience, and the induced current is still not focused. In addition, certain sensitive regions such as the bladder cannot be avoided. All of these together limit their capability of modulating the neuronal circuits precisely.

To improve the focal accuracy of the stimulation, ring configuration has been widely

used to enhance the focality of the epidural spinal cord stimulation (eSCS) [RDD12] and transcranial current stimulation (tCS) [DDB11, FTL16]. It is featured by an anode (cathode) electrode surrounded by four cathode (anode) electrodes. Generally, it is good at stimulating the radial orientation, but has difficulty in dealing with tangential orientation [FTL16]. Another limitation lies in that when the target is not underneath any electrode, the ring configuration is not able to stimulate the target precisely. In addition, it is not able to avoid certain regions either. A more effective and focal stimulation can be achieved by precisely constructing a spinal cord model and taking advantage of optimization methods. However, to the best of our knowledge, there has not been any work that uses optimization methods to provide optimal stimulation parameters for tSCS. In this dissertation, we propose a novel optimization method SOFI, resulting in focalized and precise spinal cord stimulation.

5.2 Focalized Multi-Electrode Stimulation

5.2.1 Mathematical Formulation

Let's consider a volume conduction model (e.g. head model, or spinal cord model) with different tissues, where each tissue has isotropic conductivity. Assume there are N electrodes on the skin. We use a vector x to represent the injected current at each electrode. Furthermore, we discretize the whole volume into M voxels and use vector e to represent the electrical field at each voxel resulting from the electrical stimulation. Since we further consider the orientation of the electrical field, the vector e has a dimension of $3M * 1$. Under quasi-static conditions, the electrical field e in the voxels and the stimulation parameters x at the electrodes has a linear relationship [GC99, DDB11]:

$$e = Kx. \tag{5.1}$$

Here, the coefficient matrix K is called "lead field matrix", which describes the one to one mapping between each electrode and each voxel. Specifically, the (i, j)-th entry of K denotes the electrical field at the i-th voxel due to an unit current stimulation at the j-th electrode. Therefore, the electrical field in each voxel is a linear superposition of that

due to the stimulation at each electrode. Note that although focusing on electrical field in this study, we can also use K to represent the electrical potential, current (density), or activation function at each voxel resulting from the current stimulation at each electrode. The K matrix can be calculated by constructing a realistic volume conduction model and solving the Maxwell′s equations [GC99] with the boundary element method (BEM) or finite element method (FEM). Note that the lead field matrix K here is different from that in the EEG inverse problem. Here, the current sources are at the electrode side, while in the EEG inverse problem, the current sources are in the brain.

5.2.2 Prior Arts

There are few literatures that aim to improve focal accuracy in transcutaneous spinal cord stimulation. On the other hand, several methods have been developed to design better stimulation parameters in transcranial current stimulation. In this section, we will review two types of state-of-the-art stimulation methods in transcranial current stimulation: optimization methods and reciprocity methods. These two types of methods have not been used in transcutaneous spinal cord stimulation to the best of our knowledge.

5.2.2.1 Optimization Methods

Recently, optimization techniques have been used to obtain optimal stimulation parameters for transcranial current stimulation [DDB11, RFR14, SVS12, GDE16]. It makes use of the whole multi-electrode array to achieve higher degree of focal accuracy and localization accuracy by assigning different weightings to different electrodes. With the optimization framework, it is very easy to incorporate a variety of constraints, such as avoidance area or any safety limits.

Linearly constrained minimum variance (LCMV)

The Linearly constrained minimum variance (LCMV) [DDB11] adopts analogous methodology as that in beamforming problems. It enforces a hard constraint at the target, including intensity and orientation, and minimizes the electrical field in other areas. Let C represent

a subset of the lead field matrix corresponding to the target voxels and e_0 represent the specified intensity and orientation at the target; then the model of LCMV method can be expressed as follows

$$\min_x \ \|Kx\|^2$$
$$\text{subject to } Cx = e_0.$$

The most advantage of LCMV methods is that it optimizes focal accuracy at the target on the premise that the desired intensity and orientation at the target is satisfied. However, the hard constraint at the target greatly limits the degree of freedom, and hinders it from obtaining better solution with higher intensity and focality. Moreover, with this hard constraint, it is possible that it may be unable to obtain a feasible solution, such as in the cases that the specified target intensity is high or the target area is large.

Maximum Intensity

Different from LCMV which optimizes the focality at the target, the maximum intensity method [DDB11, SVS12, GDE16] optimizes the intensity at the target. Specifically, it maximizes the directional intensity in the desired orientation, assuming that the orientation of the E-field also influences the stimulation results. It optimizes the intensity at the expense of focal accuracy.

$$\max_x \ e_0^T C x$$
$$\text{subject to } \sum_{i=1}^{N} |x| \leq 2 * I_{total}.$$

The advantage of this method is that the obtained intensity at the target is the maximum. On the other hand, its drawback is also obvious that the focal accuracy of this method is sacrificed [DDB11], which will be shown later.

5.2.2.2 Reciprocity Principle Based Methods

A critical limitation of the optimization method is that the target location, intensity, and orientation must be specified beforehand, which is unknown in many cases. Recently, transcranial current stimulation methods based on reciprocity principle [FTL16] were proposed as an alternative of optimization methods. Based on the assumption that there is a single focal source, it designs the stimulation parameters to maximize the electrical field along the desired orientation. It uses EEG as a guide and does not need the prior knowledge of the target. Unfortunately, this method is empirical rather than optimal, and it is only able to deal with simple situations, such as cases in which a single focal source predominates. It is unable to handle complicated cases, such as the situation that there are multiple targets, spatially extended targets with different orientations in different parts, or certain avoidance regions.

5.2.3 SOFI: Stimulation with Optimal Focality and Intensity

In this section, we present a novel method Stimulation with Optimal Focality and Intensity (SOFI) to obtain optimal stimulation parameters for noninvasive electrical stimulation, which overcomes the limitations of the aforementioned methods, and is able to provide both high intensity and focality simultaneously at the target.

5.2.3.1 Safety Criteria

First, it is important to guarantee that the stimulation is within safety limits. If using I_{max} to represent the maximum current at each electrode, I_{total} to denote the maximum total current injected to the body, and *ratio* to represent the intensity ratio between the target and avoidance region, our safety criteria are summarized as follows:

$$
\begin{aligned}
&|x_i| \leq I_{max}, i = 1, ..., N \\
&\sum_{i=1}^{N} |x_i| \leq 2 * I_{total} \\
&\sum_{i=1}^{N} x_i = 0 \\
&Intensity_{avoid} \leq \frac{1}{ratio} Intensity_{target}
\end{aligned}
\tag{5.2}
$$

Note that since the total positive current is equal to the total negative current, the sum of the absolute value of the current should be twice the total current injected to the body (the second safety criteria in Eq. (5.2)). Note that the safety limit values I_{max} and I_{total} may vary in different applications.

5.2.3.2 Optimization Model

The key challenges for noninvasive stimulation technologies lie in the capability of providing precise stimulation with both high focal accuracy and intensity in the desired direction. As we can see, the current optimization methods either maximize the intensity at the target by sacrificing the focal accuracy (e.g. maximum intensity method [DDB11, SVS12, GDE16]), or maximize the focal accuracy at the expense of relatively low intensity (e.g. Linear Constrained Minimum Variance (LCMV) [DDB11]). In addition, in the LCMV method and its variants [DDB11], a hard constraint is enforced to meet the specified intensity and orientation at the target, which may lead to an infeasible solution when the specified intensity is high or the target region is large. To overcome these limitations, we have developed a novel optimization method called Stimulation with Optimal Focality and Intensity (SOFI), which does not set any hard constraint and thus it always generates a feasible solution. Unlike previous methods, the SOFI method optimizes both focality and intensity within safety constraints, resulting in a solution with both high focal accuracy and high intensity. The model

of SOFI can be expressed as follows:

$$\min_x \frac{1}{w} \|Ks\|^2 - \lambda * e_0^T Cx$$

subject to

$$\begin{aligned} & |x_i| \leq I_{max}, i = 1, ..., N \\ & \sum_{i=1}^{N} |x_i| \leq 2 * I_{total} \\ & \sum_{i=1}^{N} x_i = 0 \\ & Intensity_{avoid} \leq \frac{1}{ratio} Intensity_{target} \end{aligned} \tag{5.3}$$

In the objective function, the first term is the focality term, where the constant w is the ratio between the total number of voxels and the number of targeted voxels. The second term is the intensity on the desired direction. The parameter λ balances these two objectives and controls the relative importance of the focality and directional intensity. It can be set empirically or automatically by the L-curve method or cross validation method [Han94]. Since this optimization problem is convex, it can be efficiently solved by softwares such as CVX.

The SOFI method is able to deal with any target location on any tissue with any target orientation. It can not only deal with multiple targets, but also avoid activating certain sensitive regions. In addition, it is very easy to incorporate various safety constraints into the model. Rather than setting a hard constraint at the target like the LCMV method, it allows a range of intensity by changing the parameter λ. It optimizes intensity and focality simultaneously.

To further improve the focality, we can replace the L2 norm with L1 norm to impose sparsity on the target area, for example

$$\min_x \frac{1}{w} \|Ks\|_1 - \lambda * e_0^T Cx \tag{5.4}$$

Furthermore, for spatially extended targets, it is possible to design the current intensity distribution (e.g. uniform, smooth, Gaussian, etc.) at the target depending on the require-

ments of certain applications. This can be achieved by imposing sparsity on a transform domain rather than the original domain:

$$\min_x \frac{1}{w} \|D(Ks)\|_1 - \lambda * e_0^T C x \tag{5.5}$$

where the operator D helps to transform into different domains. For example, if uniform distribution is desired, then we can set D to be the total variation operator to impose sparsity on the first derivative domain; if smooth distribution is desired, D can be set to be Laplacian operator, which imposes sparsity on the second derivative domain. If high-order smoothness or Gaussian distribution is required, we can use total generalized variation (TGV) to impose sparsity on high-order spatial derivative. A similar idea has been adopted in EEG inverse problem in our published papers [LQO16, LQH16] and here we propose to apply it to optimal stimulation.

5.2.3.3 EEG/EMG Inverse Image Guided Optimal Stimulation

One of the limitations of conventional optimization methods is that they require the clinician to specify the location and intensity of the target area, which is unknown in most applications. Recently, a method based on the reciprocity principle was proposed for tDCS [FTL16], which enables the EEG signal to be used as a guide for designing stimulation patterns without specifying the location of target. However, this method is empirical rather than optimal, and it is only able to deal with simple situations, such as cases in which a single focal source predominates. It is unable to handle complicated cases, such as multiple targets, spatially extended targets with different orientations in different parts, or containing brain regions to be avoided.

Unlike the reciprocity principle-based methods that use EEG signal as a guidance, our system uses our dynamic EEG brain image system [LLQ15] as a guide for electrical stimulation. Compared to fMRI, EEG brain imaging provides much higher temporal resolution ($\sim$ms). It is able to provide not only the number and the location, but also the orientation of targets. With our precise EEG source localization method [LQO16, LQH16], our system is able to provide the ability to handle complicated target/avoidance configurations

with high accuracy. The concurrent EEG brain imaging not only provides a guide for dynamic stimulation of complicated neural networks, but also offers real-time feedback of the neuromodulation. Thus a closed-loop stimulation is eminently possible.

5.2.3.4 Quantitative Metric

In order to evaluate the performance of various stimulation methods quantitatively, we use the following criteria:

- Intensity, defined as the average intensity at the target voxels.
- Target Error (TE), defined as the distance between center of mass of the activation area and the target.
- Focality, defined as the radius within which the accumulative energy (square of intensity) is half of the total energy.

Considering that the target orientation also plays an important role on the stimulation effectiveness, we further adopt the following directional criteria:

- Directional Intensity (DI), defined as the average intensity in the desired direction.
- Directional Target Error (DTE). It is similar to target error (TE). The only difference is that we use the total intensity when calculating TE, while using directional intensity for DTE calculation.
- Directional Focality (DF). It is similar to focality, and the only difference is that when calculating DF, we use the directional intensity rather than the total intensity.

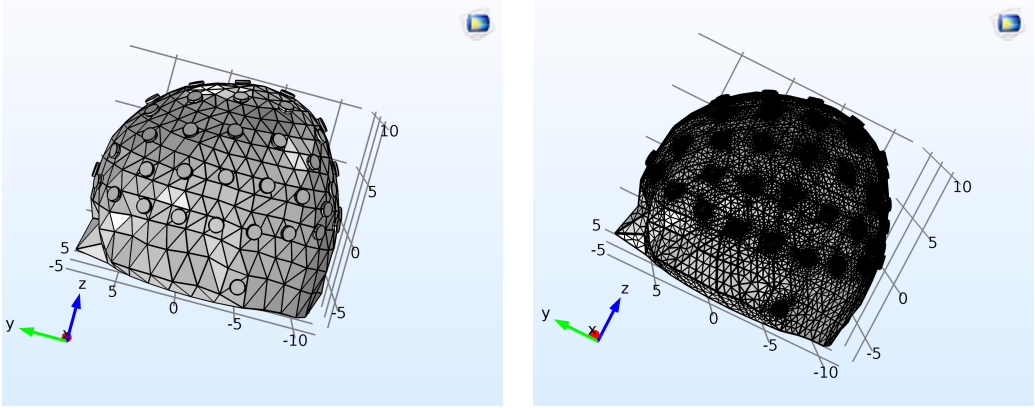

Figure 5.1: Left: realistic head model with 64 electrodes on the scalp. Right: head model after meshing.

5.3 Focalized Transcranial Current Stimulation (tCS)

5.3.1 Realistic Head Model

To design optimal stimulation parameters for tCS, it is necessary to construct a realistic head model. Using a similar method as in Chapter 2, we can construct a realistic head model and source model from high-resolution MR image. In addition, we have built an electrode model containing multiple electrodes, where the electrode locations are from the international standard 10-10 system. Fig. 5.1 shows the head model with 64 electrodes on the left panel, and the head model after meshing on the right panel. In the current electrode model, we use materials of gel and 2mm thick copper, with a diameter of 1.2cm. Note that the number, material, size, pitch, thickness and position of electrodes can be easily modified. With the realistic head model, we further use FEM method to calculate the lead field matrix in COMSOL. For the conductivity of each tissue, we use the values provided in [DDB11].

5.3.2 Experiments and Results

In this section, we first describe the safety limits and simulation protocol we used, then compare the performance of the proposed SOFI method to various state-of-the-art methods, including single small electrode, ring pattern, maximum intensity [DDB11, GDE16], weighted

least square (WLS) [DDB11], and LCMV [DDB11]. In order to have a fair comparison, we restrict the same safety limits (including total current and current for individual electrode) on the three optimization methods: WLS, LCMV and SOFI. For the other three methods that do not use optimization, we only restrict the total current. Additionally, we further compare the LCMV and the SOFI methods in the following cases: single target, multiple targets, and single target with an avoidance region.

5.3.2.1 Safety Limits

For transcranial direct current stimulation (tDCS), there have been different safety criteria in different literatures, including the limits for total current [BNB12, BED13], current density [BNB12], charge density [LKM09], duration [BNB12, SN11], etc. A common criteria shared by most literatures is that the total current should be less than 2mA [BNB12, BED13]. In our study, we restrict both total current and current for individual electrode. Specifically, we use the following constraints: the I_{max} is set to 1mA, the I_{total} is set to 2mA, and the intensity ratio between the target and avoidance region is set to 10. Note that these values can be easily modified to satisfy the requirements of different applications.

5.3.2.2 Simulation Protocol

To test the performance of the proposed SOFI method on tCS, we conduct the simulation on several different cases, including single target, multiple targets, and avoidance region on the cortex surface. Fig. 5.2 shows the target and avoidance region we use. For single target, we use the target on the right hemisphere. For multiple targets, we use two symmetric points on the left and right hemispheres. For the avoidance region, a part of the auditory cortex is used.

5.3.2.3 Results

We compare the performance of the proposed method with various state-of-the-art methods. Fig. 5.3 shows the resulting electrical field, and Fig. 5.4 shows the weighting for each

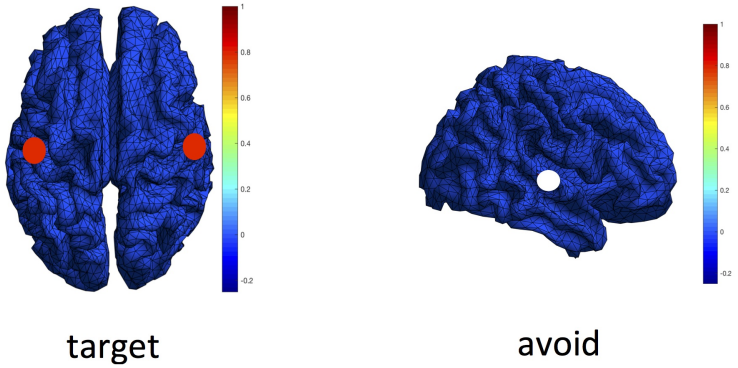

Figure 5.2: Simulated target and avoidance regions on the cortex surface.

electrode. Single electrode and maximum intensity methods show high intensity at the target, but the focality of the electrical field is very low. For the ring configuration, one can see a relatively focal activation area around the target, but its intensity is weak compared to that on the temporal cortex. This might be because the temporal cortex is closer to the scalp electrodes. In contrast, the Weighted LS (WLS), LCMV, and the proposed SOFI method provide a focal result. Compared to the other two methods, the proposed method provides even better intensity and focality.

LCMV is probably the most popular method for optimizing focality so far [DDB11], so we further compare the proposed method to LCMV in different cases: single target, multiple target, single target with avoidance region.

1. Single Target

Fig. 5.5 shows the comparison when there is one prominent target. The quantitative result shows that the proposed SOFI method provides better results than the LCMV, in terms of intensity, directional intensity (DI), target error (TE), and focality. It is worth noting that the focality is larger than 2cm for both methods, which is probably due to the relatively small current we use in tDCS (e.g. total current $\leq$2mA) as well as the high resistivity of the skull. This value matches with the results in other literatures [DDB11, FTL16].

2. Multiple Targets

In addition to single target, we also show that the proposed SOFI method is able to stimulate multiple sites. In Fig. 5.6, two symmetric points on the left and right hemispheres

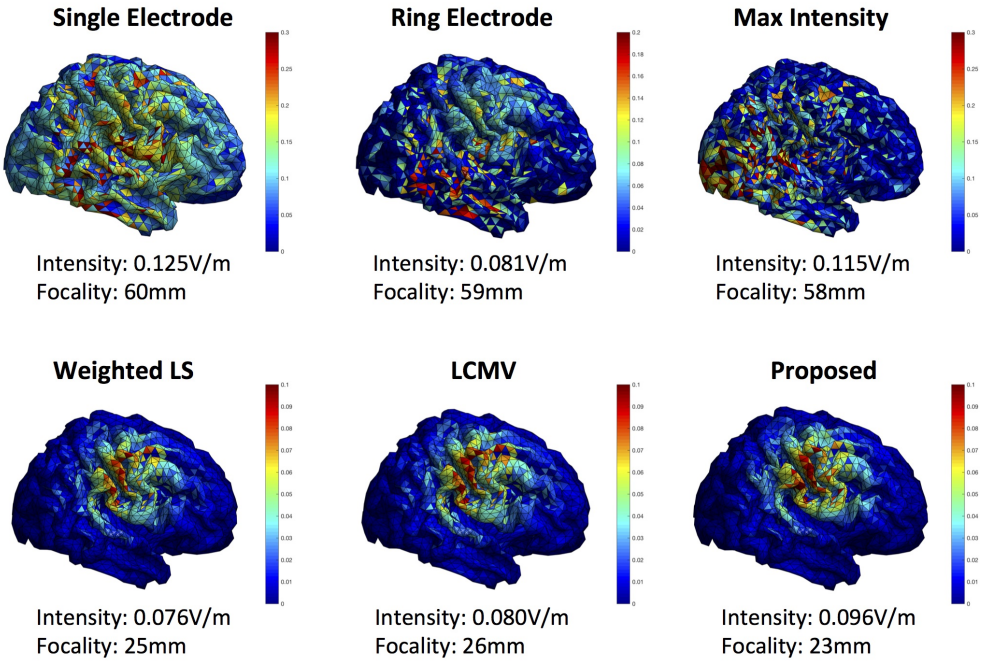

Figure 5.3: Comparison of various transcranial current stimulation methods. The color shows the intensity of the electrical field.

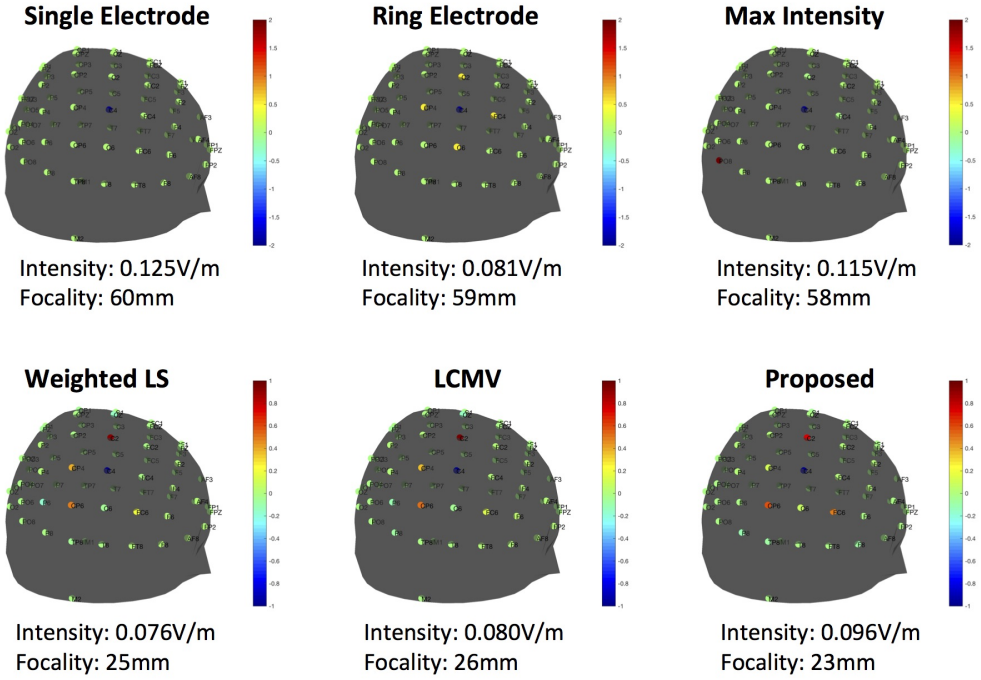

Figure 5.4: Comparison of various transcranial current stimulation methods. The color shows the stimulation parameters at each electrode.

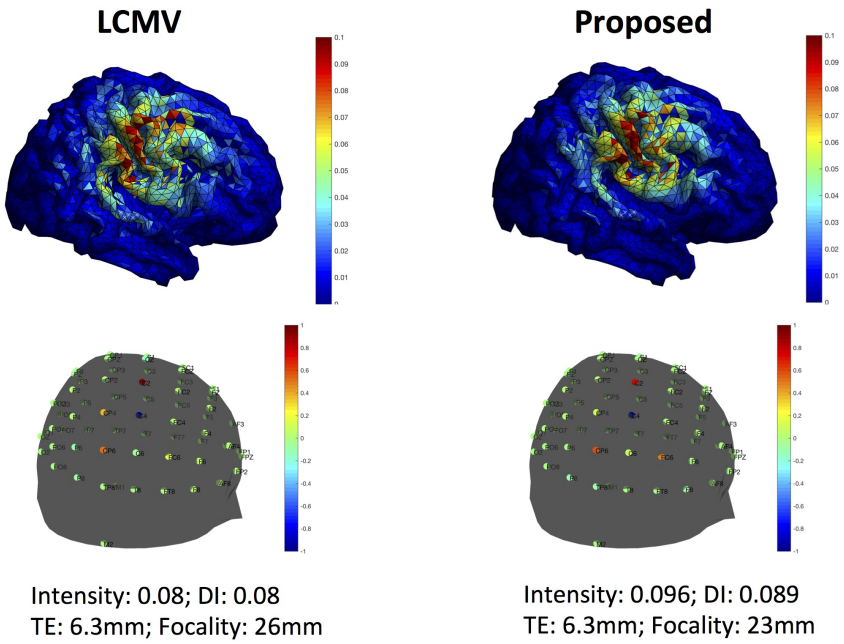

Figure 5.5: Comparison of LCMV and the proposed method with single target.

are set to be the targets. The results show that both methods are able to target both sites. Compared to LCMV, the proposed method shows higher focal accuracy. Note that the focal accuracy for both methods is lower than that in the single target case.

3. Avoidance Region

Fig. 5.7 shows the results when part of the auditory cortex is set to be the avoidance region. One can see that the avoidance region is successfully set to be silent (dark blue color). To avoid the auditory cortex, the activated area of LCMV shifts to the top, resulting in larger target error and lower focal accuracy. In comparison, the proposed method SOFI provides a more focal result with higher localization accuracy.

5.3.3 Conclusion

In summary, we have demonstrated that the SOFI method is able to deal with different complicated cases, such as single target, multiple targets, and target with avoidance region. It is worth noting that the result of single target is the best, since it has less constraints and hence provides a higher degree of freedom to select a better solution. Compared to

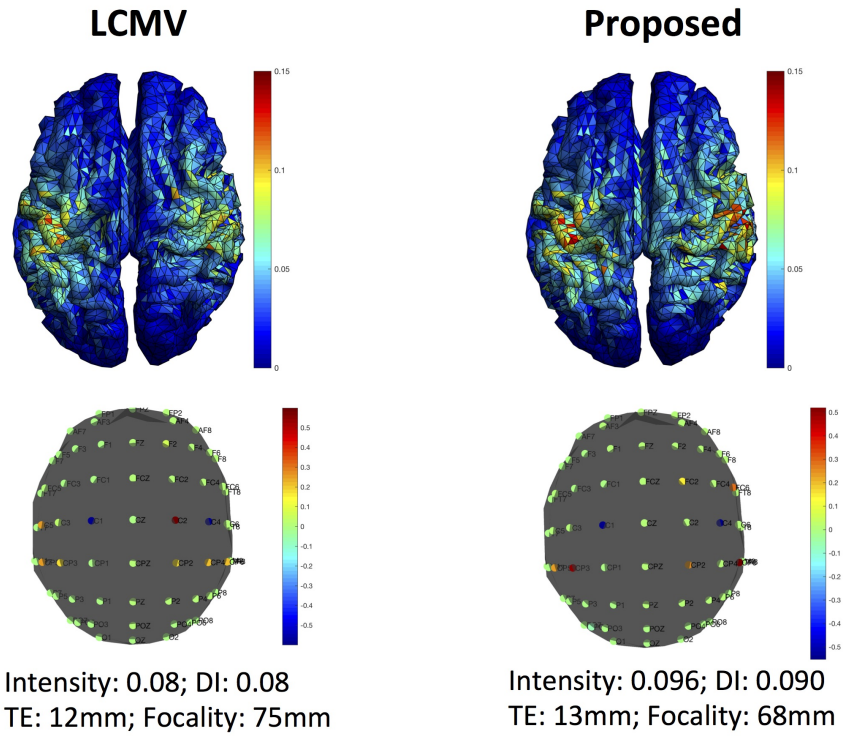

Figure 5.6: Comparison of LCMV and the proposed method using multiple targets.

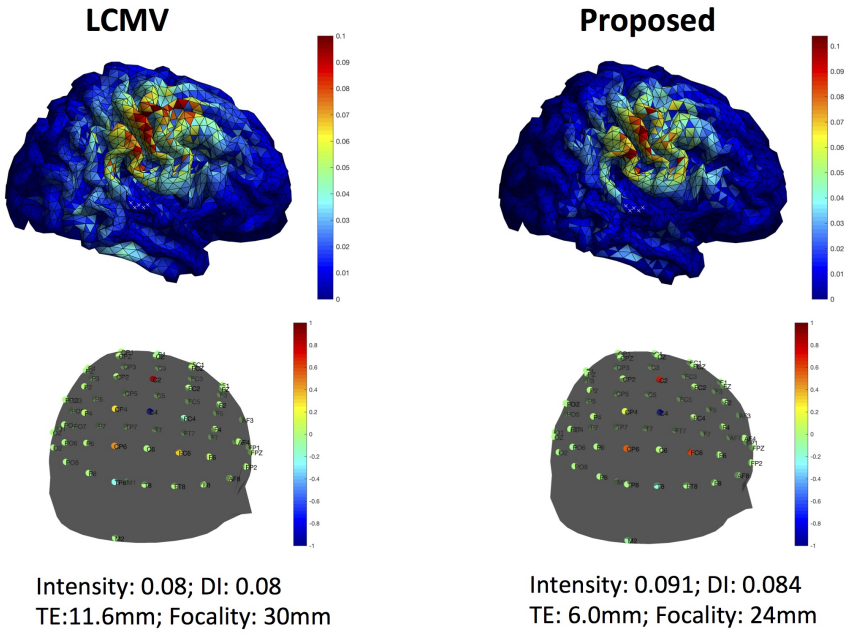

Figure 5.7: Comparison of LCMV and the proposed method using single target with avoidance region.

the maximum intensity and LCMV methods, the SOFI method maximizes the intensity and focal accuracy at the same time and achieves better focality and intensity. Its advantage is especially significant when we require certain regions not to be activated. The SOFI method is able to avoid the region without significantly shifting the activated area, while the LCMV method shifts the activation area, resulting in lower localization accuracy.

5.4 Focalized Transcutaneous Spinal Cord Stimulation (tSCS)

5.4.1 Realistic Spinal Cord Model

To calculate the optimal stimulation parameters, first we need to construct a spinal cord model. Here, we build a realistic spinal cord model based on high-resolution CT/MRI image, which includes the following steps: image segmentation, electrode model construction, and meshing. Then we can apply FEM method to calculate the lead field matrix.

1. Image Segmentation

In this step, we segment the torso into different tissues according to the gray level on the MRI/CT image. The segmentation can be done manually in software such as Solidworks, or automatically in software such as MeVisLab. For tissues that are difficult to be identified from the image, we can build it manually using software such as Solidworks or COMSOL. Fig. 5.8 shows one of the MR image we used.

After image segmentation, we convert 2D segmentation results for each tissue into 3D models with software such as Solidworks. Then we put all of the tissue together to form a whole model. Fig. 5.9 shows a 3D model with different tissues, such as skin (including SC, SG and dermis layers), fat, muscle, vertebrae, spinal nerve, CSF, grey matter, and white matter.

2. Electrode Model Construction

After constructing the 3D model for the spinal cord, we import the model into software such as COMSOL, and construct an electrode model. The electrode model includes a multi-electrode array on the back and one return electrode on the belly. Fig. 5.10 shows the

Figure 5.8: MR image of the torso.

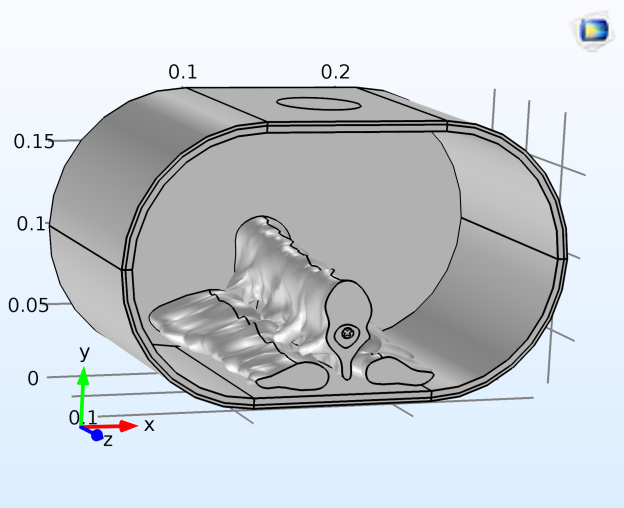

Figure 5.9: Realistic spinal cord model based on individual MRI/CT image.

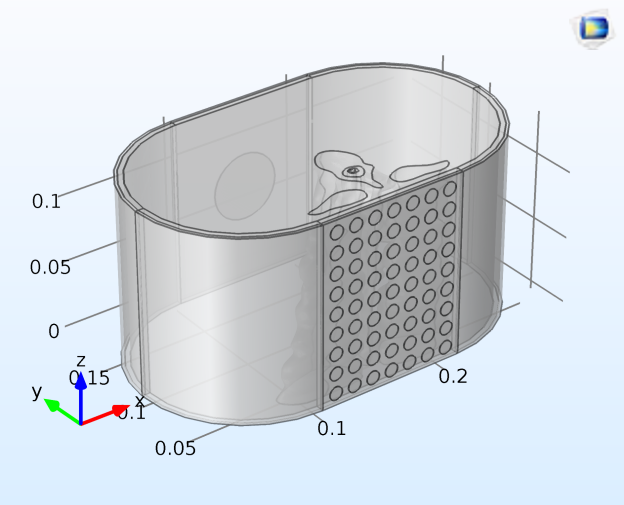

Figure 5.10: Spinal cord model with the multi-electrode array.

spinal cord with the electrodes on it, where we use 9(rows)* 7(columns) small electrodes for stimulation and one large electrode as the return. In the current model, the electrodes use stainless steel, with thickness of $60\mu m$ and diameter $1cm$. Note that the number of electrodes is not limited to 63. The electrode material, size, pitch, thickness, and position can also be easily changed in software such as COMSOL.

3. Meshing

In this step, we discretize the 3D model into a large number of voxels to form a finite element model.

4. Lead Field Matrix Calculation

To calculate the lead field matrix, we can use a finite element method software such as COMSOL. For each electrode, we inject a unit current (density) to it, and compute the resulting voltage/electrical field/current (density)/activation function at each voxel. The obtained values form a vector, which will become the corresponding column for the lead field matrix. Repeating this process will give us the whole lead field matrix. Table 5.1 lists the conductivity values for different tissues we use to calculate the lead field matrix.

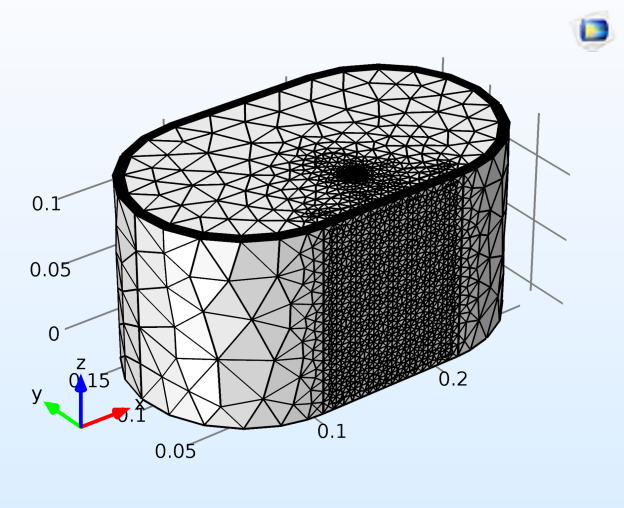

Figure 5.11: Spinal cord model after meshing.

Table 5.1: Conductivity value used for the realistic spinal cord model

Realistic spinal cord model		
	Tissue	Conductivity
Electrical conductivity σ (S)	SC	0.0018
	SG	0.15
	Dermis	1.62
	Fat	0.02383
	Abdomen	0.0414
	Vertebrae	0.0285
	Muscle	0.08 (transversal) / 0.5 (longitudinal)
	CSF	1.7
	Gray matter	0.023
	White matter	0.083 (transversal) / 0.6 (longitudinal)

5.4.2 Experiments and Results

5.4.2.1 Safety Limits

According to [GGM15, GGP15], with a carrier frequency of 10 kHz, the subject can easily tolerate a stimulation intensity from 30 to 200mA for a painless operation. Therefore, here we adopt a safety criteria that the current intensity for each electrode is limited to 100mA, the total current intensity is limited to 200mA, and the intensity in the avoidance region is at least 10 times smaller than that in the target region. It is worth pointing out that the suggested safety limit values $I_{max} = 100mA$ and $I_{total} = 200mA$ can be easily modified.

5.4.2.2 Simulation Protocol

In our simulation study, we simulate three different target configurations to test the performance of the proposed method in different cases (Fig. 5.12), including 1) single target case, in which there is only one target region; 2) multiple targets case, in which there are two target regions; 3) avoidance case, in which we simulate one target along with a nearby avoidance region. In this study, the default target tissue is white matter. This is because the target region is dorsal root or dorsal column in many applications, such as locomotor behavior regulation and pain control. Except for white matter, we also test the case that the target location is on the vertebra (e.g. we choose a spot on the vertebra where there is a cavity so that the current can flow into the spinal cord), and compare the results with that of white matter. For the target orientation, the default orientation is along y-axis (radial to the electrode); we also test the orientation of z-axis and make a comparison between them.

5.4.2.3 Method Comparison

We compare the proposed SOFI method with several state-of-the-art methods in the literature: single large electrode, single small electrode, maximum intensity, ring configuration, and LCMV. Fig. 5.13 shows the stimulation results for each stimulation method.

For single large electrode, single small electrode, and the maximum intensity methods,

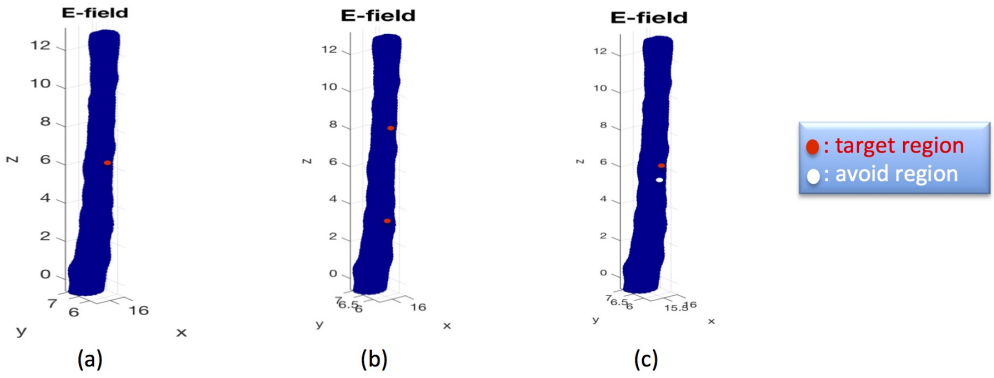

Figure 5.12: Simulated target and avoidance regions. (a) single target. (b) multiple targets. (c) one target region with one nearby avoidance region.

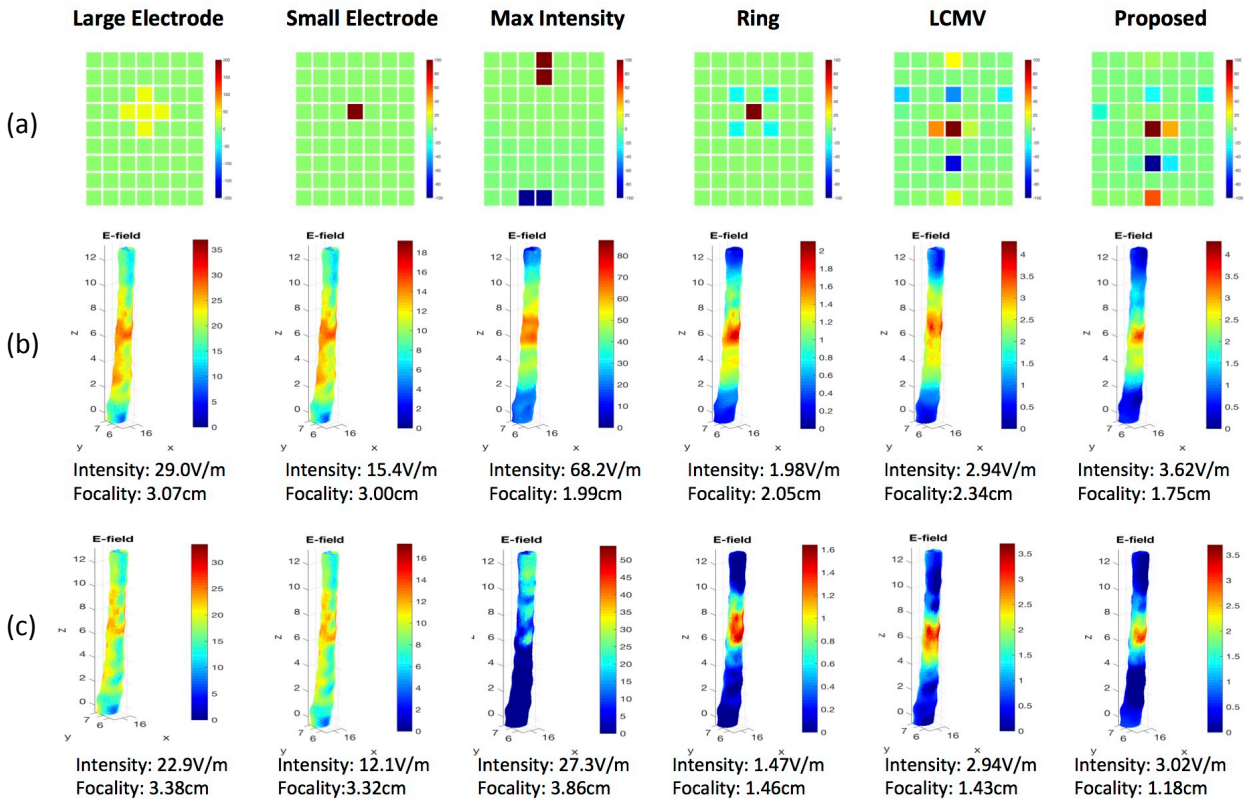

Figure 5.13: Method comparison. (a) stimulation parameter at each electrode; (b) intensity of E-field at the white matter; (c) directional intensity in the desired direction.

the intensity of E-field at the target is very high; however, the E-field is spread out resulting in very low focal accuracy. Among all the methods, the maximum intensity method provides the highest directional intensity and the worst focality. In comparison, the results of ring configuration, LCMV and the proposed method are much more focal. Compared to the other two methods, the proposed method provides the best results in terms of bot intensity and focality.

5.4.2.4 Effect of Various Factors on the Stimulation Results

In the following, we show the influence of different factors, such as target location, target orientation, multiple targets, avoidance region, and parameter λ on the result of the stimulation.

Target Location

The SOFI method is able to target any location including any tissue such as bone and white matter. Deeper source is generally more difficult to target, in terms of intensity and focality at the target. For example, in Fig. 5.14, we compare the results of targeting bone with targeting white matter. As we can see from the results, targeting bone provides much higher target intensity and focality accuracy than targeting white matter, which is reasonable since the electrical field is weakened by the high-resistivity bone when targeting the white matter.

Target Orientation

In addition to target locations, the proposed method is also able to target any orientation. In the previous results (Fig. 5.13), we set the target orientation to be along the y-axis, i.e. radial to the electrode. In the following figure, we show the results of target orientation along the z-axis, i.e. tangential to the electrode, and compare the performance of different stimulation methods. The first row shows the stimulation parameters for each method, and one can see that the weighting for each electrode is very different from that of y-axis orientation (Fig. 5.13 top). For targets with z-axis orientation, generally the stimulation pattern is to place the anode on one side of z-axis and the cathode on the other side. The

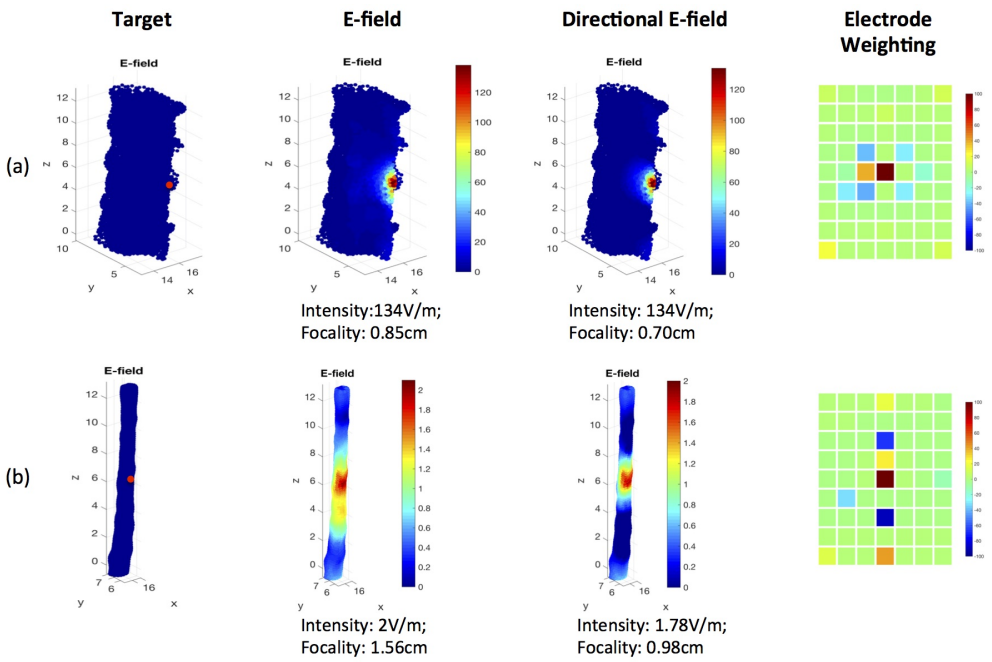

Figure 5.14: Influence of target locations. (a) targeting bone; (b) targeting white matter.

ring configuration has difficulty in dealing with tangential targets, which can be seen from its low target intensity and focal accuracy. To improve the focal accuracy, the LCMV and the SOFI methods place multiple anodes with different weightings rather than only using a single anode/cathode. Compared to other methods, the proposed SOFI method provides the best focal accuracy.

Multiple Targets

The SOFI method is able to deal with not only a single target but also multiple targets. Fig. 5.16 compares the performance of the LCMV and the proposed SOFI methods for targeting two regions. The SOFI method provides better results than the LCMV method in terms of target intensity, localization accuracy, and focal accuracy. Compared to the results of single target (Fig. 5.13), we can see that both target intensity and focality are lower in the multiple targets case, due to additional constraints on the solution.

Avoidance Region

As we know, the ring pattern is unable to avoid certain regions. In contrast, optimization methods including the proposed SOFI method are able to handle that, by restraining the

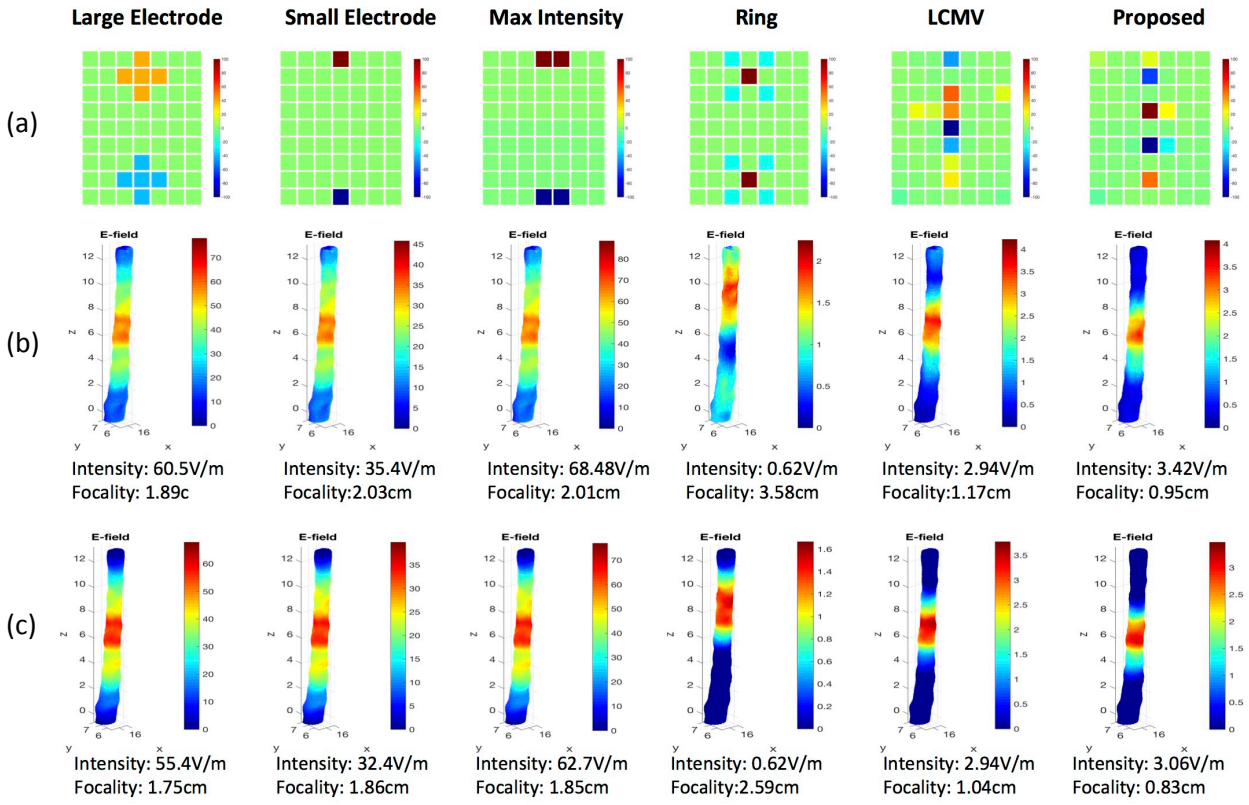

Figure 5.15: Method comparison with target in the direction of z axis. (a) stimulation parameter at each electrode; (b) intensity of E-field at the white matter; (c) directional intensity in the desired direction.

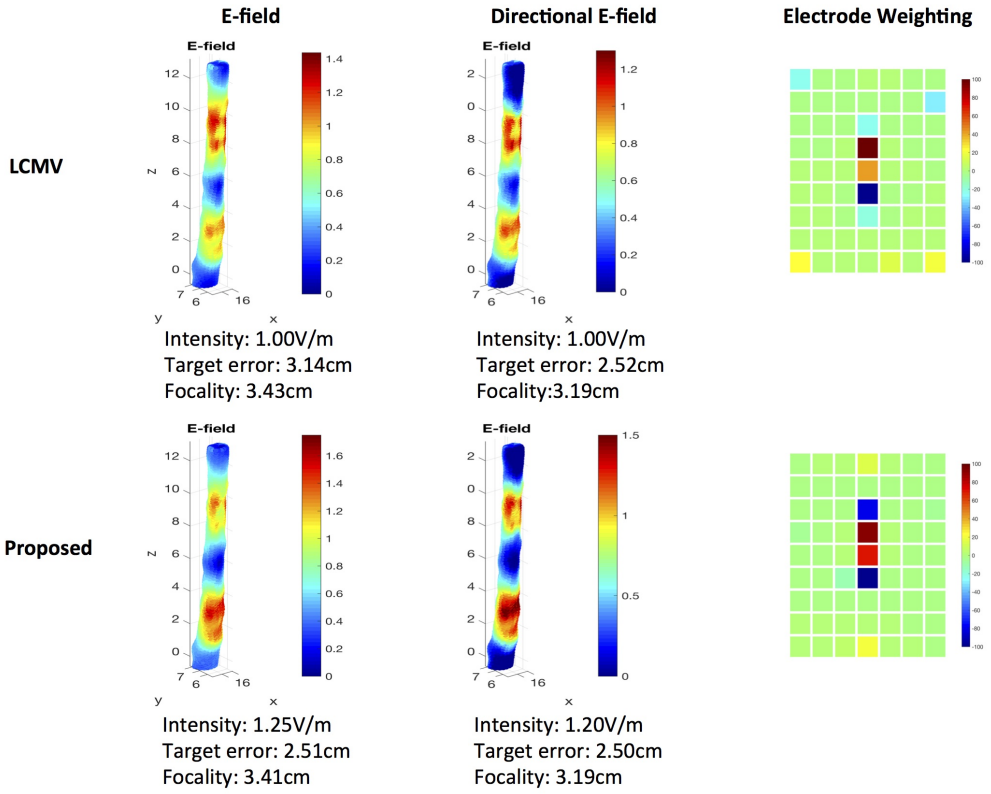

Figure 5.16: Comparison of LCMV and the proposed SOFI method in the case of multiple targets.

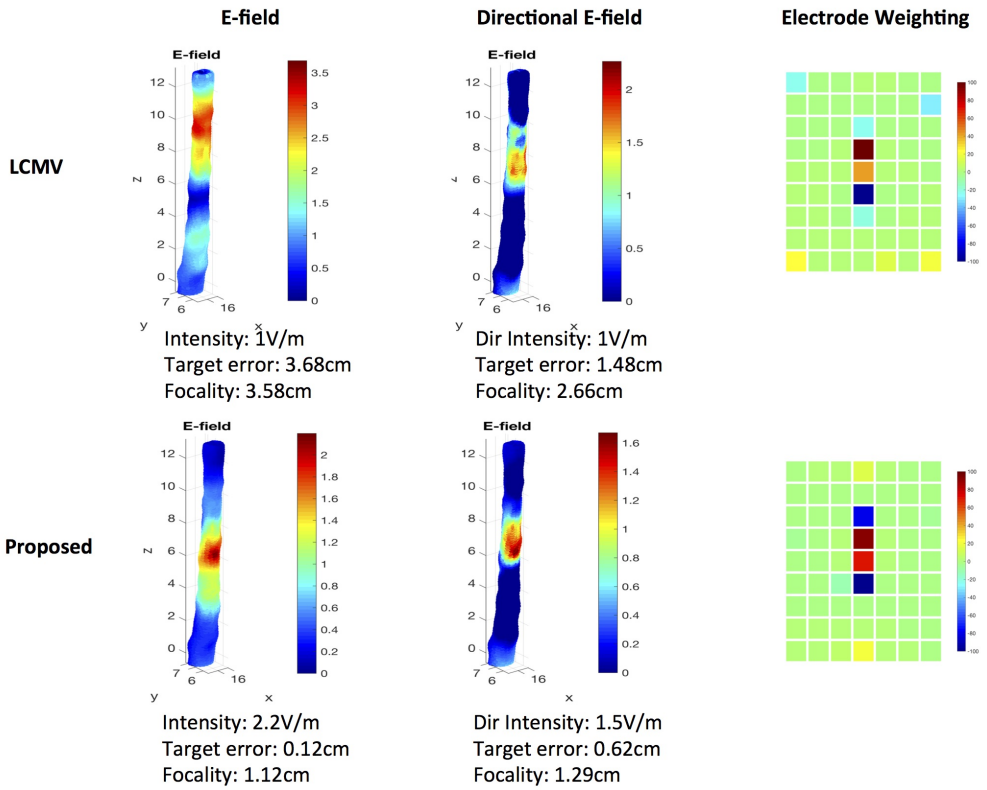

Figure 5.17: Comparison of LCMV and the proposed SOFI method in dealing with avoidance regions.

intensity in the avoidance region to a few times (e.g.10) lower than that in the target region. Fig. 5.17 compares the performance of the LCMV method and the proposed SOFI method when dealing with an avoidance region close to the target region (Fig. 5.12 (c)). The result shows that the LCMV method avoids the region by shifting the activated area away from the target region, leading to larger target error and lower focal accuracy. In contrast, the proposed SOFI method provides much higher localization accuracy and focal accuracy than LCMV method.

Parameter λ

The intensity and focality at the target have an inherent trade-off [DDB11]. In the SOFI method, the parameter λ controls the relative importance between the target intensity and focality, and is critical to the stimulation results. When λ is large, more weight is put on the directional intensity term, therefore the intensity of the results will be high, and vice

versa. By setting λ at a very small value (e.g. 0.01), we can estimate the upper bound of the focality. On the other hand, if setting λ at a very large value (e.g. 1000), we can obtain an upper bound of the intensity. As λ goes to infinity, the proposed method becomes the maximum intensity method (Fig. 5.18). To obtain the best result, selecting an appropriate value of λ is very important.

Fig. 5.18 shows the results of LCMV method, the maximum intensity method, and the proposed SOFI method with different λ. The results show that as λ becomes larger, the directional focality decreases while the directional intensity increases. The result of λ =0.01 estimates the upper bound of directional focality, which is 0.59cm, and λ =1000 estimates the upper bound of directional intensity, which is 27.3V/m. One can see that the results of λ =1000 matches with that of maximum intensity method. In addition, the proposed SOFI method always obtains better results than LCMV in terms of focality and intensity. For example, when λ =2, the SOFI method provides a similar intensity to LCMV, but its focal accuracy is higher; when λ = 4, it provides similar focality to LCMV, but the intensity is much higher.

5.4.3 Conclusion

To the best of our knowledge, this is the first study that uses optimization technique to design optimal stimulation parameters for tSCS. We develop a novel optimization method SOFI, which is able to handle any target location (e.g. on the dorsal root or on the dorsal column) with any orientation. With this method, we can stimulate as deep as the white matter, with focal accuracy around 1cm (Fig. 5.14). In addition, we can stimulate not only single target but also multiple targets, as well as avoid certain regions. We demonstrate that the SOFI method provides better results than other state-of-the-art methods in terms of directional intensity and focality. It is worth noting that adding more constraints (e.g. more targets) on the problem will affect the stimulation performance, due to the reduced degree of freedom.

In the SOFI method, the parameter λ controls the relative importance between the

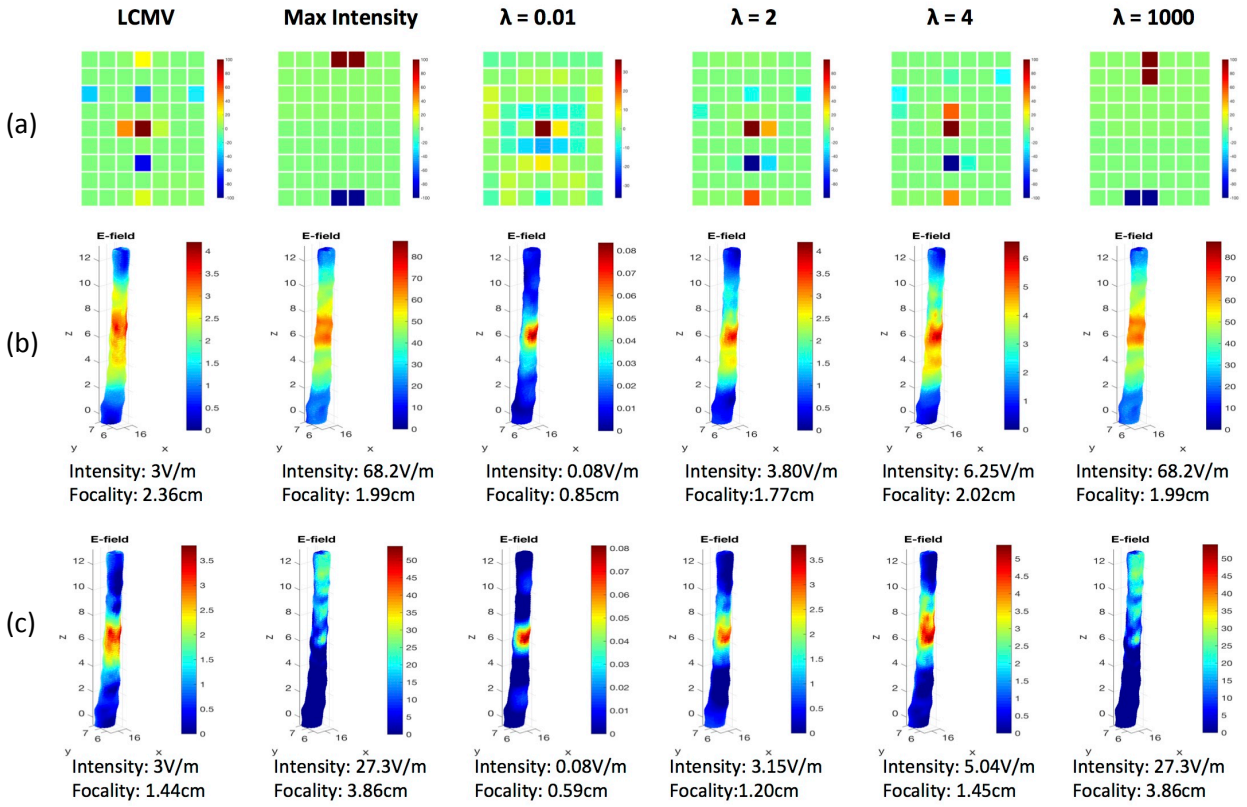

Figure 5.18: Influence of the parameter λ in the proposed method on the stimulation results. (a) stimulation parameter at each electrode; (b) intensity of E-field at the white matter; (c) directional intensity in the desired direction.

intensity and the focality. By changing λ, we can estimate an upper bound of focality and intensity. When λ is very large, we get the best intensity; when λ is very small, we get the best focality. With an appropriate parameter λ, an elegant solution can be obtained with both high intensity and focal accuracy. The parameter λ can be selected manually by experience or automatically by methods such as L-curve or cross validation.

CHAPTER 6

Brain Dynamics Study with Accurate Time-Frequency Analysis

So far, we have presented several brain imaging algorithms that are able to provide images with high reconstruction accuracy, as well as optimization algorithms which can provide focalized and precise stimulation. We have also discussed how to use the neural images to guide the stimulation.

In this chapter, we will further study the neural dynamics quantitatively with accurate time-frequency analysis method. Specifically, we propose to use Hilbert-Huang Transform (HHT), a nonstationary method for analyzing the frequency of neural signal. By applying to seizure detection and cross frequency coupling, we demonstrate that it is able to extract more accurate frequency information than the widely used Fast Fourier Transform (FFT) method.

6.1 Time-Frequency Analysis Methods

6.1.1 Fast Fourier Transform (FFT)

Fourier transform is a widely used frequency analysis technique, which converts a signal from the time domain to the frequency domain. The fast Fourier Transform (FFT) is a computational effective implementation of the discrete Fourier Transform (DFT), which is defined as follows

$$X_k = \sum_{n=0}^{N-1} x_n e^{-i2\pi kn/N} \;\; k = 0, ..., N-1, \tag{6.1}$$

where the $x_0, ..., x_{N-1}$ are the time points of a signal in time domain, while the $X_0, ..., X_{N-1}$ are the output in frequency domain.

Fourier transform assumes that the signal is stationary. However, neural signals such as EEG, ECoG and EMG, are nonstationary, thus the stationary assumption may introduce inaccuracy. It has been demonstrated that the Fourier Transform has deficiency in identifying the low-frequency and high-frequency bands of heart rate variability (HRV), while the nonstationary method Hilbert-Huang Transform (HHT) is able to overcome this limitation and provides superior performance [LKY11].

6.1.2 Hilbert-Huang Transform (HHT)

Hilbert-Huang Transform (HHT) is a powerful tool in dealing with nonlinear and nonstationary signal. It mainly involves two steps: Empirical Mode Decomposition and Hilbert Transform [Hua14].

1. Empirical Mode Decomposition (EMD)

The purpose of EMD is to decompose the signal into some intrinsic mode functions (IMFs) that can be handled by Hilbert Transform. An IMF represents a simple oscillatory mode that is more general and data-adaptive than the harmonic function: it can have a variable amplitude and frequency as functions of time. That is why HHT can deal with nonstationary signals. IMF is defined with two requirements: 1) the number of extrema and the number of zero-crossings must either be equal or differ at most by one; 2) at any point, the mean value of the envelope defined by the local maxima and the envelope defined by the local minima is zero. Fig. 6.1 shows the IMFs of a seizure signal from our database. In the end, the original signal can be expressed as the sum of the IMFs. Let $x(t)$ represent the original signal, c_j represent the IMFs and r_n the residue, then we have

$$x(t) = \sum_{j=1}^{n} c_j(t) + r_n(t). \tag{6.2}$$

Multivariate Empirical Mode Decomposition (MEMD) is an extension of standard EMD

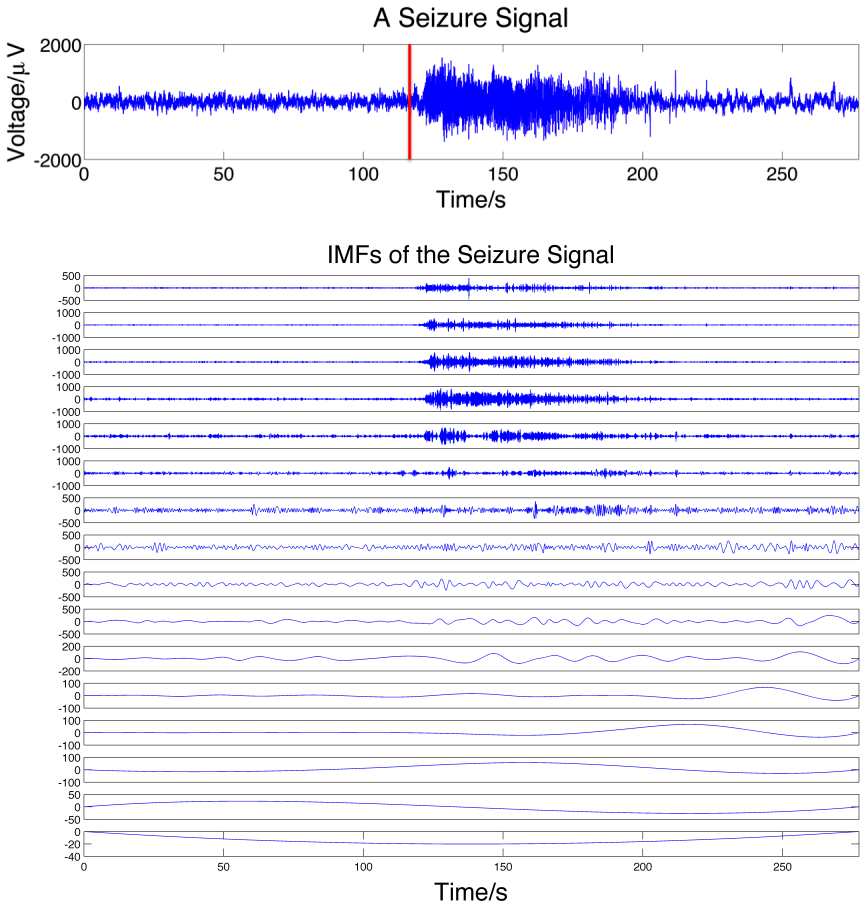

Figure 6.1: Top: A seizure signal from our database (red line is the seizure onset); Bottom: all of the IMFs of the signal.

to multivariate signals, which decomposes signals from several channels simultaneously. MEMD can extract common rotation modes across signal components, thus is more suitable than EMD to decompose the fusion of information from multiple sources [MGK08].

2. Hilbert Transform (HT)

After we decompose the original signal into several IMFs, there is no difficulty to apply the Hilbert Transform to each IMF component. Hilbert Transform is defined as:

$$y(t) = H[x(t)] = \frac{1}{\pi}\mathrm{PV}\int_{-\infty}^{\infty}\frac{x(\tau)}{t-\tau}d\tau. \tag{6.3}$$

Here "PV" indicates the principal value of the singular integral. Now, we can calculate the instantaneous amplitude $a(t)$, phase $\theta(t)$ and frequency $w(t)$ as follows:

$$a(t) = \sqrt{x^2 + y^2}, \theta(t) = arctan(\frac{y}{x}), w(t) = \frac{d\theta}{dt}. \tag{6.4}$$

In the end, the original signal can be expressed as the real part in the following form:

$$x(t) = \Re\left\{ \sum_{j=1}^{n} a_j(t) exp\big[i \int w_j(t) dt\big] \right\}. \tag{6.5}$$

6.2 Seizure Detection

6.2.1 Introduction

Epilepsy is one of the most common neurological diseases, affecting over 3 million people in U.S. and 50 million (∼1%) people worldwide. Electro-Encephalography (EEG) can display clear abnormalities when a seizure begins, thus is very suitable for seizure detection. Conventionally, the detection of seizure is achieved by visual scanning of EEG recordings by an experienced neurophysiologist. However, this method has the drawbacks of time-consuming and subjective. Hence, many algorithms have been developed to detect seizure automatically since 1970s. A seizure detection algorithm usually consists of three stages: 1) frequency/time analysis; 2) feature extraction; 3) classification.

Frequency/time analysis is the first stage of seizure detection algorithm, whose accuracy will directly influence the following two stages. Currently, many researchers use Fast Fourier Transform (FFT), which assumes that the signal is stationary. However, EEG signal itself is nonstationary even within a short window, thus the stationary assumption may introduce inaccuracy. To verify this, we compared the performance of FFT and HHT in seizure detection.

After frequency/time analysis, some features can be extracted to characterize the signal. The features vary from time domain features (such as minimum, maximum, mean, variance, energy, entropy, etc.) [DOY12, LWC10], frequency domain features (such as energy, dominant frequency, weighted frequency, etc.) [Sub07, HHH11, OA11], to features from cross correlation [CCM09], PCA [PG08], ICA [HHH11], etc. Here we used the power in different

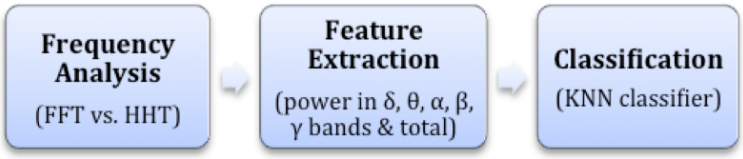

Figure 6.2: Flow chart of the three stages of our algorithm.

frequency bands and the total power as our features. Although Oweis, et al. [OA11] also used HHT for frequency analysis, our features are more effective and achieve much higher accuracy.

After feature extraction, the features will form two classes (seizure or non-seizure) in the feature space. The goal of the classification stage is to classify the testing signal to the seizure or non-seizure class. Some commonly used classifiers include K-nearest neighbor (KNN) [GRD11], artificial neural networks (ANN) [AFA09], support vector machines (SVM) [DOY12, CCM09], etc. In our algorithm, we chose the KNN classifier, which is usually used as benchmark of various classifiers. Combined all of the above three stages, we developed our own seizure detection algorithm.

6.2.2 Methods

Our algorithm consists of three stages: frequency analysis, feature extraction, and classification. Fig. 6.2 shows the flow chart of our algorithm.

1. Frequency Analysis

Fig. 6.3 compares the FFT and HHT frequency spectrum of the signal shown in Fig. 6.1 (top), from which we can have two observations: 1) the resolution of HHT spectrum is better than FFT; 2) FFT has a wider frequency distribution, while HHT stresses on lower frequencies. The reason why HHT can give a more accurate frequency analysis than FFT is as follows: in FFT, the frequency is derived by convolution, thus there will be a trade-off between time resolution and frequency resolution; in HHT, the frequency is derived by differentiation, and hence it is not limited by the uncertainty principle and can provide both high time resolution and high frequency resolution at the same time.

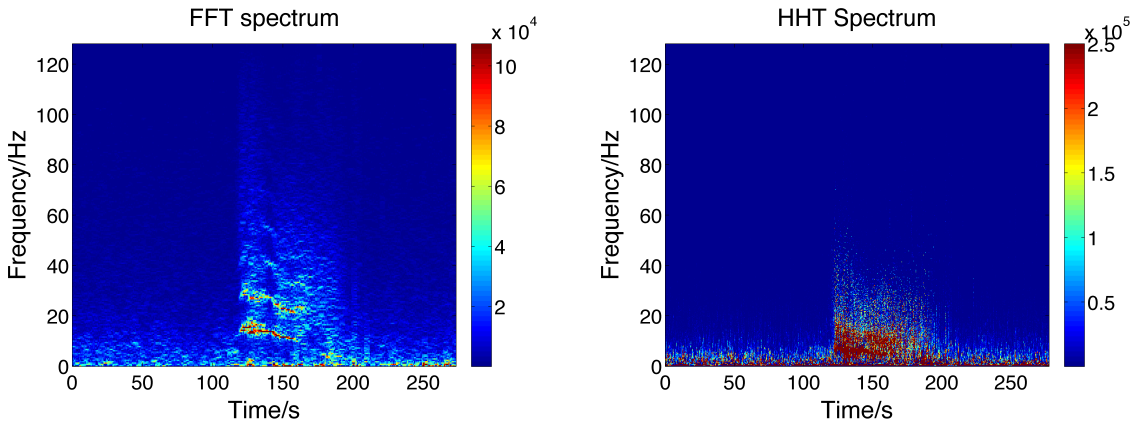

Figure 6.3: Frequency spectrum of FFT (left) and HHT(right).

2. Feature Extraction

After frequency analysis, a total of 7 features were extracted: power in delta (0.5-4Hz), theta (4-8Hz), alpha (8-13Hz), beta (13-30Hz), gamma1 (30-60Hz), gamma2 ($\geq$60Hz) frequency band, and total power.

To calculate the power of a certain frequency band using HHT, we first calculated the energy of each IMF within a small moving window, then summed all of them together and divided by time to get the total power. The energy of each IMF can be calculated as follows: 1) find the time points when the instantaneous frequency located within the frequency band; 2) sum the square of the instantaneous amplitude corresponding to these time points.

Fig. 6.4 shows the power trend of different frequency bands of the signal in Fig. 6.1 (top). From the figure, we can see a dramatic increase of power in some frequency bands when seizure starts. That is why our proposed features are very effective. Moreover, we can see the difference between FFT and HHT again: HHT stresses on lower frequencies.

3. Classification

In this step, the data is separated into training set and testing set. The training set is labeled (seizure or non-seizure class), and the task of the classifier is to predict labels of the testing set. Here we use KNN as our classifier, whose idea is intuitive: it classifies unlabeled examples based on their similarity with examples in the training set.

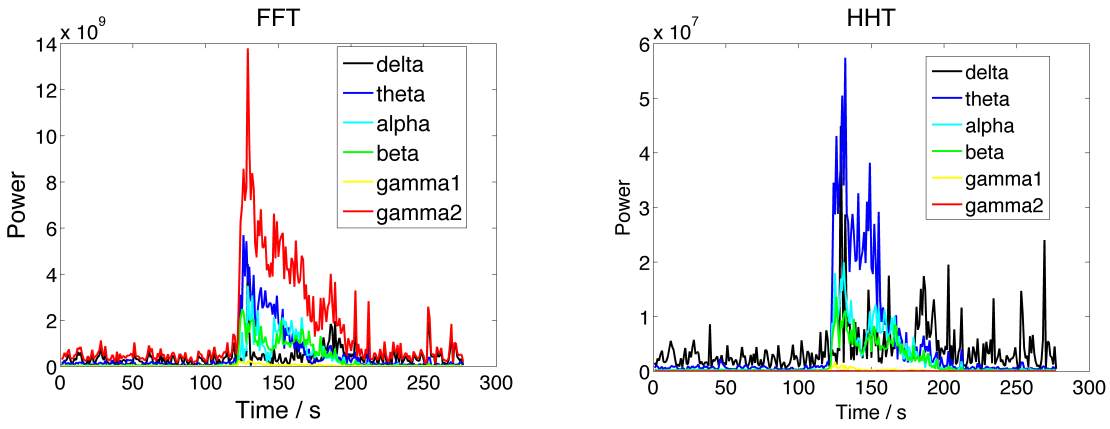

Figure 6.4: Power trend of different frequency bands during a seizure. Left: FFT; Right: HHT.

For example, Fig. 6.5 shows two dimensions of the feature space, from where we can clearly see two classes: seizure (red) and non-seizure signal (blue). Our goal is to find a class label for the unknown testing example x(green). Assume we use $k = 5$ neighbors. After searching for the 5 closest neighbors of x, we find that all of them belong to the seizure class, so x is assigned to the seizure class.

6.2.3 Results and Method Comparison

Three databases were tested here: 1) Bonn database; 2) Freiburg database; 3) Tzu Chi Medical Center database.

6.2.3.1 Result of Bonn database

The Bonn database is available online [ALM01], which was recorded by the University of Bonn. There are a total of five datasets (denoted A-E) each containing 100 single-channel EEG segments of 23.6 s. The sampling rate is 173.61Hz, and the ADC has the spectral bandwidth 0.5 85 Hz. In our study, we use 3 sets of them: A (recorded from healthy volunteers relaxed in an awake state with eyes open); D (recorded within the epileptogenic zones); E (recorded during seizure activities). Fig. 6.6 shows some examples from these

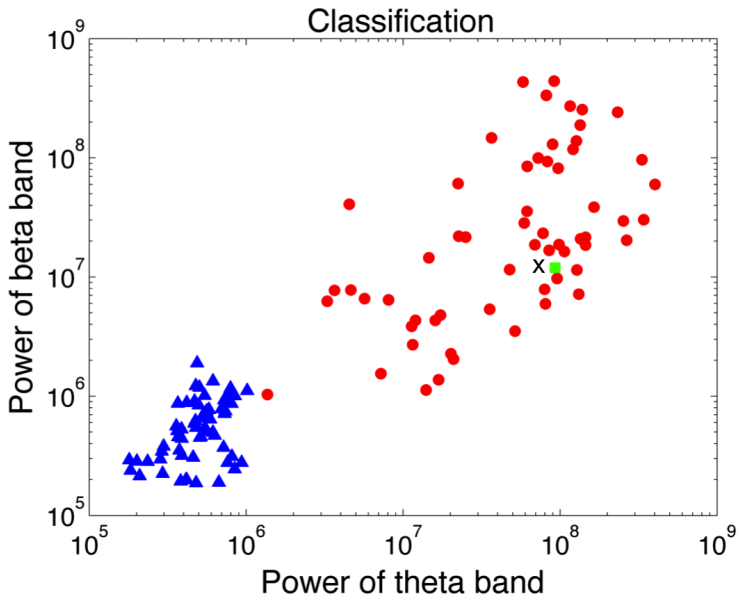

Figure 6.5: KNN classification. Two dimensions of the feature space (log-scale) are shown. x is predicted as "seizure" by the KNN classifier.

3 datasets. Here we formed two classification problems: 1) classify set A (healthy) and E (ictal); 2) classify set D (interictal) and E (ictal). We separated all of the sets into 50% -50% : half for training, and half for testing.

1) A & E classification problem

Table 6.1 shows that our algorithm achieves 100% accuracy for both FFT and HHT, which is a good result compared with other recent algorithms (Table 6.2) [Sub07, PG08, CCM09, OA11]. In addition, the features and classifier of our algorithm are relatively simple

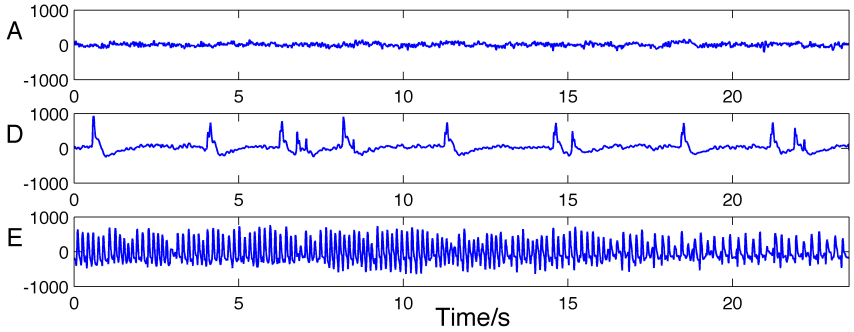

Figure 6.6: Signals of dataset A, D and E from Bonn database.

Table 6.1: Result of the A&E classification problem

Window	***Method***	***Sensitivity***	***Specificity***	***Accuracy***
4096 (23.6s)	FFT	100	100	100
	HHT	100	100	100
2048 (11.8s)	FFT	100	100	100
	HHT	100	100	100
1024 (5.9s)	FFT	100	100	100
	HHT	100	100	100

Table 6.2: Algorithms using Bonn database (A&E)

Authors	***Methods***	***Accu***
Subasi (2007)	Discrete wavelet transform (DWT), mixture of expert model	95
Polat et al. (2008)	Principal Component Analysis and FFT, Artificial immune recognition system	100
Chandaka et al.(2009)	Cross-correlation, LS-Support vector machine	95.95
Oweis et al. (2011)	MEMD or EMD, weighted frequency, t-testing/Euclidean clustering	80% or 94%
Our work	Fast Fourier Transform or Hilbert-Huang Transform, K-nearest neighbor classifer	100

compared to others. For example, Polat, et al. [PG08] also achieved 100% using FFT, but they used more than 100 features.

2) D & E classification problem

D&E problem is more difficult than A&E, since the waveform difference between D&E is not as distinct as that of A&E (Fig. 6.6). Table 6.3 shows the results of using different window lengths. We can see that the accuracy is also very high, and HHT performs better than FFT in all cases.

Table 6.3: Result of the D&E classification problem

Window	***Method***	***Sensitivity***	***Specificity***	***Accuracy***
4096	FFT	94.00	92.00	93.00
(23.6s)	HHT	96.00	94.00	95.00
2048	FFT	95.00	93.00	94.00
(11.8s)	HHT	95.00	94.00	94.50
1024	FFT	94.00	94.50	94.25
(5.9s)	HHT	98.00	94.50	96.25

6.2.3.2 Result of Freiburg database

The Freiburg database was available online by request at `http://epilepsy.uni-freiburg.de/freiburg-seizure-predictionproject/eeg-database`. This database contains intracranial EEG recordings from 21 patients at the Epilepsy Center of the University Hospital of Freiburg. There are in total 87 seizures, 509h of interictal and 73h of preictal or ictal data. For each patient, six channels are available, of which 3 focal and 3 extrafocal electrodes. The data were acquired using a Neurofile NT digital video EEG system with 256 Hz sampling rate, and a 16 bit ADC. Before using this database, we firstly filtered the data by a 50Hz notch filter to remove the line noise.

We tested all the 21 patients (87 seizures and 509 h interictal signals) in the Freiburg database. A window length of 4s was used, since there are many short seizures (<5s) in this database. Our classification criteria are: for ictal signal, as long as one window is classified as "seizure", we will say that a seizure is detected; for interictal signal, if one window is classified as "seizure", then we will report a false alarm.

To guarantee the reliability of our algorithm, we used 21-fold cross validation: use 20 patients for training and one for testing, then repeat this procedure for 21 times. Since there is not enough ictal data for training, we used a window with 80% overlap to generate more training examples. Also, since the interictal signals are very long and they are more than enough for training, thus we randomly picked up 200 windows from each signal. Using FFT, we obtained a sensitivity 89.66% and specificity 93.26% ; for HHT, the results are better:

Table 6.4: Algorithms using Freiburg database

Authors	***# of patients***	***Sensitivity***	***Specificity***
Schad et al. (2008)	6 patients	38%-77%	-
Aarabi et al. (2009)	21 patients	68.9%	97.8%
Orosco et al. (2011)	21 patients	41.4%	79.3%
		69.4	69.2%
Raghunathan et al. (2011)	5 patients	87.5%	99.82%
Our work (FFT)	21 patients	89.66%	93.26%
Our work (HHT)	21 patients	93.10%	95.17%

the sensitivity is 93.10% and specificity is 95.17% (Table 6.4). Also, for some special cases, for example patient 12, FFT gives a very bad specificity (62.98%), but HHT still gives a high specificity (90.64%).

Table 6.4 compares some algorithms using the Freiburg database [SSS08, AFA09, OCL11, RJI11]. The performance of our algorithm is significantly better than others. It seems that the result of Raghunathan, et al. [RJI11] is also good, but they only tested 5 patients, which are relatively easy cases.

6.2.3.3 Result of Tzu Chi Medical Center Database

This database was recorded by our collaborator Dr. Yue-Loong Hsin at Hualein Tzu Chi Medical Center, Taiwan. A total of 33 ictal recordings are available from 13 patients. The sampling rate is 256Hz, and the channel number varies from 5 to 52. Fig. 6.1 (top) is a representative ictal recording from this database.

When testing this database, we used the ictal and interictal signals from the Freiburg database for training. We expect that the signal power between different databases will be different since they use different electrodes for recording. Therefore, we normalized the power in different frequency bands by the total power. The result shows that all of the seizures were detected (100% sensitivity), which have been verified by experienced epileptologists.

6.2.3.4 Compare the Performance of FFT and HHT

All of the above testing results show that HHT outperforms FFT in seizure detection (except when both of them achieve 100% accuracy). It is usually assumed that the signal can be regarded as "stationary" when the window is short. But our results show that even the window is only 4s, HHT still has advantage over FFT. Therefore we conclude that the "stationary assumption" can introduce some inaccuracy, and propose that we should pay attention to the "nonstationarity" of the EEG signal. On the other hand, we should also notice that HHT takes longer time for computation. Hence, our suggestion is using HHT when higher accuracy is required, and using FFT when less computation is required.

6.2.4 Conclusion

We developed a highly accurate seizure detection algorithm whose performance is very competitive among the current algorithms. The features and classifier in our algorithm are simple but very effective, therefore is very suitable for hardware implementation. Most importantly, we conducted a detailed comparison of the stationary method FFT and nonstationary method HHT in seizure detection, and found that HHT offers better performance for difficult cases in aspect of both sensitivity and specificity. To the best of our knowledge, this is the first to compare stationary methods and nonstationary methods in seizure detection. Tradeoff of accuracy and computation power suggests to use FFT when less computation is required and use HHT if higher accuracy is needed.

6.3 Cross Frequency Coupling

6.3.1 Introduction

Cross Frequency Coupling (CFC) is the interaction between brain oscillations of different frequencies, and the coupling phenomenon has been observed in the brain of rodent and human [TKT08, BE04]. Phase-amplitude coupling (PAC) is a type of CFC, which shows the dependence between the phase of a low-frequency component and the amplitude of a

high-frequency component of electrical brain activities [CK10]. It has been claimed that the modulation of low frequency phase on high frequency amplitude plays a functional role in cognition and information processing, such as learning and memory [AHJ10, LJ13]. The low-frequency phase reflects local neuronal excitability, and the increase of high-frequency amplitude shows a general increase in population synaptic activity or selective activation of a connected neuronal subnetwork [CK10]. The change of PAC patterns has been associated with various neurological disorders, e.g., epilepsy, Parkinson′s disease, and schizophrenia [AVW11, LTR10, MH11]. Therefore, PAC shows great potential in diagnosing and treating diseases, and it is critical to understand the biological meaning of PAC patterns.

The conventional method used for PAC analysis first defines the frequency of interest, and then uses narrowband Fourier-based filters to extract different frequency bands. After obtaining signals of different frequencies, it uses Hilbert Transform (HT) to extract instantaneous phase and amplitude signals to calculate the coupling intensity [TKT08, LTR10]. However, this method has several drawbacks: 1) the operation of filtering in frequency space is linear and can cause waveform distortions when applied to nonlinear and nonstationary electrocorticography (ECoG) data [Hua05]; 2) narrowband filter distorts data near the cut-off frequency, and data distortions can be significantly high when the filter is repeatedly used to extract many frequency bands [PHK14]; and 3) since the ECoG signal is not an oscillatory function with zero reference level, the instantaneous phase and amplitude values extracted by HT do not have physical meanings according to Huang [HSL98], which all make the interpretation of comodulogram (coupling map) inaccurate.

In order to overcome the limitation of the conventional method, a novel method based on Hilbert Huang Transform (HHT) is proposed in this study, which displays PAC comodulograms in an IMF domain instead of a traditional frequency domain. As HHT is able to deal with nonstationary and nonlinear signals, the proposed method also avoids distortions from using conventional time-frequency analysis methods like Fast Fourier Transform (FFT). The proposed method consists of two steps: Multivariate Empirical Mode Decomposition (MEMD) and followed by HT. MEMD decomposes the signal into several Intrinsic Mode Functions (IMFs) that are oscillatory functions, thus the instantaneous phase and ampli-

tude extracted by HT are physically meaningful. In this study, we apply the proposed HHT method in analyzing five subsequent seizure EEG (electroencephalography) evolving stages from preictal stage to seizure termination, and compare the PAC patterns obtained by the conventional method and HHT method. The results show that the HHT method overcomes the limitation of the conventional method and shows more regular and clearer PAC patterns across different patients.

6.3.2 Materials and Methods

6.3.2.1 Materials

The intracranial signals were obtained from two epileptic patients with pharmacoresistance undergoing staged epilepsy surgery. For the first patient, the ECoG data were recorded using 4*8 grid electrodes at 256 Hz sampling rate. The ECoG data of the second patient were recorded by three 2*8 grid electrodes at 1024 Hz. Raw signals were filtered by a 0.5 Hz high-pass filter in both two patients, and the signal from the second patient was further filtered by a 300 Hz low-pass filter. In addition, line noise was removed by a 5-order band-stop Butterworth filter. The experimental procedures involving human subjects described in this study were approved by the Institutional Review Board.

6.3.2.2 Stages of Seizure

Regarding the seizure dynamic, each attack is classified by time order as preictal, ictal, and postictal. In this study, the time-series seizure EEG activity is divided into five stages: preictal stage before seizure onset, initial fast EEG activity stage, firing pattern transition stage, fast-burst stage and slow-burst stage before seizure stops (shown in Fig. 6.7).

6.3.2.3 Modulation Index Calculation

There are many quantitative methods for measuring PAC, among which the Kullback-Liebler based modulation index (KL-MI) has many advantages over the other methods, i.e., good

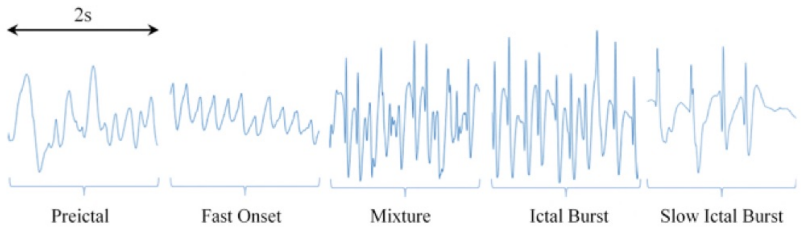

Figure 6.7: Classification of five seizure stages by firing pattern: Preictal = preictal stage, Fast onset = initial fast EEG activity stage, Mixture = firing pattern transition stage, Ictal burst = fast-burst stage, Slow ictal burst = slow-burst stage.

tolerance to noise, amplitude independent, and good sensitivity to multimodality and modulation bandwidth [TKE10]. Therefore, we use KL-MI to measure coupling intensity in this study. The method begins with the average binned amplitude as a function of phase, and then uses KL divergence algorithm to calculate the deviation of this amplitude distribution (P) from a uniform distribution (U) [TKE10, TKM09]. MI is defined by dividing the KL distance by the maximal possible entropy value log (N):

$$MI = \frac{D_{KL}(P,U)}{log(N)} \tag{6.6}$$

The KL distance is related to the Shannon entropy by the following:

$$D_{KL}(P,U) = log(N) + \sum_{j=1}^{N} P(j)log[P(j)] \tag{6.7}$$

Therefore, when amplitude is uniformly distributed over phases (i.e., $P = U$), MI equals to zero and no coupling exists between the amplitude and phase. MI increases as P gets further away from U, meaning the coupling gets stronger.

6.3.2.4 Comodulogram Construction

After computing MI between phase and amplitude from each pair of IMFs, the HHT method displays the comodulogram in an IMF domain which represents the coupling phenomenon between IMFs rather than between frequency bands. As each IMF contains an oscillatory mode and the sum of all the IMFs is the original signal, the IMF-domain comodulogram

does not need to first define the frequency of interest and presents a comprehensive look of coupling phenomenon.

6.3.3 Results and Method Comparison

The conventional method and HHT method are used to analyze the intracranial signals from two epilepsy patients. Comparisons are made between the two methods illustrating PAC phenomenon in the five seizure EEG stages in Fig. 6.8.

It is shown that the phase of delta and theta band modulates the amplitude of gamma-band brain rhythm in epileptogenic cortex [GCC15]. Therefore, the frequency of interest for phase signal is set between 0.5 Hz and 10 Hz in the conventional method. In Patient 1 (left) and Patient 2 (left), the conventional method shows the coupling phenomenon between different frequency bands in a frequency domain. For Patient 1, preictal and initial fast EEG activity stages have similar coupling area (i.e., mainly between 3-8 Hz phase and around 100 Hz amplitude), and the fast onset shows stronger coupling intensity. The firing pattern transition stage and fast-burst stage both show stronger coupling phenomenon than fast onset generally between 2-10 Hz phase and 15-100 Hz amplitude, where the strongest coupling exists between around 4-7 Hz and 40-50 Hz. Slow-burst EEG activity mainly couples between 2-6 Hz phase and 15-60 Hz amplitude with weaker intensity than fast-burst EEG activity. For Patient 2, the coupling is mainly between 0.5-2 Hz phase and 30-100 Hz amplitude in preictal stage, and 0.5-1 Hz phase and around 20-80 Hz, 210-240 Hz and 280-300 Hz amplitude in initial fast EEG activity stage. After the firing transition stage, the coupling sporadically distributes between 0.5-10 Hz phase and 30-100 Hz amplitude, with main coupled phase 0.5-2 Hz. From the two patients, we can see the PAC patterns using the conventional method are not consistent across different patients. Moreover, although a moving window is used in this method to improve frequency resolution, the displayed minimal frequency is limited by sampling rate and the bandwidth of filter, and thus is not able to illustrate delta band (0.5-3 Hz) when the sampling rate is low (Patient 1, left).

As for HHT method, illustrated in Patient 1 (right) and Patient 2 (right), there are

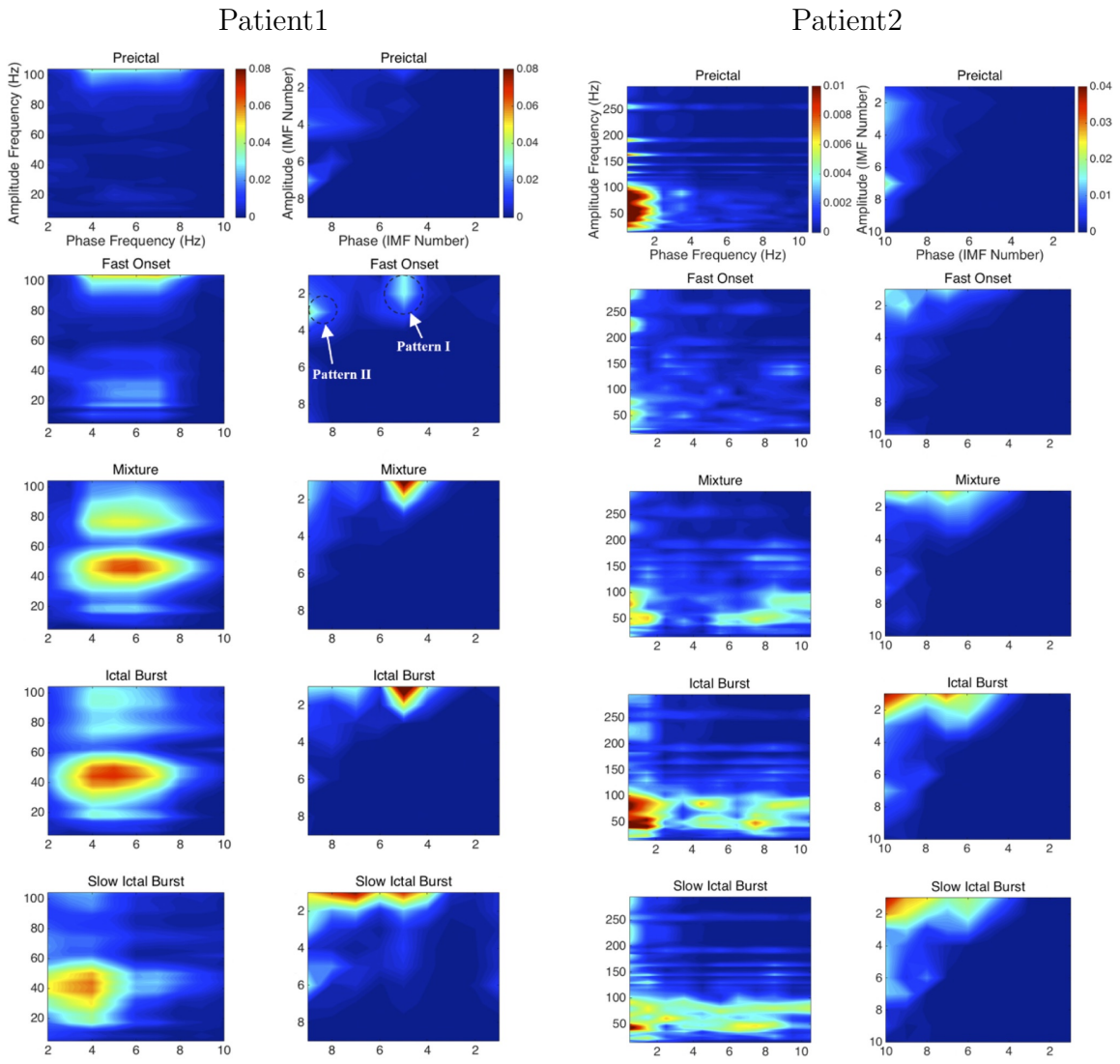

Figure 6.8: Patient 1: PAC comodulogram comparisons between the conventional method (left) and HHT method (right) in five seizure stages. HHT method displays PAC comodulogram in IMF domain instead of traditional frequency domain, and represents coupling phenomenon between certain two IMFs instead of frequency bands. The color bar represents MI. Patient 2: PAC comodulogram comparisons between the conventional method (left) and HHT method (right) in five seizure stages. HHT method shows clear and regular PAC patterns across different stages, while the conventional method does not.

generally two patterns (Pattern I and Pattern II) which are two strongest coupling regions in the IMF-domain comodulograms, both having stronger coupling intensity than that of the conventional method during all stages. During seizure (including fast onset, mixture, ictal burst and slow ictal burst), the location of Pattern I (e.g., in patient 1, Pattern I is the area around 5th-IMF phase coupled with 1st-IMF amplitude) is relatively fixed, with only intensity changing: increasing from seizure onset to fast-burst stage and then decreasing till seizure stops; whereas the location of Pattern II (e.g., in patient 1, Pattern II is the area around 9th-IMF phase coupled with 3rd-IMF amplitude in initial fast EEG activity stage, 9th-IMF phase with 1st-IMF amplitude in firing pattern transition stage, and 7th-IMF phase with 1st-IMF amplitude in bursting stages) changes from fast onset to ictal burst and remains the same from ictal burst to slow ictal burst, while the intensity keeps changing over stages.

As each IMF also has a frequency range, we check the instantaneous frequency of the coupled IMFs in each stage of the two patients and find consistency between the two methods in terms of coupled frequency. Fig. 6.9 illustrates the frequency consistency in the ictal stage (seizure) of patient 1. As it is shown in the IMF-domain comodulogram, the couplings are between 5th-IMF phase and 1st-IMF amplitude, and between 5th-IMF phase and 2nd-IMF amplitude. The frequencies of 1st-2nd IMFs (amplitude) and 5th IMF (phase) are shown in the histograms on the right, where the amplitude frequency mainly ranges approximately from 20 to 50 Hz, and the phase frequency 3-8 Hz, which is consistent with the result shown by the conventional method in frequency bands.

As a result, compared to the conventional method, HHT method shows similar PAC patterns in IMF domain between the two patients, and regular changes across different seizure stages. It also has a more comprehensive PAC presentation and generally stronger coupling intensity (MI) than the conventional method. Therefore, we hypothesize that the IMF may have biological meaning and the real coupling may happen in the IMF domain rather than frequency domain.

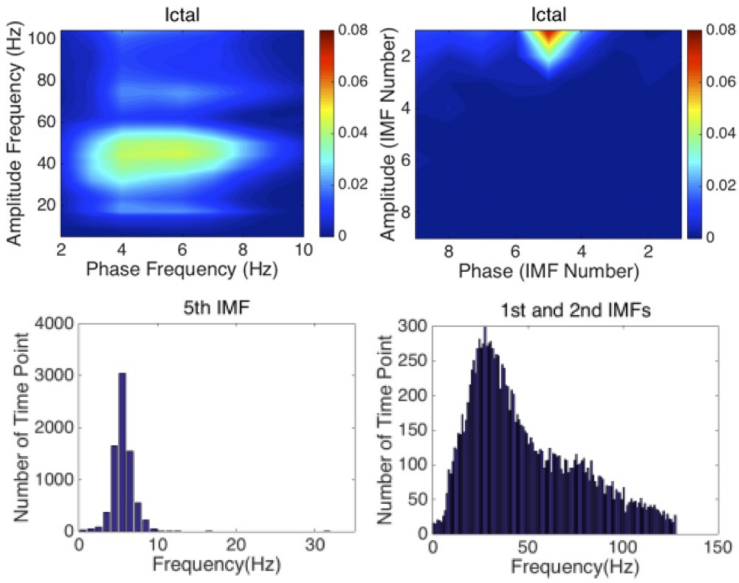

Figure 6.9: Comparisons between the two methods in ictal stage of patient 1 (top); and histograms of the frequency range of 5th IMF (phase) and 1st-2nd IMFs (amplitude) in HHT method (bottom); showing the consistency of the two methods in terms of coupled frequency bands.

6.3.4 Conclusion

We propose a novel method based on HHT to analyze PAC phenomenon in IMF domain, and show new PAC patterns in five seizure stages of two epilepsy patients. The proposed HHT method is superior than the conventional method in terms of 1) able to deal with nonstationary and nonlinear signal, and generates less signal distortions leading to more accurate results; 2) more regular and clearer PAC patterns in IMF domain over five seizure stages in different patients; and 3) generally stronger PAC intensity. The coupling intensity between IMFs is stronger than that is between frequency bands, and the frequency components of coupled IMFs are consistent with the conventional method, which indicates that the real coupling may exist between IMFs rather than traditional frequency bands. For further development, the proposed method also can be applied to EEG signals from patients with different diseases such as schizophrenia, depression, and Alzheimer′s disease.

CHAPTER 7

Conclusions and Future Directions

7.1 Conclusions

In this dissertation, we have developed two novel EEG-based brain imaging methods that provide brain images with high temporal and spatial resolution. Firstly, we develop a Sparsity and SMOOthness enhanced brain TomograpHy (s-SMOOTH) method, which combines the voxel-based total generalized variation (vTGV) and the ℓ_{1-2} regularizations to improve reconstruction accuracy for EEG source imaging. By imposing sparsity constraints on high order spatial derivative, the vTGV regularization enhances the smoothness of the brain image, and helps to accurately reconstruct the current density distribution of the source. Furthermore, the ℓ_{1-2} regularization enhances the sparsity of the brain image, and improves the spatial resolution. A large number of simulation experiments show that the s-SMOOTH outperforms the state-of-the-art methods in terms of total reconstruction accuracy, localization accuracy, and degree of focalization. The application to auditory and visual P300 data further demonstrates its performance in realistic scenario. Secondly, we develop an efficient and accurate EEG brain imaging method by defining a novel graph fractional-order total variation (gFOTV) adapted to the cortical surface. Unlike s-SMOOTH, which incorporates two regularization terms to promote both smoothness and sparsity, the gFOTV method only uses one regularization term but achieves similar accuracy. It imposes sparsity in α-order spatial derivatives with $\alpha \in [1, 2]$, and provides the freedom to choose a more elegant order of smoothness for the underlying brain image. Specifically, we show that $\alpha = 1.6$ provides an accurate result that is smoother than $\alpha = 1$ and more focal than $\alpha = 2$. It is worth mentioning that the gFOTV method consumes less computation than the s-SMOOTH method by

only using one regularization term. Furthermore, we develop a parallel algorithm based on the gFOTV method, which significantly accelerates the numerical solutions. Numerical experiments show that this algorithm running multiple threads on a multi-core system exhibits superior performance in computation time compared to the state-of-the-art optimization algorithm, such as alternating direction methods of multipliers (ADMM). It shows a great potential to achieve real-time temporal resolution, which can potentially bring tremendous convenience and broad influence to clinical applications.

In addition to neural imaging, we have also developed a novel optimization method Stimulation with Optimal Focality and Intensity (SOFI), in order to provide focalized stimulation to treat neural diseases in a noninvasive way. In noninvasive electrical stimulation, the biggest challenge is to achieve both high intensity and high focal accuracy at the target within the safety limits. However, the existing optimization methods either maximize the intensity at the expense of focality, or optimize the focality by sacrificing the intensity. In contrast, the SOFI method is able to optimize both intensity and focality at the target. By applying to transcranial current stimulation (tCS) and transcutaneous spinal cord stimulation (tSCS), we show that the SOFI method is able to target not only a single target, but also multiple targets as well as avoid certain regions with high focal and localization accuracy. For tCS, we have demonstrated that our proposed method provides better results than the state-of-the-art methods in terms of directional intensity, focality, and target accuracy. For tSCS, SOFI is the first optimization method that designs optimal parameters for each electrode to achieve focalized stimulation to the best of our knowledge. We also propose to use the developed EEG-based brain imaging to guide and provide feedback for the focalized stimulation to produce a dynamic stimulation.

Finally, to study the neural dynamics in frequency domain, we propose to use an accurate nonstationary method - Hilbert-Huang Transform (HHT) - for time-frequency analysis. We demonstrate that it outperforms the widely used stationary method - fast Fourier Transform (FFT) - in the applications of seizure detection and cross frequency coupling.

7.2 Future Directions

Currently, neural imaging and stimulation techniques are developed separately. In the future, it would be desirable to incorporate them into a closed-loop system, which includes 1) realistic volume conduction model based on high resolution MRI/CT images; 2) accurate inverse imaging algorithms to provide precise target localization and focal precision with excellent temporal resolution; 3) optimal stimulation patterns with desired intensity guided by our source localization algorithm; 4) miniaturized and fully integrated hardware electronics to independently and dynamically drive each of the multi-electrodes; and 5) user-friendly graphical user interface that will enable home use. In addition, we point out the following future directions for improving the current imaging and stimulation methods.

7.2.1 EEG-based Brain Imaging

We have developed two accurate brain imaging methods: s-SMOOTH and gFOTV. Currently, the EEG source imaging methods work for each time point independently. In the future, the relationship between two contiguous time points could also be modeled so that the brain imaging is done in a spatiotemporal manner. Considering that the current source distributions between consecutive time points usually changes smoothly [BG97, GYO04, ZGB05], the temporal smoothness of the signal could be integrated into the objective function to further improve the reconstruction accuracy [OHG09, GKH12].

So far, the regularization parameters in the models are tuned manually. In the future, the parameters could be selected in an automatic fashion by treating the parameters as unknown variables in the proposed model and then solving the corresponding optimization problem using the bilevel approach [KP13, CCR15, RSV16].

For the gFOTV method, at present, we select a fixed smoothness order for the whole brain image. It is possible that the brain image has different smoothness orders in different subregions. In future work, our proposed framework could be extended by using spatially variant smoothness orders for different subregions in an automatic way to further improve the reconstruction accuracy. In addition, currently the gFOTVE method has only been tested

on synthetic data, and it would be interesting to apply gFOTV to various real scenarios in the future.

7.2.2 Focalized Noninvasive Stimulation

Currently, the research of focalized stimulation focuses on methodologies development. In the future, it would be necessary to test the proposed SOFI method in real experiments to further verify its performance. For transcutaneous spinal cord stimulation (tSCS), it would be interesting to apply the SOFI method to restore motor functions in spinal cord injury (SCI) as well as manage chronic pain. For transcranial current stimulation (tCS), it has shown therapeutic potential for modulating the neural disorders such as depression [LKH06, NBF09], epilepsy [ARG13], stroke, and other illness caused by traumatic brain injury [WCC06, KKP12, SDO14]. It would be interesting to evaluate the SOFI method through sensorimotor and cognitive investigations in these brain disorders.

References

[ACK05] Geoffray Adde, Maureen Clerc, and Renaud Keriven. "Imaging methods for MEG/EEG inverse problem." *International Journal of Bioelectromagnetism*, **7**(2):111–114, 2005.

[AEG14] Claudia A Angeli, V Reggie Edgerton, Yury P Gerasimenko, and Susan J Harkema. "Altering spinal cord excitability enables voluntary movements after chronic complete paralysis in humans." *Brain*, **137**(5):1394–1409, 2014.

[AFA09] A Aarabi, R Fazel-Rezai, and Y Aghakhani. "A fuzzy rule-based system for epileptic seizure detection in intracranial EEG." *Clinical Neurophysiology*, **120**(9):1648–1657, 2009.

[AGA04] H Aurlien, IO Gjerde, JH Aarseth, G Eldøen, B Karlsen, H Skeidsvoll, and NE Gilhus. "EEG background activity described by a large computerized database." *Clinical Neurophysiology*, **115**(3):665–673, 2004.

[AHJ10] Nikolai Axmacher, Melanie M Henseler, Ole Jensen, Ilona Weinreich, Christian E Elger, and Juergen Fell. "Cross-frequency coupling supports multi-item working memory in the human hippocampus." *Proceedings of the National Academy of Sciences*, **107**(7):3228–3233, 2010.

[ALM01] Ralph G Andrzejak, Klaus Lehnertz, Florian Mormann, Christoph Rieke, Peter David, and Christian E Elger. "Indications of nonlinear deterministic and finite-dimensional structures in time series of brain electrical activity: Dependence on recording region and brain state." *Physical Review E*, **64**(6):061907, 2001.

[ARG13] Narong Auvichayapat, Alexander Rotenberg, Roman Gersner, Sudarat Ngodklang, Somsak Tiamkao, Wichittra Tassaneeyakul, and Paradee Auvichayapat. "Transcranial direct current stimulation for treatment of refractory childhood focal epilepsy." *Brain stimulation*, **6**(4):696–700, 2013.

[AVW11] C Alvarado-Rojas, M Valderrama, A Witon, V Navarro, and M Le Van Quyen. "Probing cortical excitability using cross-frequency coupling in intracranial EEG recordings: a new method for seizure prediction." In *2011 Annual International Conference of the IEEE Engineering in Medicine and Biology Society*, pp. 1632–1635. IEEE, 2011.

[BAC14] Hanna Becker, Laurent Albera, Pierre Comon, Rémi Gribonval, and Isabelle Merlet. "Fast, variation-based methods for the analysis of extended brain sources." In *Signal Processing Conference (EUSIPCO), 2014 Proceedings of the 22nd European*, pp. 41–45. IEEE, 2014.

[BBB13] Martin Benning, Christoph Brune, Martin Burger, and Jahn Müller. "Higher-order TV methodsenhancement via Bregman iteration." *Journal of Scientific Computing*, **54**(2-3):269–310, 2013.

[BE04] Andreas Bruns and Reinhard Eckhorn. "Task-related coupling from high-to low-frequency signals among visual cortical areas in human subdural recordings." *International Journal of Psychophysiology*, **51**(2):97–116, 2004.

[BED13] Marcelo T Berlim, Frederique Van den Eynde, and Z Jeff Daskalakis. "Clinical utility of transcranial direct current stimulation (tDCS) for treating major depression: a systematic review and meta-analysis of randomized, double-blind and sham-controlled trials." *Journal of psychiatric research*, **47**(1):1–7, 2013.

[BF07] Jian Bai and Xiang-Chu Feng. "Fractional-order anisotropic diffusion for image denoising." *IEEE transactions on image processing*, **16**(10):2492–2502, 2007.

[BFR06] Paulo S Boggio, Roberta Ferrucci, Sergio P Rigonatti, Priscila Covre, Michael Nitsche, Alvaro Pascual-Leone, and Felipe Fregni. "Effects of transcranial direct current stimulation on working memory in patients with Parkinson's disease." *Journal of the neurological sciences*, **249**(1):31–38, 2006.

[BG97] Sylvain Baillet and Line Garnero. "A Bayesian approach to introducing anatomo-functional priors in the EEG/MEG inverse problem." *Biomedical Engineering, IEEE Transactions on*, **44**(5):374–385, 1997.

[BH14] Kristian Bredies and Martin Holler. "Regularization of linear inverse problems with total generalized variation." *Journal of Inverse and Ill-posed Problems*, **22**(6):871–913, 2014.

[BKI11] Kyung-Yeol Bae, Do-Won Kim, Chang-Hwan Im, and Seung-Hwan Lee. "Source imaging of P300 auditory evoked potentials and clinical correlations in patients with posttraumatic stress disorder." *Progress in Neuro-Psychopharmacology and Biological Psychiatry*, **35**(8):1908–1917, 2011.

[BKP10] Kristian Bredies, Karl Kunisch, and Thomas Pock. "Total generalized variation." *SIAM Journal on Imaging Sciences*, **3**(3):492–526, 2010.

[BNB12] Andre Russowsky Brunoni, Michael A Nitsche, Nadia Bolognini, Marom Bikson, Tim Wagner, Lotfi Merabet, Dylan J Edwards, Antoni Valero-Cabre, Alexander Rotenberg, Alvaro Pascual-Leone, et al. "Clinical research with transcranial direct current stimulation (tDCS): challenges and future directions." *Brain stimulation*, **5**(3):175–195, 2012.

[Cam04] Tracy Cameron. "Safety and efficacy of spinal cord stimulation for the treatment of chronic pain: a 20-year literature review." *Journal of Neurosurgery: Spine*, **100**(3):254–267, 2004.

[CCM09] Suryannarayana Chandaka, Amitava Chatterjee, and Sugata Munshi. "Cross-correlation aided support vector machine classifier for classification of EEG signals." *Expert Systems with Applications*, **36**(2):1329–1336, 2009.

[CCM12] Vincent P Clark, Brian A Coffman, Andy R Mayer, Michael P Weisend, Terran DR Lane, Vince D Calhoun, Elaine M Raybourn, Christopher M Garcia, and Eric M Wassermann. "TDCS guided using fMRI significantly accelerates learning to identify concealed objects." *Neuroimage*, **59**(1):117–128, 2012.

[CCR15] Luca Calatroni, Cao Chung, Juan Carlos De Los Reyes, Carola-Bibiane Schönlieb, and Tuomo Valkonen. "Bilevel approaches for learning of variational imaging models." *arXiv preprint arXiv:1505.02120*, 2015.

[Cec09] RPT Cecilia Norrbrink. "Transcutaneous electrical nerve stimulation for treatment of spinal cord injury neuropathic pain." 2009.

[CK10] Ryan T Canolty and Robert T Knight. "The functional role of cross-frequency coupling." *Trends in cognitive sciences*, **14**(11):506–515, 2010.

[CNH10] Wei-Tang Chang, Aapo Nummenmaa, Jen-Chuen Hsieh, and Fa-Hsuan Lin. "Spatially sparse source cluster modeling by compressive neuromagnetic tomography." *NeuroImage*, **53**(1):146–160, 2010.

[CP11] A. Chambolle and T. Pock. "A first-order primal-dual algorithm for convex problems with applications to imaging." *Journal of Mathematical Imaging and Vision*, **40**(1):120–145, 2011.

[CSZ13] Dali Chen, Shenshen Sun, Congrong Zhang, YangQuan Chen, and Dingyu Xue. "Fractional-order TV-L2 model for image denoising." *Central European Journal of Physics*, **11**(10):1414–1422, 2013.

[DDB11] Jacek P Dmochowski, Abhishek Datta, Marom Bikson, Yuzhuo Su, and Lucas C Parra. "Optimized multi-electrode stimulation increases focality and intensity at target." *Journal of neural engineering*, **8**(4):046011, 2011.

[DDH13] Jacek P Dmochowski, Abhishek Datta, Yu Huang, Jessica D Richardson, Marom Bikson, Julius Fridriksson, and Lucas C Parra. "Targeted transcranial direct current stimulation for rehabilitation after stroke." *Neuroimage*, **75**:12–19, 2013.

[DGP98] Milan R Dimitrijevic, Yuri Gerasimenko, and Michaela M Pinter. "Evidence for a spinal central pattern generator in humansa." *Annals of the New York Academy of Sciences*, **860**(1):360–376, 1998.

[DH08] Lei Ding and Bin He. "Sparse source imaging in electroencephalography with accurate field modeling." *Human brain mapping*, **29**(9):1053–1067, 2008.

[Din09] Lei Ding. "Reconstructing cortical current density by exploring sparseness in the transform domain." *Physics in Medicine and Biology*, **54**(9):2683, 2009.

[DOY12] Firat Duman, Nilüfer Özdemir, and Esen Yildirim. "Patient specific seizure prediction algorithm using Hilbert-Huang transform." In *Proceedings of 2012 IEEE-EMBS International Conference on Biomedical and Health Informatics*, pp. 705–708. IEEE, 2012.

[DS93] Anders M Dale and Martin I Sereno. "Improved localizadon of cortical activity by combining EEG and MEG with MRI cortical surface reconstruction: a linear approach." *Journal of cognitive neuroscience*, **5**(2):162–176, 1993.

[EGR12] V Reggie Edgerton, Yury Gerasimenko, Roland R Roy, and Daniel C Lu. "Transcutaneous spinal cord stimulation: noninvasive tool for activation of locomotor circuitry.", November 13 2012. US Patent App. 14/355,812.

[ELX13] Ernie Esser, Yifei Lou, and Jack Xin. "A method for finding structured sparse solutions to nonnegative least squares problems with applications." *SIAM Journal on Imaging Sciences*, **6**(4):2010–2046, 2013.

[EPY16] B. Edmunds, Z. Peng, and W. Yin. "TMAC: A Toolbox of Modern Async-Parallel, Coordinate, Splitting, and Stochastic Methods." *arXiv preprint arXiv:1606.04551*, 2016.

[FBS06] Felipe Fregni, Paulo S Boggio, Marcelo C Santos, Moises Lima, Adriana L Vieira, Sergio P Rigonatti, M Teresa A Silva, Egberto R Barbosa, Michael A Nitsche, and Alvaro Pascual-Leone. "Noninvasive cortical stimulation with transcranial direct current stimulation in Parkinson's disease." *Movement Disorders*, **21**(10):1693–1702, 2006.

[FHB03] Walter J Freeman, Mark D Holmes, Brian C Burke, and Sampsa Vanhatalo. "Spatial spectra of scalp EEG and EMG from awake humans." *Clinical Neurophysiology*, **114**(6):1053–1068, 2003.

[FKW02] Manfred Fuchs, Jörn Kastner, Michael Wagner, Susan Hawes, and John S Ebersole. "A standardized boundary element method volume conductor model." *Clinical Neurophysiology*, **113**(5):702–712, 2002.

[FTL16] M Fernández-Corazza, S Turovets, P Luu, E Anderson, and D Tucker. "Transcranial Electrical Neuromodulation Based on the Reciprocity Principle. Front." *Psychiatry*, **7**:87, 2016.

[GBC90] Alan Gevins, Paul Brickett, Bryan Costales, Jian Le, and Bryan Reutter. "Beyond topographic mapping: towards functional-anatomical imaging with 124-channel EEGs and 3-D MRIs." *Brain topography*, **3**(1):53–64, 1990.

[GC99] David Jeffrey Griffiths and Reed College. *Introduction to electrodynamics*, volume 3. prentice Hall Upper Saddle River, NJ, 1999.

[GCC15] Mirna Guirgis, Yotin Chinvarun, Martin del Campo, Peter L Carlen, and Berj L Bardakjian. "Defining regions of interest using cross-frequency coupling in extratemporal lobe epilepsy patients." *Journal of neural engineering*, **12**(2):026011, 2015.

[GDE16] Seyhmus Guler, Moritz Dannhauer, Burak Erem, Rob Macleod, Don Tucker, Sergei Turovets, Phan Luu, Deniz Erdogmus, and Dana H Brooks. "Optimization of focality and direction in dense electrode array transcranial direct current stimulation (tDCS)." *Journal of neural engineering*, **13**(3):036020, 2016.

[GER16] Yury Gerasimenko, Victor Reggie Edgerton, Roland R Roy, and Daniel C LU. "MULTI-SITE TRANSCUTANEOUS ELECTRICAL STIMULATION OF THE SPINAL CORD FOR FACILITATION OF LOCOMOTION.", February 4 2016. US Patent 20,160,030,737.

[GGM10] Yury Gerasimenko, Ruslan Gorodnichev, Ekaterina Machueva, Elena Pivovarova, Denis Semyenov, Alexandr Savochin, Roland R Roy, and V Reggie Edgerton. "Novel and direct access to the human locomotor spinal circuitry." *The Journal of Neuroscience*, **30**(10):3700–3708, 2010.

[GGM15] Yury Gerasimenko, Ruslan Gorodnichev, Tatiana Moshonkina, Dimitry Sayenko, Parag Gad, and V Reggie Edgerton. "Transcutaneous electrical spinal-cord stimulation in humans." *Annals of physical and rehabilitation medicine*, **58**(4):225–231, 2015.

[GGP15] Yury Gerasimenko, Ruslan Gorodnichev, Aleksandr Puhov, Tatiana Moshonkina, Aleksandr Savochin, Victor Selionov, Roland R Roy, Daniel C Lu, and V Reggie Edgerton. "Initiation and modulation of locomotor circuitry output with multisite transcutaneous electrical stimulation of the spinal cord in noninjured humans." *Journal of neurophysiology*, **113**(3):834–842, 2015.

[GGR95] Irina F Gorodnitsky, John S George, and Bhaskar D Rao. "Neuromagnetic source imaging with FOCUSS: a recursive weighted minimum norm algorithm." *Electroencephalography and clinical Neurophysiology*, **95**(4):231–251, 1995.

[GKH12] Alexandre Gramfort, Matthieu Kowalski, and Matti Hämäläinen. "Mixed-norm estimates for the M/EEG inverse problem using accelerated gradient methods." *Physics in medicine and biology*, **57**(7):1937, 2012.

[GMP10] RM Gorodnichev, EN Machueva, EA Pivovarova, DV Semenov, SM Ivanov, AA Savokhin, VR Edgerton, and Yu P Gerasimenko. "A new method for the activation of the locomotor circuitry in humans." *Human physiology*, **36**(6):700–707, 2010.

[GPP11] RM Gorodnichev, EA Pivovarova, A Pukhov, SA Moiseev, AA Savokhin, TR Moshonkina, NA Shcherbakova, VA Kilimnik, VA Selionov, IB Kozlovskaia, et al. "Transcutaneous electrical stimulation of the spinal cord: non-invasive tool for activation of locomotor circuitry in human." *Fiziologiia cheloveka*, **38**(2):46–56, 2011.

[GQY14] Weihong Guo, Jing Qin, and Wotao Yin. "A new detail-preserving regularization scheme." *SIAM Journal on Imaging Sciences*, **7**(2):1309–1334, 2014.

[Gra09] Alexandre Gramfort. *Mapping, timing and tracking cortical activations with MEG and EEG: Methods and application to human vision.* PhD thesis, Ecole nationale supérieure des telecommunications-ENST, 2009.

[GRD11] Ling Guo, Daniel Rivero, Julián Dorado, Cristian R Munteanu, and Alejandro Pazos. "Automatic feature extraction using genetic programming: an application to epileptic EEG classification." *Expert Systems with Applications*, **38**(8):10425–10436, 2011.

[Gul98] Ramesh M Gulrajani. *Bioelectricity and biomagnetism*. J. Wiley, 1998.

[GYO04] Andreas Galka, Okito Yamashita, Tohru Ozaki, Rolando Biscay, and Pedro Valdés-Sosa. "A solution to the dynamical inverse problem of EEG generation using spatiotemporal Kalman filtering." *NeuroImage*, **23**(2):435–453, 2004.

[Han94] Per Christian Hansen. "Regularization tools: A Matlab package for analysis and solution of discrete ill-posed problems." *Numerical algorithms*, **6**(1):1–35, 1994.

[HDS06] Ming-Xiong Huang, Anders M Dale, Tao Song, Eric Halgren, Deborah L Harrington, Igor Podgorny, Jose M Canive, Stephen Lewis, and Roland R Lee. "Vector-based spatial–temporal minimum L1-norm solution for MEG." *NeuroImage*, **31**(3):1025–1037, 2006.

[HGH11] Susan Harkema, Yury Gerasimenko, Jonathan Hodes, Joel Burdick, Claudia Angeli, Yangsheng Chen, Christie Ferreira, Andrea Willhite, Enrico Rejc, Robert G Grossman, et al. "Effect of epidural stimulation of the lumbosacral spinal cord on voluntary movement, standing, and assisted stepping after motor complete paraplegia: a case study." *The Lancet*, **377**(9781):1938–1947, 2011.

[HHH11] Yu Han, Yue-Loong Hsin, Tomor Harnod, and Wentai Liu. "Features and futures: seizure detection in partial epilepsies." *Neurosurgery Clinics of North America*, **22**(4):507–518, 2011.

[HHI93] Matti Hämäläinen, Riitta Hari, Risto J Ilmoniemi, Jukka Knuutila, and Olli V Lounasmaa. "Magnetoencephalography–theory, instrumentation, and applications to noninvasive studies of the working human brain." *Reviews of modern Physics*, **65**(2):413, 1993.

[HHK13] US Hofstoetter, C Hofer, H Kern, SM Danner, W Mayr, MR Dimitrijevic, and K Minassian. "Effects of transcutaneous spinal cord stimulation on voluntary locomotor activity in an incomplete spinal cord injured individual." *Biomedical Engineering/Biomedizinische Technik*, 2013.

[HI84] Matti S Hämäläinen and Risto J Ilmoniemi. *Interpreting measured magnetic fields of the brain: estimates of current distributions*. Helsinki University of Technology, Department of Technical Physics, 1984.

[HMT14] Ursula S Hofstoetter, William B McKay, Keith E Tansey, Winfried Mayr, Helmut Kern, and Karen Minassian. "Modification of spasticity by transcutaneous spinal cord stimulation in individuals with incomplete spinal cord injury." *The journal of spinal cord medicine*, **37**(2):202–211, 2014.

[HNZ08] Stefan Haufe, Vadim V Nikulin, Andreas Ziehe, Klaus-Robert Müller, and Guido Nolte. "Combining sparsity and rotational invariance in EEG/MEG source reconstruction." *NeuroImage*, **42**(2):726–738, 2008.

[HSL98] Norden E Huang, Zheng Shen, Steven R Long, Manli C Wu, Hsing H Shih, Quanan Zheng, Nai-Chyuan Yen, Chi Chao Tung, and Henry H Liu. "The empirical mode decomposition and the Hilbert spectrum for nonlinear and non-stationary time series analysis." In *Proceedings of the Royal Society of London A: Mathematical, Physical and Engineering Sciences*, volume 454, pp. 903–995. The Royal Society, 1998.

[HTD11] Stefan Haufe, Ryota Tomioka, Thorsten Dickhaus, Claudia Sannelli, Benjamin Blankertz, Guido Nolte, and Klaus-Robert Müller. "Large-scale EEG/MEG source localization with spatial flexibility." *NeuroImage*, **54**(2):851–859, 2011.

[Hua05] Norden E Huang et al. "Introduction to the Hilbert-Huang Transform and its related mathematical problems." *Interdisciplinary Mathematics*, **5**:1–26, 2005.

[Hua14] Norden Eh Huang. *Hilbert-Huang transform and its applications*, volume 16. World Scientific, 2014.

[IAJ03] Chang-Hwan Im, Kwang-Ok An, Hyun-Kyo Jung, Hyukchan Kwon, and Yong-Ho Lee. "Assessment criteria for MEG/EEG cortical patch tests." *Physics in medicine and biology*, **48**(15):2561, 2003.

[Jeo12] Young Hoon Jeon. "Spinal cord stimulation in pain management: a review." *The Korean journal of pain*, **25**(3):143–150, 2012.

[JLS87] Brian Jeffs, Richard Leahy, and Manbir Singh. "An evaluation of methods for neuromagnetic image reconstruction." *Biomedical Engineering, IEEE Transactions on*, (9):713–723, 1987.

[KBP11] Florian Knoll, Kristian Bredies, Thomas Pock, and Rudolf Stollberger. "Second order total generalized variation (TGV) for MRI." *Magnetic resonance in medicine*, **65**(2):480–491, 2011.

[KDS14] M Krenn, SM Danner, A Schweiger, US Hofstoetter, K Minassian, and W Mayr. "Design of a Multi-site Electrical Stimulation System for Transcutaneous Lumbar Posterior Roots Stimulation." In *International Conference on Advancements of Medicine and Health Care through Technology; 5th–7th June 2014, Cluj-Napoca, Romania*, pp. 43–46. Springer, 2014.

[KHD15] Matthias Krenn, Ursula S Hofstoetter, Simon M Danner, Karen Minassian, and Winfried Mayr. "Multi-Electrode Array for Transcutaneous Lumbar Posterior Root Stimulation." *Artificial organs*, **39**(10):834–840, 2015.

[KKP12] Eun-Kyoung Kang, Dae-Yul Kim, and Nam-Jong Paik. "Transcranial direct current stimulation of the left prefrontal cortex improves attention in patients

with traumatic brain injury: a pilot study." *Journal of rehabilitation medicine*, **44**(4):346–350, 2012.

[KP13] Karl Kunisch and Thomas Pock. "A bilevel optimization approach for parameter learning in variational models." *SIAM Journal on Imaging Sciences*, **6**(2):938–983, 2013.

[KTD13] M Krenn, A Toth, SM Danner, US Hofstoetter, K Minassian, and W Mayr. "Selectivity of transcutaneous stimulation of lumbar posterior roots at different spinal levels in humans." *Biomed Tech (Berl)*, **58**:1–2, 2013.

[LBM11] Martin Luessi, S Derin Babacan, Rafael Molina, James R Booth, and Aggelos K Katsaggelos. "Bayesian symmetrical EEG/fMRI fusion with spatially adaptive priors." *Neuroimage*, **55**(1):113–132, 2011.

[LHL14] Ying Li, Yue-Loong Hsin, and Wentai Liu. "Comparison study of seizure detection using stationary and nonstationary methods." In *2014 36th Annual International Conference of the IEEE Engineering in Medicine and Biology Society*, pp. 3272–3275. IEEE, 2014.

[Lin05] David EJ Linden. "The P300: where in the brain is it produced and what does it tell us?" *The Neuroscientist*, **11**(6):563–576, 2005.

[LJ13] John E Lisman and Ole Jensen. "The theta-gamma neural code." *Neuron*, **77**(6):1002–1016, 2013.

[LKH06] David Liebetanz, Florian Klinker, Diana Hering, Reinhard Koch, Michael A Nitsche, Heidrun Potschka, Wolfgang Löscher, Walter Paulus, and Frithjof Tergau. "Anticonvulsant Effects of Transcranial Direct-current Stimulation (tDCS) in the Rat Cortical Ramp Model of Focal Epilepsy." *Epilepsia*, **47**(7):1216–1224, 2006.

[LKM09] David Liebetanz, Reinhard Koch, Susanne Mayenfels, Fatima König, Walter Paulus, and Michael A Nitsche. "Safety limits of cathodal transcranial direct current stimulation in rats." *Clinical Neurophysiology*, **120**(6):1161–1167, 2009.

[LKY11] Helong Li, Sam Kwong, Lihua Yang, Daren Huang, and Dongping Xiao. "Hilbert-Huang transform for analysis of heart rate variability in cardiac health." *IEEE/ACM Transactions on Computational Biology and Bioinformatics (TCBB)*, **8**(6):1557–1567, 2011.

[LL16] Ying Li and Wentai Liu. "Focalized Noninvasive Stimulation with Optimization Technique.", December 6 2016. UCLA Case No. UC-2017-497-1-LA.

[LLQ15] Ying Li, Wentai Liu, Jing Qin, Chih-Wei Chang, and Yi-Kai Lo. "Ultra-Dense Electrode-Based Brain Imaging System With High Spatial And Temporal Resolution.", September 7 2015. Serial No. PCT/US2016/050452, UCLA Case No. UC-2016-151-2-LA-FP.

[LPF99] David EJ Linden, David Prvulovic, Elia Formisano, Martin Völlinger, Friedhelm E Zanella, Rainer Goebel, and Thomas Dierks. "The functional neuroanatomy of target detection: an fMRI study of visual and auditory oddball tasks." *Cerebral Cortex*, **9**(8):815–823, 1999.

[LQH16] Ying Li, Jing Qin, Yue-Loong Hsin, Stanley Osher, and Wentai Liu. "s-SMOOTH: Sparsity and Smoothness Enhanced EEG Brain Tomography." *Frontiers in Neuroscience*, **10**:543, 2016.

[LQO16] Ying Li, Jing Qin, Stanley Osher, and Wentai Liu. "Graph fractional-order total variation EEG source reconstruction." In *Engineering in Medicine and Biology Society (EMBC), 2016 IEEE 38th Annual International Conference of the*, pp. 101–104. IEEE, 2016.

[LTR10] Jon López-Azcárate, Mikel Tainta, María C Rodríguez-Oroz, Miguel Valencia, Rafael González, Jorge Guridi, Jorge Iriarte, José A Obeso, Julio Artieda, and Manuel Alegre. "Coupling between beta and high-frequency activity in the human subthalamic nucleus may be a pathophysiological mechanism in Parkinson's disease." *The Journal of neuroscience*, **30**(19):6667–6677, 2010.

[LWC10] Sheng-Fu Liang, Hsu-Chuan Wang, and Wan-Lin Chang. "Combination of EEG complexity and spectral analysis for epilepsy diagnosis and seizure detection." *EURASIP Journal on Advances in Signal Processing*, **2010**(1):1, 2010.

[LYH15] Yifei Lou, Penghang Yin, Qi He, and Jack Xin. "Computing Sparse Representation in a Highly Coherent Dictionary Based on Difference of L1 and L2." *Journal of Scientific Computing*, **64**(1):178–196, 2015.

[LZD12] Ke Liao, Min Zhu, Lei Ding, Sébastien Valette, Wenbo Zhang, and Deanna Dickens. "Sparse imaging of cortical electrical current densities via wavelet transforms." *Physics in medicine and biology*, **57**(21):6881, 2012.

[MAS14] Sergio Machado, Oscar Arias-Carrión, Isabel Sampaio, Juliana Bittencourt, Bruna Velasques, Silmar Teixeira, Antonio Egídio Nardi, Roberto Piedade, and Pedro Ribeiro. "Source Imaging of P300 Visual Evoked Potentials and Cognitive Functions in Healthy Subjects." *Clinical EEG and neuroscience*, **45**(4):262, 2014.

[MGK08] Danilo Mandic, Martin Golz, Anthony Kuh, Dragan Obradovic, and Toshihisa Tanaka. *Signal processing techniques for knowledge extraction and information fusion*. Springer, 2008.

[MH11] Lauren V Moran and L Elliot Hong. "High vs low frequency neural oscillations in schizophrenia." *Schizophrenia bulletin*, p. sbr056, 2011.

[MJS04] Christoph Mulert, Lorenz Jäger, Robert Schmitt, Patrick Bussfeld, Oliver Pogarell, Hans-Jürgen Möller, Georg Juckel, and Ulrich Hegerl. "Integration of fMRI and simultaneous EEG: towards a comprehensive understanding of localization

and time-course of brain activity in target detection." *Neuroimage*, **22**(1):83–94, 2004.

[MLL92] John C Mosher, Paul S Lewis, and Richard M Leahy. "Multiple dipole modeling and localization from spatio-temporal MEG data." *Biomedical Engineering, IEEE Transactions on*, **39**(6):541–557, 1992.

[MML04] Christoph M Michel, Micah M Murray, Göran Lantz, Sara Gonzalez, Laurent Spinelli, and Rolando Grave de Peralta. "EEG source imaging." *Clinical neurophysiology*, **115**(10):2195–2222, 2004.

[MO95] Kanta Matsuura and Yoichi Okabe. "Selective minimum-norm solution of the biomagnetic inverse problem." *IEEE Transactions on Biomedical Engineering*, **42**(6):608–615, 1995.

[MPR07a] Karen Minassian, Ilse Persy, Frank Rattay, Milan R Dimitrijevic, Christian Hofer, and Helmut Kern. "Posterior root–muscle reflexes elicited by transcutaneous stimulation of the human lumbosacral cord." *Muscle & nerve*, **35**(3):327–336, 2007.

[MPR07b] Karen Minassian, Ilse Persy, Frank Rattay, Michaela M Pinter, Helmut Kern, and Milan R Dimitrijevic. "Human lumbar cord circuitries can be activated by extrinsic tonic input to generate locomotor-like activity." *Human movement science*, **26**(2):275–295, 2007.

[MSB08] A Molins, Steven M Stufflebeam, Emery N Brown, and Matti S Hämäläinen. "Quantification of the benefit from integrating MEG and EEG data in minimum ℓ_2-norm estimation." *Neuroimage*, **42**(3):1069–1077, 2008.

[NBF09] Michael A Nitsche, Paulo S Boggio, Felipe Fregni, and Alvaro Pascual-Leone. "Treatment of depression with transcranial direct current stimulation (tDCS): a review." *Experimental neurology*, **219**(1):14–19, 2009.

[NS06] Paul L Nunez and Ramesh Srinivasan. *Electric fields of the brain: the neurophysics of EEG*. Oxford university press, 2006.

[OA11] Rami J Oweis and Enas W Abdulhay. "Seizure classification in EEG signals utilizing Hilbert-Huang transform." *Biomedical engineering online*, **10**(1):1, 2011.

[OCL11] Lorena Orosco, Agustina Garcés Correa, and Eric Laciar Leber. "Epileptic seizures detection based on empirical mode decomposition of EEG signals." *MANAGEMENT OF EPILEPSY–RESEARCH, RESULTS AND TREATMENT*, **1**, 2011.

[OFC13] Maryam Odabaee, Walter J Freeman, Paul B Colditz, Ceon Ramon, and Sampsa Vanhatalo. "Spatial patterning of the neonatal EEG suggests a need for a high number of electrodes." *Neuroimage*, **68**:229–235, 2013.

[OFM11] Robert Oostenveld, Pascal Fries, Eric Maris, and Jan-Mathijs Schoffelen. "FieldTrip: open source software for advanced analysis of MEG, EEG, and invasive electrophysiological data." *Computational intelligence and neuroscience*, **2011**, 2011.

[OHG09] Wanmei Ou, Matti S Hämäläinen, and Polina Golland. "A distributed spatio-temporal EEG/MEG inverse solver." *NeuroImage*, **44**(3):932–946, 2009.

[OS74] K. B. Oldham and J. Spanier. *The Fractional Calculus*. Academic Press, New York, 1974.

[OSP03] Robert Oostenveld, Dick F Stegeman, Peter Praamstra, and Adriaan van Oosterom. "Brain symmetry and topographic analysis of lateralized event-related potentials." *Clinical neurophysiology*, **114**(7):1194–1202, 2003.

[OV91] Thom Oostendorp and Adriaan Van Oosterom. "The potential distribution generated by surface electrodes in inhomogeneous volume conductors of arbitrary shape." *Biomedical Engineering, IEEE Transactions on*, **38**(5):409–417, 1991.

[Pas99] Roberto Domingo Pascual-Marqui. "Review of methods for solving the EEG inverse problem." *International journal of bioelectromagnetism*, **1**(1):75–86, 1999.

[Pas02] Roberto Domingo Pascual-Marqui. "Standardized low-resolution brain electromagnetic tomography (sLORETA): technical details." *Methods Find Exp Clin Pharmacol*, **24**(Suppl D):5–12, 2002.

[PC11] T. Pock and A. Chambolle. "Diagonal preconditioning for first order primal-dual algorithms in convex optimization." In *2011 International Conference on Computer Vision*, pp. 1762–1769. IEEE, 2011.

[PG08] Kemal Polat and Salih Güneş. "Artificial immune recognition system with fuzzy resource allocation mechanism classifier, principal component analysis and FFT method based new hybrid automated identification system for classification of EEG signals." *Expert Systems with Applications*, **34**(3):2039–2048, 2008.

[PGD00] MM Pinter, F Gerstenbrand, and MR Dimitrijevic. "Epidural electrical stimulation of posterior structures of the human lumbosacral cord: 3. Control of spasticity." *Spinal cord*, **38**(9):524–531, 2000.

[PHK14] Benjamin Pittman-Polletta, Wan-Hsin Hsieh, Satvinder Kaur, Men-Tzung Lo, and Kun Hu. "Detecting phase-amplitude coupling with high frequency resolution using adaptive decompositions." *Journal of neuroscience methods*, **226**:15–32, 2014.

[PML94] Roberto D Pascual-Marqui, Christoph M Michel, and Dietrich Lehmann. "Low resolution electromagnetic tomography: a new method for localizing electrical activity in the brain." *International Journal of psychophysiology*, **18**(1):49–65, 1994.

[PNH14] Yury Petrov, Jeffrey Nador, Christopher Hughes, Stanley Tran, Ozgur Yavuzcetin, and Srinivas Sridhar. "Ultra-dense EEG sampling results in two-fold increase of functional brain information." *NeuroImage*, **90**:140–145, 2014.

[PS04] Russell A Poldrack and Rebecca Sandak. "Introduction to this special issue: The cognitive neuroscience of reading." *Scientific Studies of Reading*, **8**(3):199–202, 2004.

[PV15] Konstantinos Papafitsoros and Tuomo Valkonen. "Asymptotic behaviour of total generalised variation." In *International Conference on Scale Space and Variational Methods in Computer Vision*, pp. 702–714. Springer, 2015.

[PWX16] Z. Peng, T. Wu, Y. Xu, M. Yan, and W. Yin. "Coordinate friendly structures, algorithms and applications." *Annals of Mathematical Sciences and Applications*, **1**:57–119, 2016.

[PXY16] Z. Peng, Y. Xu, M. Yan, and W. Yin. "ARock: an algorithmic framework for asynchronous parallel coordinate updates." *SIAM Journal on Scientific Computing*, **38**(5):A2851CA2879, 2016.

[QG13] Jing Qin and Weihong Guo. "An efficient compressive sensing MR image reconstruction scheme." In *Biomedical Imaging (ISBI), 2013 IEEE 10th International Symposium on*, pp. 306–309. IEEE, 2013.

[QWL16] Jing Qin, Tianyu Wu, Ying Li, Wotao Yin, Stanley Osher, and Wentai Liu. "Accelerated High-Resolution EEG Source Imaging." *CAM Report 16-75*, 2016.

[QYW14] Jing Qin, Xiyu Yi, Shimon Weiss, and Stanley Osher. "Shearlet-TGV Based Fluorescence Microscopy Image Deconvolution." *CAM Report 14-32*, 2014.

[RDD12] Philippe Rigoard, Alexandre Delmotte, Samuel D'Houtaud, Lorraine Misbert, Bakari Diallo, Aline Roy-Moreau, Sylvain Durand, Solène Royoux, Jean-Philippe Giot, and Benoit Bataille. "Back pain: a real target for spinal cord stimulation?" *Neurosurgery*, **70**(3):574–585, 2012.

[RFH09] Ceon Ramon, Walter J Freeman, Mark Holmes, A Ishimaru, Jens Haueisen, Paul H Schimpf, and Elham Rezvanian. "Similarities between simulated spatial spectra of scalp EEG, MEG and structural MRI." *Brain topography*, **22**(3):191–196, 2009.

[RFR14] Giulio Ruffini, Michael D Fox, Oscar Ripolles, Pedro Cavaleiro Miranda, and Alvaro Pascual-Leone. "Optimization of multifocal transcranial current stimulation for weighted cortical pattern targeting from realistic modeling of electric fields." *Neuroimage*, **89**:216–225, 2014.

[RHZ13] Zemin Ren, Chuanjiang He, and Qifeng Zhang. "Fractional order total variation regularization for image super-resolution." *Signal Processing*, **93**(9):2408–2421, 2013.

[RJI11] Shriram Raghunathan, Arjun Jaitli, and Pedro P Irazoqui. "Multistage seizure detection techniques optimized for low-power hardware platforms." *Epilepsy & Behavior*, **22**:S61–S68, 2011.

[RSV16] JC Reyes, C-B Schönlieb, and T Valkonen. "Bilevel Parameter Learning for Higher-Order Total Variation Regularisation Models." *Journal of Mathematical Imaging and Vision*, pp. 1–25, 2016.

[Sar87] J. Sarvas. "Basic mathematical and electromagnetic concepts of the biomagnetic inverse problem." *Phys. Med. Biol.*, **32**:11–22, 1987.

[SDO14] Samuel S Shin, C Edward Dixon, David O Okonkwo, and R Mark Richardson. "Neurostimulation for traumatic brain injury: A review." *Journal of neurosurgery*, **121**(5):1219–1231, 2014.

[SGA78] RD Sidman, V Giambalvo, T Allison, and P Bergey. "A method for localization of sources of human cerebral potentials evoked by sensory stimuli." *Sensory Processes*, **2**(2):116, 1978.

[SHI09] Tomiki Sumiyoshi, Yuko Higuchi, Toru Itoh, Mie Matsui, Hirofumi Arai, Michio Suzuki, Masayoshi Kurachi, Chika Sumiyoshi, and Yasuhiro Kawasaki. "Effect of perospirone on P300 electrophysiological activity and social cognition in schizophrenia: a three-dimensional analysis with sloreta." *Psychiatry Research: Neuroimaging*, **172**(3):180–183, 2009.

[SLW16] Abbas Sohrabpour, Yunfeng Lu, Gregory Worrell, and Bin He. "Imaging brain source extent from EEG/MEG by means of an iteratively reweighted edge sparsity minimization (IRES) strategy." *NeuroImage*, **142**:27–42, 2016.

[SN11] Charlotte J Stagg and Michael A Nitsche. "Physiological basis of transcranial direct current stimulation." *The Neuroscientist*, **17**(1):37–53, 2011.

[SSS08] Ariane Schad, Kaspar Schindler, Björn Schelter, Thomas Maiwald, Armin Brandt, Jens Timmer, and Andreas Schulze-Bonhage. "Application of a multivariate seizure detection and prediction method to non-invasive and intracranial long-term EEG recordings." *Clinical neurophysiology*, **119**(1):197–211, 2008.

[Sub07] Abdulhamit Subasi. "EEG signal classification using wavelet feature extraction and a mixture of expert model." *Expert Systems with Applications*, **32**(4):1084–1093, 2007.

[SV86] Michael Scherg and Detlev Von Cramon. "Evoked dipole source potentials of the human auditory cortex." *Electroencephalography and Clinical Neurophysiology/Evoked Potentials Section*, **65**(5):344–360, 1986.

[SVS12] Rosalind J Sadleir, Tracy D Vannorsdall, David J Schretlen, and Barry Gordon. "Target Optimization in Transcranial Direct Current Stimulation." *Frontiers in Psychiatry*, **3**, 2012.

[TA97] Pham Dinh Tao and Le Thi Hoai An. "Convex analysis approach to DC programming: Theory, algorithms and applications." *Acta Mathematica Vietnamica*, **22**(1):289–355, 1997.

[TKE10] Adriano BL Tort, Robert Komorowski, Howard Eichenbaum, and Nancy Kopell. "Measuring phase-amplitude coupling between neuronal oscillations of different frequencies." *Journal of neurophysiology*, **104**(2):1195–1210, 2010.

[TKM09] Adriano BL Tort, Robert W Komorowski, Joseph R Manns, Nancy J Kopell, and Howard Eichenbaum. "Theta–gamma coupling increases during the learning of item–context associations." *Proceedings of the National Academy of Sciences*, **106**(49):20942–20947, 2009.

[TKT08] Adriano BL Tort, Mark A Kramer, Catherine Thorn, Daniel J Gibson, Yasuo Kubota, Ann M Graybiel, and Nancy J Kopell. "Dynamic cross-frequency couplings of local field potential oscillations in rat striatum and hippocampus during performance of a T-maze task." *Proceedings of the National Academy of Sciences*, **105**(51):20517–20522, 2008.

[Tuc93] Don M Tucker. "Spatial sampling of head electrical fields: the geodesic sensor net." *Electroencephalography and clinical neurophysiology*, **87**(3):154–163, 1993.

[UHS98] Kimmo Uutela, Matti Hamalainen, and Riitta Salmelin. "Global optimization in the localization of neuromagnetic sources." *IEEE Transactions on Biomedical Engineering*, **45**(6):716–723, 1998.

[UHS99] Kimmo Uutela, M Hämäläinen, and Erkki Somersalo. "Visualization of magnetoencephalographic data using minimum current estimates." *NeuroImage*, **10**(2):173–180, 1999.

[VMS08] Mayrim Vega-Hernández, Eduardo Martínez-Montes, José M Sánchez-Bornot, Agustín Lage-Castellanos, and Pedro A Valdés-Sosa. "Penalized least squares methods for solving the EEG inverse problem." *Statistica Sinica*, **18**(4):1535–1551, 2008.

[WCC06] Brian R Webster, Pablo A Celnik, and Leonardo G Cohen. "Noninvasive brain stimulation in stroke rehabilitation." *NeuroRx*, **3**(4):474–481, 2006.

[YEX14] Penghang Yin, Ernie Esser, and Jack Xin. "Ratio and difference of L1 and L2 norms and sparse representation with coherent dictionaries." *Commun. Inform. Systems*, **14**:87–109, 2014.

[YLH15] P. Yin, Y. Lou, Q. He, and J. Xin. "Minimization of L1-L2 for Compressed Sensing." *SIAM J. of Sci. Computing*, **37**(1):A536–A563, 2015.

[ZGB05] Yiheng Zhang, Alireza Ghodrati, and Dana H Brooks. "An analytical comparison of three spatio-temporal regularization methods for dynamic linear inverse problems in a common statistical framework." *Inverse Problems*, **21**(1):357, 2005.

[ZLH16] Hanyue Zhou, Ying Li, Yue-Loong Hsin, and Wentai Liu. "Phase-amplitude coupling analysis for seizure evolvement using Hilbert Huang Transform." In *Engineering in Medicine and Biology Society (EMBC), 2016 IEEE 38th Annual International Conference of the*, pp. 1022–1025. IEEE, 2016.

[ZZD14] Min Zhu, Wenbo Zhang, Deanna L Dickens, and Lei Ding. "Reconstructing spatially extended brain sources via enforcing multiple transform sparseness." *Neuroimage*, **86**:280–293, 2014.